1-9-2020

Stellar Nucleosynthesis: Direct Measurement of the Neutron-Capture Cross Sections of Stable Germanium Isotopes and Design of a Next Generation Ion Trap for the Study of Beta-Delayed Neutron Emission

Alexander Laminack
Louisiana State University and Agricultural and Mechanical College

STELLAR NUCLEOSYNTHESIS: DIRECT MEASUREMENT OF THE NEUTRON-CAPTURE CROSS SECTIONS OF STABLE GERMANIUM ISOTOPES AND DESIGN OF A NEXT GENERATION ION TRAP FOR THE STUDY OF β-DELAYED NEUTRON EMISSION

A Dissertation

Submitted to the Graduate Faculty of the
Louisiana State University and
Agricultural and Mechanical College
in partial fulfillment of the
requirements for the degree of
Doctor of Philosophy

in

The Department of Physics and Astronomy

by
Alexander Laminack
B. S., The Unviersity of Alabama, 2015
May 2020

To my wife and son: Kristy Allen Alexander Laminack and Daniel Allen Laminack.
Also to my mother and father: Kelley Gene Laminack Jr. and Connie Elizabeth Harkey Laminack.

Acknowledgments

First I would like to acknowledge my advisers Dr. Jeffrey Blackmon and Dr. Scott Marley. Their constant mentorship was essential to my progress in my graduate studies. Dr. Marley introduced me to nuclear physics experiments using ion traps. Dr. Blackmon mentored me through data analysis methods and provided me with ample opportunities to perform and contribute to nuclear physics experiments. Also thanks to the funders of my research at the U.S. Department of Energy Office of Science, Office of Nuclear Physics under Award DE-FG02-96ER40978 and under Contract Number DE-AC02-06CH11357. Additionally I would like to thank the tight-knit group of graduate students in the LSU nuclear physics group. Help was always given in abundance when needed.

I would like to extend a special thanks to the DANCE group at LANL as well. Dr. John Ullmann was a great help to me in performing experiments at LANSCE using DANCE, Dr. Chris Prokop offered guidance with data analysis, and Dr. Aaron Couture provided assistance with both. This work benefited from the use of the LANSCE accelerator facility at Los Alamos National Laboratory. A.C. and J.L.U. were supported under the auspices of the US Department of Energy by Los Alamos National Security, LLC, under Contract No. DE-AC52-06NA25396. Additionally I would like to thank Stanislav Valenta of Charles University in Prague. Standa was instrumental in providing the input for the DICEBOX simulations for my neutron capture experiment. A special thanks to Steve Elliott with the MAJORANA Project for providing the MAJORANA sample and to John Greene of Argonne National Laboratory for pressed-powder sample preparation.

Finally I would like to thank Dr. Nick Scielzo and the ion trapping group studying β-delayed neutron emission at LLNL and ANL. Nick's instruction was pivotal in developing my understanding of Geant4 and SIMION as well as using these tools to accurately simulate systems used in nuclear physics experiments.

Contents

Abstract

Knowledge of stellar nuclear reaction rates is critical to understanding the cosmic origins of the abundances of elements. In order to determine these reaction rates, accurate measurements of nuclear cross sections are needed. This thesis presents the results of an experiment to directly measure the neutron capture cross sections of ^{70}Ge, ^{72}Ge, ^{74}Ge, and ^{76}Ge. These measurements were performed at the Los Alamos Neutron Science CEnter (LANSCE) using the Detector for Advanced Neutron Capture Experiments (DANCE). This is the first direct measurement for many of these isotopes across the neutron energy spectrum of 10 eV to 1 MeV using the neutron time-of-flight method. Maxwellian-Averaged Cross Sections (MACS) were calculated from these measurements at the astrophysically relevant temperatures in order to determine the stellar nuclear reaction rates. The results of this experiment are neutron capture cross sections and MACS for ^{70,72,74,76}Ge with uncertainties on the order of 5%. A comparison of these values to the current evaluated cross sections in two databases is also presented.

In addition to the experimental component of my thesis, a series of simulations were performed in the pursuit of designing a next-generation ion trap named the BEtA-Recoil trap (BEARtrap). BEARtrap was designed for β-delayed neutron emission studies. It is a linear Paul trap surrounded by an array of MCP detectors and plastic scintillator detectors. β-delayed neutron emission affects the abundance curves for heavy elements created in the r-process, comprises a major component of nuclear reactor neutron fluxes, and has national security applications. BEARtrap allows for a novel technique to simultaneously measure the β-delayed neutron emission branching ratios and emitted neutron energy spectra by means of β-recoil ion coincident detection.

Chapter 1. Background and Motivation

1.1. Introduction

One of the great questions of physics is the origin of elements. Fusion provided the answer to this question for light elements but was shown not to be responsible for the creation of the heavier elements (A>56). These heavier elements are synthesized primarily by two distinct neutron-capture processes. One of these processes occurs in asymptotic giant branch stars and heavy main sequence stars. This is the slow neutron-capture process. Measuring the neutron-capture cross sections for the isotopes present in these environments is essential to understanding the origin of heavy elements. The first half of this thesis will detail an experiment to measure the cross sections of a few such isotopes, namely the stable isotopes of germanium. The other neutron-capture process is characterized by rapid neutron capture and occurs in neutron star mergers and potentially other sites. The isotopes produced in these events are very neutron rich and thus unstable. In order to understand the stable isotopes that are ultimately produced by these neutron star mergers, it is critical to understand the decay properties of the unstable isotopes that decay back to stability. The second half of this thesis will outline the design and simulation of a next-generation ion trap used to study the decay of neutron-rich nuclei.

This thesis is composed of 8 chapters. Chapter 1 explores the astrophysics background behind the synthesis of intermediate mass elements and the motivation for the germanium cross section measurements. Details of the experiments themselves including setup, detectors, calibrations, and samples are presented in Chapter 2. Chapter 3 outlines the data analysis process for these experiments in great detail. This chapter will focus on the analysis for ^{74}Ge as an example, although the process is similar for all isotopes. Chapter 4 shows the results of the ^{74}Ge cross section measurement as well as a comparison to previously accepted data where available. The results for the remaining germanium isotopes are presented in Chapter 5. In Chapter 6 the discussion moves on from neutron capture to the physics of

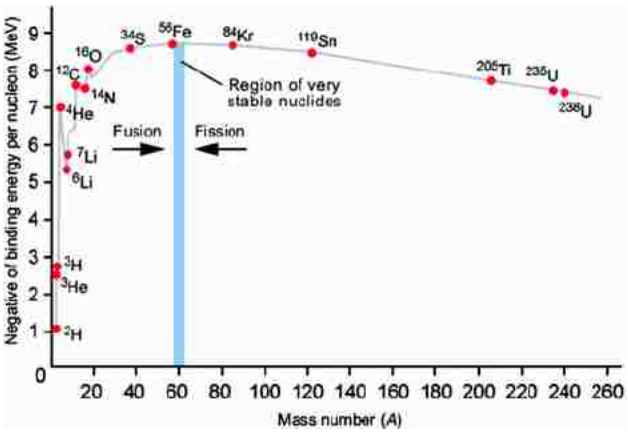

Figure 1.1. Binding energies per nucleon for the elements[2]

β-delayed neutron emission. This chapter includes the background and motivation for studying β-delayed neutron emission as well as a discussion of ion traps and their role in studying radioactive decay. Chapter 7 details the simulation and design of a next-generation ion trap dedicated to the study of β-delayed neutron emission. Finally, a closing chapter is dedicated to summarizing the results of the neutron capture experiment and the progress on designing and commissioning the next generation ion trap.

1.2. Synthesis of Elements Heavier Than Iron

Nuclear fusion reactions occurring in the cores of stars produce the light elements we observe. The framework for these processes was outlined by Fred Hoyle[1]. As long as the binding energy per nucleon of the fusion product is higher than that of the reactants, energy is released by the fusion reaction as the star continues to burn. Figure 1.1 is a plot of binding energies per nucleon for the stable elements. Stellar fusion processes can only synthesize elements up to around the peak of this curve which is at ^{56}Fe.

The question arises, how are the elements heavier than iron synthesized? A famous paper called the B^{2}FH paper (named after its authors Burbidge, Burbidge, Fowler, and Hoyle) was published in 1957 that detailed the processes by which elements heavier than iron are synthesized. They concluded that neutron-capture processes could synthesize heavy elements in stars[3]. Neutron capture is preferred over charged-particle capture because the neutron

does not have to overcome the Coulomb barrier, which increases with proton number and makes charged-particle capture highly unlikely at stellar temperatures. At closed neutron shells, the neutron-capture cross section becomes very small compared to the cross section between closed shells. Therefore, if heavy elements are created by a sequence of neutron captures, peaks would appear in the isotopic abundance curves corresponding to these closed neutron shells. While the expected peaks are present in the observed isotopic abundance curve, the presence of a double-peaked structure (shown in Figure 1.2) implies that there must be two distinct capture processes occurring. These processes are differentiated by the timescale over which they occur. The slow neutron-capture process, or s process, occurs on or very near the valley of stability. As a result, the s-process peaks in isotopic abundance occur at the closed neutron shells as expected. On the other hand, the r process is characterized by rapid sequential captures of neutrons. This process occurs in neutron star mergers and maybe in other scenarios such as core-collapse supernovae. The rapid capture of neutrons produces isotopes that are very neutron rich and these isotopes accumulate in higher numbers around closed neutron shells as mentioned before. When they decay back to stability, the result is a shifting downward in proton number of the peak relative to the closed shell abundances produced by the s process. These two processes explain the presence of a double peaked structure in the observed atomic abundance curve.

Studying s-process nuclei is inherently easier than their r-process counterparts since the s process occurs along stability. This means that targets can be made out of s-process isotopes and their cross sections can be measured directly. With precisely measured neutron capture cross sections of s-process nuclei, we can determine stellar reaction rates and produce reliable predictions for s-process abundances. Certain stable isotopes are shielded from the r process by other stable isotopes and are thus produced only by the s process. Figure 1.3 shows a diagram of the s and r processes on a subset of the chart of nuclides. Here you can see portion of the chart of nuclides showing graphically how s-only isotopes arise. These s-only isotopes present important constraints to nucleosynthesis models. Aside from studying the s

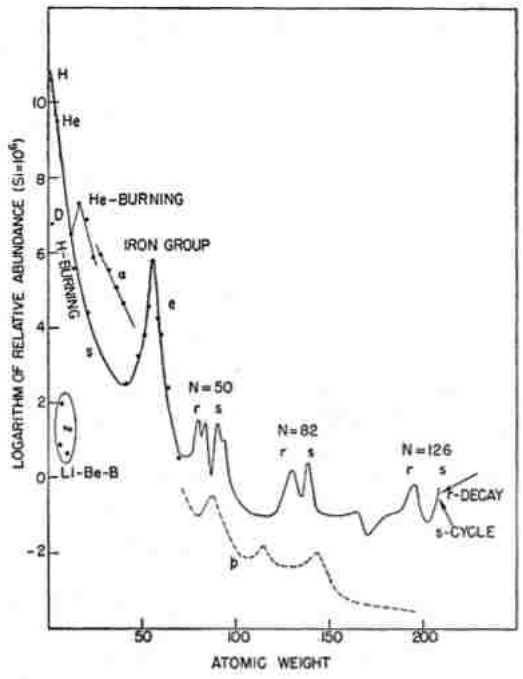

Figure 1.2. Observed atomic abundances. Note the double peaked structure for elements heavier than iron[3]. This suggests two distinct processes for synthesizing elements.

process itself, this also allows us to infer the structure of the r process. By subtracting off a reliable s-process abundance pattern from the observed solar system isotopic abundances, we obtain the expected r-process abundance curve. This abundance pattern will inform future efforts to study the r process as facilities gain access to the neutron rich r-process isotopes.

When B^2FH explained Solar System abundances, they attempted to model the s process using what is now known as the classical s-process model. This simple model begins with ^{56}Fe nuclei being irradiated by a neutron source and assumes that temperature and neutron density are constant. By using observed s-only abundances, Clayton *et al.* showed that a single irradiation of an iron seed is insufficient[5]. This problem was remedied by Seeger *et al.* when they showed an exponential distribution of neutron exposures can accurately produce the s-only isotope abundances[6]. The neutron density as a function of the time-integrated neutron flux is then given by Equation 1.1

$$\rho(\tau) = \frac{G \cdot N_{56}^{\odot}}{\tau_0} exp(-\tau/\tau_0) \tag{1.1}$$

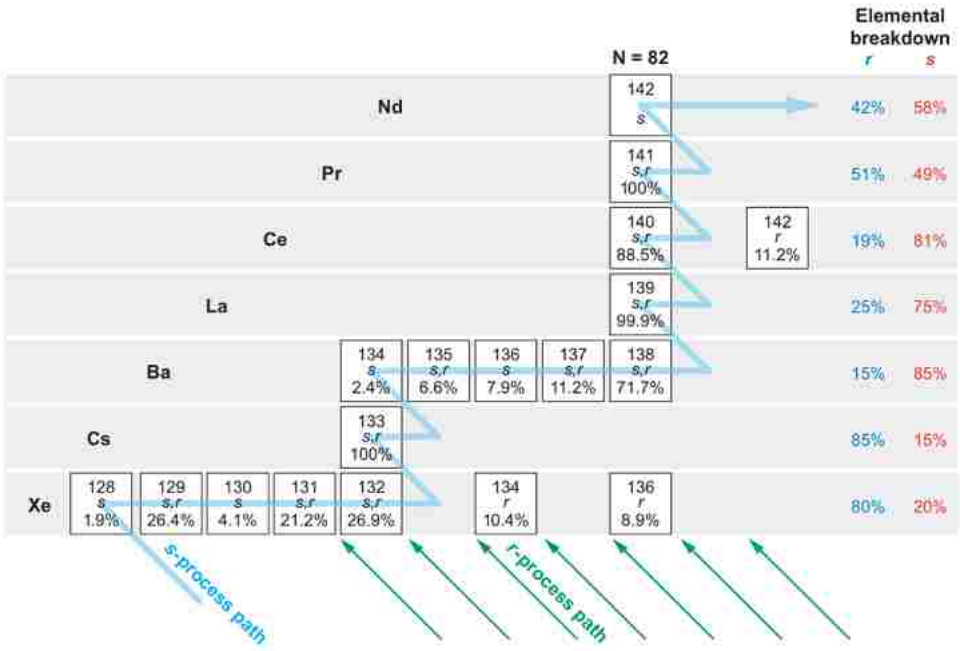

Figure 1.3. A subsection of the chart of nuclides showing the reason for s-only isotopes. Each nuclide has an s, r, or both depending on which process produces it. Note how stable isotopes like ^{134}Xe shield ^{134}Ba from decaying r-process isotopes [4].

An analytical solution arises for calculating s-process abundances. Reaction flow, which is characterized by multiplying the Maxwellian-Averaged Cross Section (MACS) with the s-process abundances, is given by Equation 1.2.

$$\langle\sigma\rangle_{(A)} N_{s(A)} = \frac{G \cdot N_{56}^{\odot}}{\tau_0} \prod_{i=56}^{A} (1 + \frac{1}{\tau_0 \langle\sigma\rangle_i})^{-1} \tag{1.2}$$

Here $\langle\sigma\rangle_{(A)}$ is the MACS of isotope of mass number A, $N_{s(A)}$ is the observed abundance, G is the fraction of the observed ^{56}Fe abundance irradiated, τ_0 is a constant associated with the time-integrated neutron flux, and $N_{56}^{\odot}$ is the observed abundance of ^{56}Fe. G and τ_0 are determined by fitting to observed abundances of s-process only elements. A plot of this product is show in Figure 1.4.

The results of this study implied that there must be multiple components of the s process. The abundance curve can only be explained by two radically different exponential neutron exposures using the classical model. These two components are now known as the main and

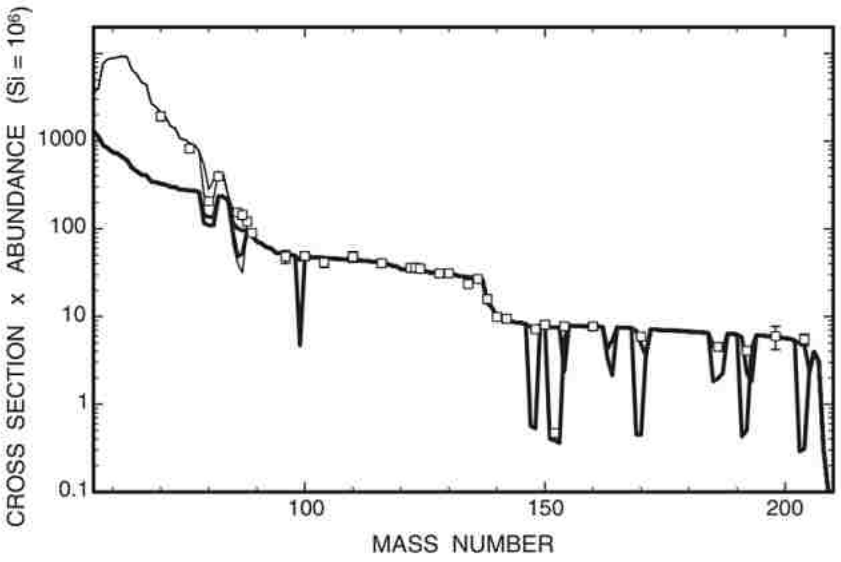

Figure 1.4. The product of neutron-capture cross section and observed abundance as a function of mass number[7]. The open squares are known s-process only isotopes. The dark line represents only the main s process. The light line represents the abundance curve generated by a weak and main s process combined.

weak components of the s process. The natural next step was to investigate potential sites for these two processes. Käppeler, Beer, and Wisshak review the discovery of astrophysical sites suitable to the main and weak components of the s process[8]. It was discovered that low mass $(1.5-3M_{\odot})$ Asymptotic Giant Branch (AGB) stars produced a suitable environment for the main s process while high mass main sequence stars $(8-25M_{\odot})$ host the weak component. A combination of precisely measured neutron capture cross sections[9] and well known isotopic abundances of s-process only isotopes[10] has resulted in a good understanding of the main s process. On the other hand, the weak s process is more poorly understood for a few reasons. A significant cause is the uncertainty in reaction rates surrounding the $^{22}Ne(\alpha, n)$ reaction, which is the neutron source for the weak s process. Additionally, there are relatively few s-only isotopes in the relevant mass region $(60 \leq A \leq 90)$, which are used as calculation restraints. Finally, and most importantly for this work, many neutron-capture cross sections for weak s-process isotopes are either imprecisely measured or not directly measured at all[9].

1.3. Germanium Cross Section Motivation

The less well understood component of the s-process is the weak s process and it occurs in high mass main sequence stars ($8-25M_{\odot}$). The s process produces roughly half of the elements heavier than iron and the weak component is responsible for synthesizing the elements in the mass range from iron to strontium ($60 \leq A \leq 90$). Since the primary neutron source for the weak s process is the $^{22}Ne(\alpha, n)$ reaction, it is important to understand the synthesis of ^{22}Ne. Peters outlines a series of stellar reactions that synthesize ^{22}Ne from a ^{14}N seed which is produced in the CNO cycle[11]. These reactions are $^{14}N(\alpha, \gamma)^{18}F(\beta^{+})^{18}O(\alpha, \gamma)^{22}Ne$. Core helium burning provides the thermal energy needed to allow these reactions to proceed peaking at approximately 2.5×10^{8} K. Once helium core burning ceases, the leftover helium is used as the α source for the all important $^{22}Ne(\alpha, n)$ reaction. The temperature during this phase is 3×10^{8} K which means that the neutrons produced have energies distributed in a Maxwellian distribution with thermal energy $kT = 30$ keV. Once the leftover helium is consumed, there is ^{22}Ne remaining, which will reignite during carbon burning due to the α particles produced by the $^{12}C(^{12}C, \alpha)$ reaction[12]. This takes place at a temperature corresponding to $kT = 90$ keV. It might seem as though this would generate a source of abundant neutrons for capture in the s process since a lot of ^{14}N is produced by the CNO cycle, however, the $^{22}Ne(\alpha, n)^{25}Mg$ reaction is self-poisoning. Most of the neutrons produced by this reaction are indeed captured by the resulting ^{25}Mg leading to the limited mass range reached by the weak s-process ($60 \leq A \leq 90$)[13].

Studies have been carried out to investigate how sensitive the relative s-process isotopic abundances are to changes in reaction rates of other isotopes in the s-process path. The results show that changes in the reaction rates of lighter weak s-process nuclei propagate up the chain of heavier weak s-process isotopes and cause significant changes in isotopic abundances[12]. This is because the neutron flux present in the weak s process is too low to achieve reaction flow equilibrium[12]. Therefore, an accurate measure of the neutron capture cross sections of s-process elements is critical in order to predict isotopic abundances. An

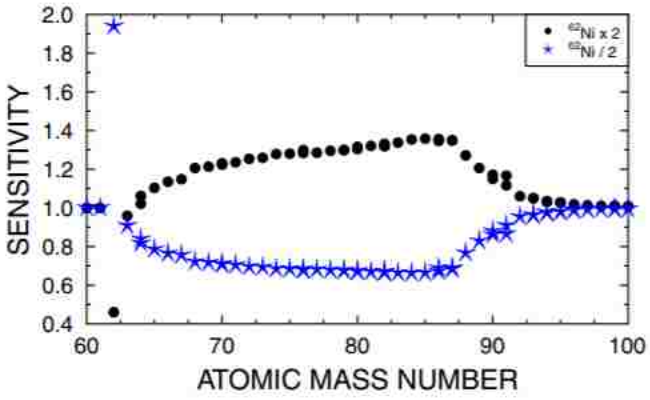

Figure 1.5. The effects of an arbitrary factor of two change in the $^{62}Ni(n,\gamma)$ cross section propagating down the line to the abundances of heavier elements[14]. A similar effect is found for all weak s-process isotopes, including germanium.

example of the fractional change in isotopic abundance to a factor 2 change in cross section as a function of mass number is shown in Figure 1.5.

Since every isotope along the weak s-process path affects the abundance of isotopes produced downstream, the capture cross sections for all isotopes on the path are of interest. Figure 1.6 shows this sensitivity[12]. This figure shows the fractional change in abundances produced by nucleosynthesis calculations performed only 9 years apart with updated data. The first thing to note is that the abundances change greatly with only a few years of updated data. Second to note is the uncertainty of the abundances of many of these isotopes. All stable germanium isotopes ($^{70,72,73,74,76}Ge$) participate in the weak s process but ^{72}Ge and ^{73}Ge were identified by Pignatari *et al.* as being of particular importance for new measurements since only theoretical cross sections exist for these two isotopes. Although measured cross sections exist for the other isotopes, making measurements with a consistent and more modern setup allows us to improve systematic uncertainties. We also need samples of each isotope for background subtraction purposes so we have measured the cross sections for all the even stable germanium isotopes.

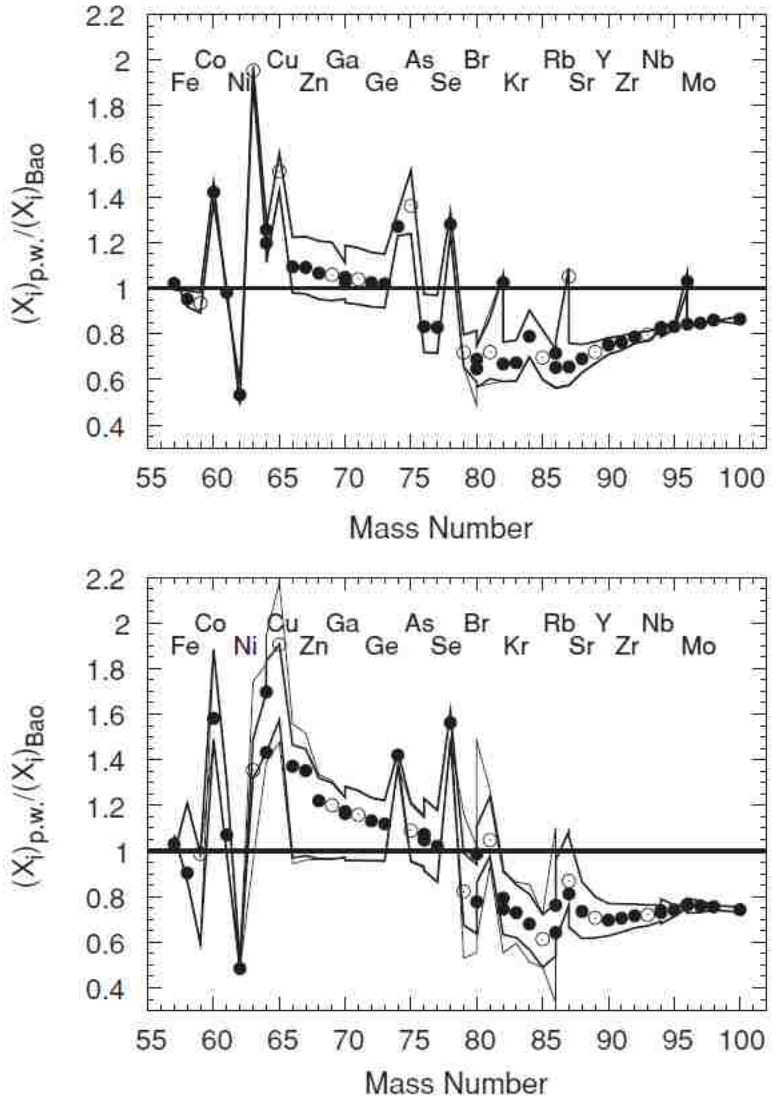

Figure 1.6. Top: isotopic abundances after He core burning calculated by Pignatari *et al.* (2010)[12] relative to that obtained using the Maxwellian averaged cross-sections (MACS) for isotopes heavier than iron by Bao *et al.* (2000)[9]. Dark lines indicate maximum and minimum yields from the rates used by Pignatari et al. The light lines indicate maximum and minimum yields when a factor of 2 uncertainty for the MACS of the unstable isotopes ^{63}Ni, ^{79}Se, and ^{85}Kr is included. Even and odd Z elements are distinguished by filled and empty circles, respectively. Bottom: the same comparison but for just after C shell burning. Figure from Bao *et al.* [9].

1.4. High Energy Physics

Aside from the primary motivator (the astrophysical impact), there is another useful application for these neutron-capture cross section measurements. There are currently experiments being carried out to search for neutrinoless double β-decay ($0\nu\beta\beta$) of ^{76}Ge. ^{76}Ge is a convenient isotope for this experiment because the sample material is also the detector. The demonstrator experiment for this project is known as MAJORANA[15] and the final iteration will be an international collaboration called LEGEND. This ambitious project is an effort with a great deal of funding due to its scientific significance. $0\nu\beta\beta$ is a process wherein a nucleus undergoes two simultaneous β-decays without emitting a neutrino. This process is allowed only if the neutrino is a so-called Majorana particle, meaning that the neutrino is its own antiparticle. Observation of this process would be vastly significant since it would violate lepton number, a fundamental symmetry of the Standard Model.

The half-life of $0\nu\beta\beta$ in ^{76}Ge is at least 10^{25} years. This corresponds to about 1 expected count per year for their 1 ton sample[15]. Backgrounds are required to be extremely limited and well understood so the experiment will take place deep underground. While the underground environment heavily suppresses background from cosmic rays, there is a steady background of muon-induced cosmogenic neutrons[16]. A major source of background for LEGEND will come from these neutron capturing on ^{76}Ge and a minor impurity of ^{74}Ge. A simulation of the cosmogenic neutron background expected in the LEGEND experimental site is shown in Figure 1.7. A prominent feature is displayed near the region of interest near 2023 keV corresponding to neutron capture on ^{76}Ge. A precise measurement of the ^{74}Ge(n,γ) and ^{76}Ge(n,γ) cross sections are required in order to properly characterize this background. As part of a collaboration, physicists working on LEGEND have supplied us with a fragment from their detector crystal. This fragment, prepared as a sample for our neutron capture measurement, is shown in Figure 1.8. A comparison of evaluated cross sections to our measurements is presented later in this thesis to examine the impact of our measurement on their background characterization.

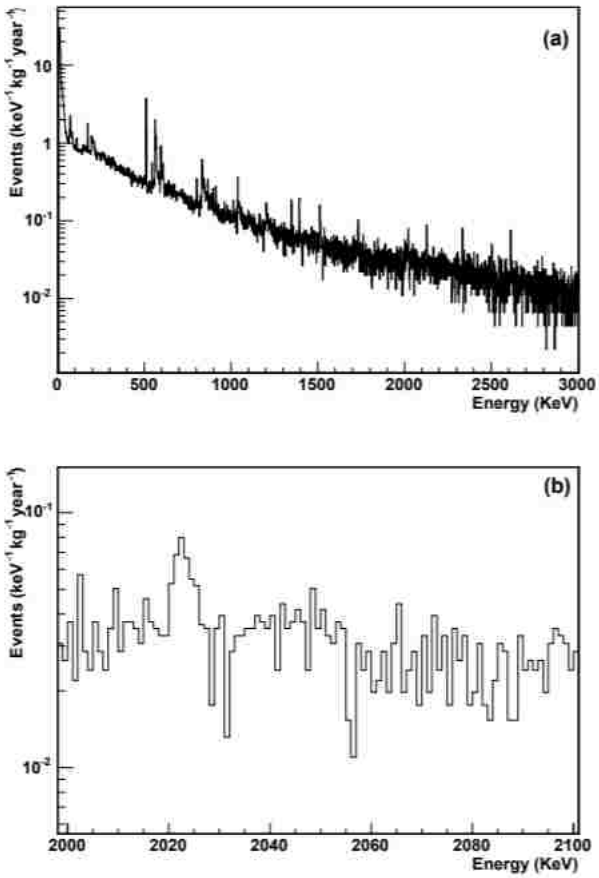

Figure 1.7. Simulated cosmogenic background at the deep underground lab site for the LEGEND project. Top: total spectrum of the background. Bottom: background zoomed in on the region of interest for LEGEND. The peak around 2023 keV is produced by neutron capture on ^{76}Ge, which comprises the MAJORANA detector and sample.

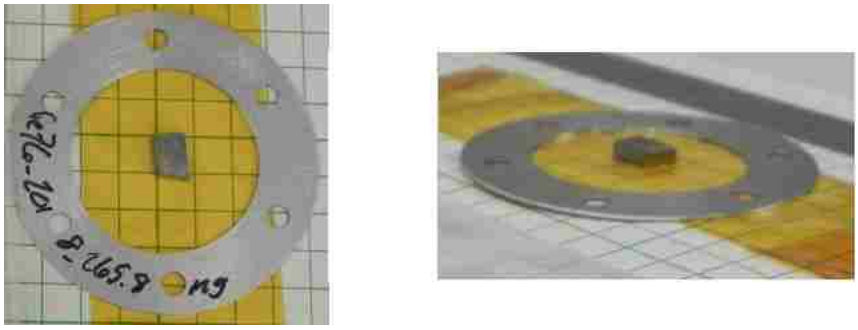

Figure 1.8. Chip off of the MAJORANA detector crystal prepared as a sample for our neutron capture experiment.

Chapter 2. Neutron Capture Experiments

2.1. Overview

These experiments were conducted at the Los Alamos Neutron Science CEnter (LANSCE) at Los Alamos National Laboratory (LANL). At LANSCE, an 800 MeV proton beam is produced using a linear accelerator. This beam is bunched into pulses using a proton storage ring before being delivered to a tungsten target where neutrons are produced by high energy spallation reactions. These neutrons are moderated by water moderators before being delivered down various flight paths, one of which contains the equipment used for this experiment[17]. A diagram is shown in Figure 2.1 of flight path 14 that was used for this experiment.

At LANSCE, the neutron energy is determined via the time-of-flight method. The flight path length and the neutron time of flight are needed to calculate this energy. The length of the flight path is defined as the distance from the water moderator viewed by flight path 14 to the center of the Detector for Advanced Neutron Capture Experiments (DANCE) array where the samples are placed. Details about DANCE and its operation are offered in the next section. This distance is used to calculate the incident neutron energy. For a time-of-flight method of determining neutron energy, the only remaining variable needed is the actual time it takes to get to the sample. This is provided by two pieces of data: 1) a T_0 timing signal provided by the beam operators for when the proton beam pulse contacts the spallation target and 2) the time stamp recorded when either a detection occurs in DANCE or in the downstream beam monitors. Since the neutron mass, distance traveled, and the time-of-flight are determined, the incident neutron energies (which are less than 1 MeV) can be calculated using the non-relativistic kinetic energy equation given in Equation 2.1.

$$E_n = \frac{1}{2} m_n \frac{l_{FP}^2}{t_{TOF}^2} \tag{2.1}$$

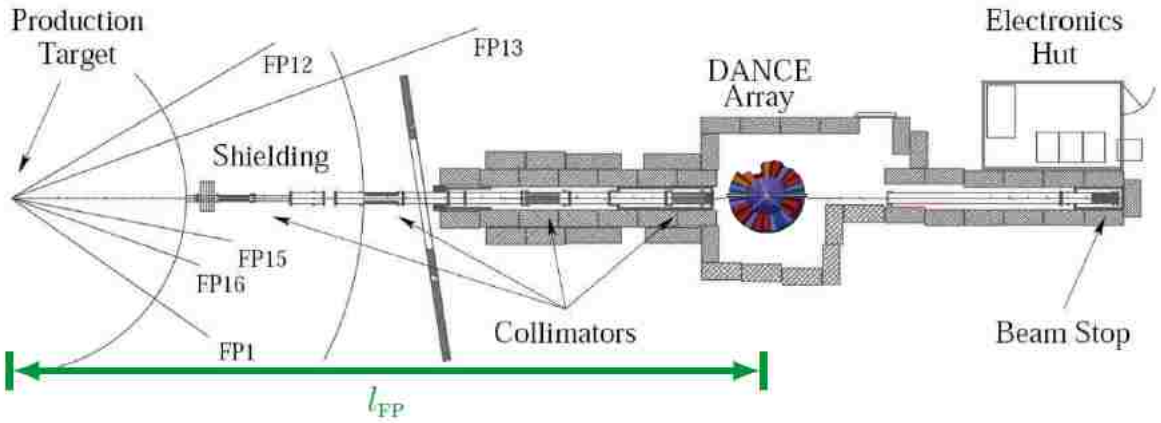

Figure 2.1. A diagram depicting flight path 14. Here, l_{FP} is the distance from the neutron source to the DANCE array[18].

Here E_n represents the neutron energy, m_n is the neutron mass, l_{FP} is the flight path length, and t_{TOF} is the neutron time of flight. The uncertainty in this energy is dominated by the initial width of the proton pulse (250 ns) as well as broadening effects of the moderator. Two independent uncertainties in the time of flight and the flight-path length can be propagated to acquire the uncertainty in the neutron energy using Equation 2.2.

$$\Delta E_n = 2E_n\sqrt{\left(\frac{\Delta l_{FP}}{l_{FP}}\right)^2 + \left(\frac{\Delta t_{TOF}}{t_{TOF}}\right)^2} \tag{2.2}$$

A timing signal is generated to signify that a pulse of protons has impinged on the spallation target. A window is generated during which data will be collected from DANCE. The length of the window will determine the neutron energy range examined. For this experiment, the energy range was chosen to be between 10 eV and 1 MeV.

2.2. Experimental Setup

In flight path 14 at LANSCE sits an array of 160 BaF_2 detectors that form DANCE, a nearly 4π solid angle calorimeter. After a nucleus captures a neutron, it de-excites by emitting a cascade of gamma rays. The principle of calorimetry in the context of this experiment is that the entire gamma cascade is ideally detected. The reason for this is explained in further detail later in the thesis. Each of these gamma detectors views an equal

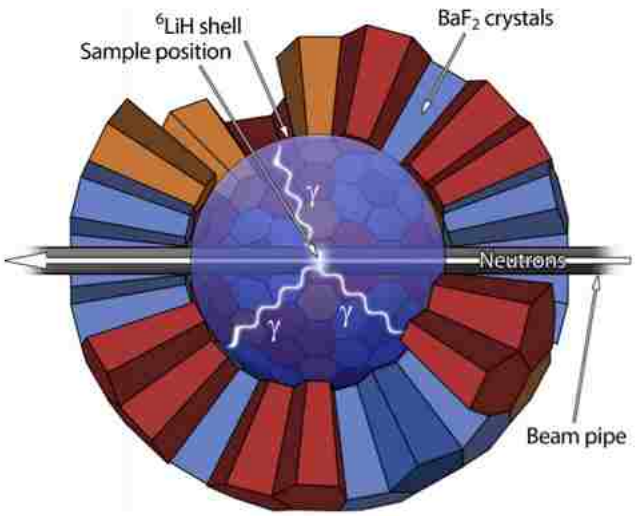

Figure 2.2. A diagram of the 160 elements that form DANCE. The different colors represent the 4 distinct crystal shapes[19].

solid angle from the center of the array. Two holes are left in the array to allow the neutron beam to enter and exit. These 162 slots make up the entire detector array. A diagram can be seen in Figure 2.2.

In order to detect entire gamma cascades, the concept of coincident detections must be established. Two or more gamma detections are said to be coincident if they occur within a range of times set by the experimenter known as a coincidence window. In the case of these experiments, these coincidence windows have to be very tight to reduce dead time between gamma cascades as much as possible and to reduce the uncertainty in neutron energy as much as possible since its computation depends on timing. For this reason, BaF_2 was chosen as the detector material for DANCE due to its superior timing properties compared to other scintillators. Of some interest in these experiments is the multiplicity of gamma rays detected within a coincidence window. This is merely the number of gamma rays detected as a single capture event and it is discussed at length in the analysis section.

Three types of beam monitors are placed downstream from DANCE. They are used to determine the neutron flux seen by the targets. The three detectors are a ^{3}He proportional counter, ^{6}LiF converter foil paired with a silicon detector, and a ^{235}U fission chamber. Each of

these detectors are used to monitor neutrons of different energies: ^{3}He for thermal neutrons, ^{6}LiF for $E_n \leq 3$ keV, and ^{235}U for $E_n \geq 3$ keV. For the purpose of this experiment, the ^{3}He monitor was unused since thermal neutrons were not of interest. The reason for the energy region distinctions is related to the relevant reaction cross sections of the different detectors. The cross section for ^{235}U(n,f) varies greatly with many resonances below 3 keV, whereas the cross section for ^{6}Li(n,α) is smoothly varying with neutron energy. Above 3 keV, however, ^{6}Li has a large, broad resonance but an otherwise small cross section relative to that of ^{235}U(n,f). These beam monitor cross sections as a function of energy are shown in Figure 2.3. The reason why the cross section difference above 3 keV is so significant is shown in Figure 2.4, which shows the relevant reaction cross sections for the two complimentary beam monitors. The count rates at higher neutron energy are already low but this is exacerbated by a few strong neutron capture resonances in various beamline components that further reduce the neutron flux at the target location. In addition to the high-energy resonances, there is another between 200 and 300 eV that would not be discernible if not for the ^{6}Li monitor.

2.3. Detector Calibrations

Timing differences between detectors are the first thing to be calibrated. Gamma rays will often Compton scatter in one crystal and deposit the rest of their energy into another. This fact is exploited to calibrate any timing difference between crystals. The timing calibrations begin at one end of DANCE and are boot-strapped across the entire sphere pair-by-pair until the entire array is calibrated. Because BaF_2 is such a fast detector, coincidence windows can be as narrow as ± 5 ns. An example of the results of this time calibration are shown in Figure 2.5.

Initially, DANCE is energy calibrated using gamma sources placed at the center of the array where samples are placed. The gamma sources allow for a reliable energy calibration using the same type of radiation to be detected in this experiment across a broad range of energies. This calibration is subject change over the course of the experiment as gains shift due to changes in environmental conditions and high voltage bias. Fortunately, the choice of

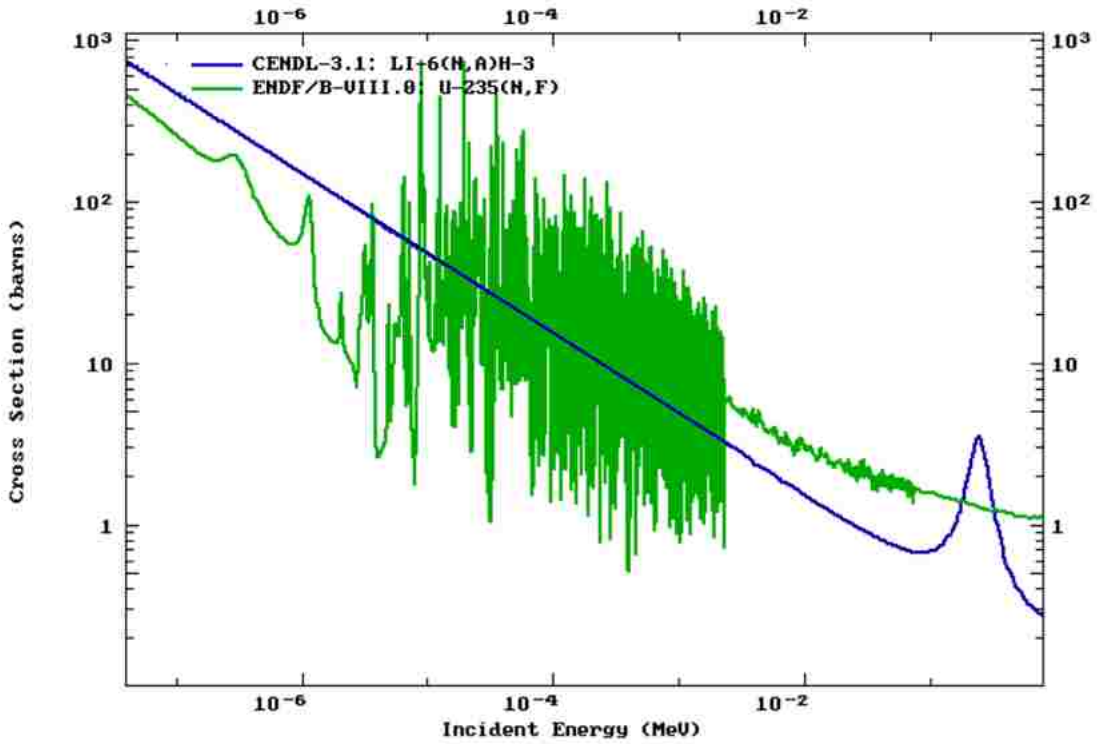

Figure 2.3. CENDL-3.1 ^{6}Li(n,α) cross-section and ENDF/B-VIII.0 ^{235}U(n,f) cross-section. ^{235}U is shown in green and ^{6}Li is shown in blue

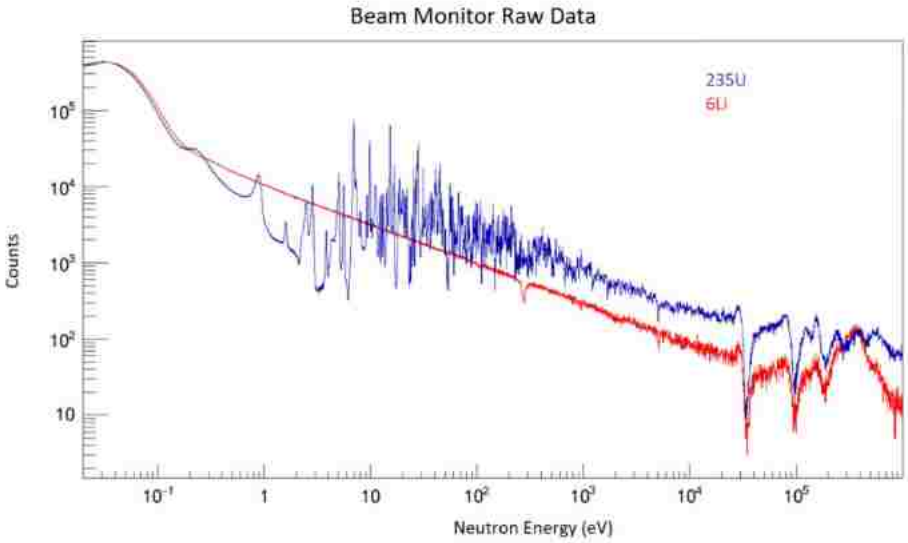

Figure 2.4. Raw beam monitor data from ^{72}Ge runs. Data from the ^{235}U fission chamber is shown in blue and ^{6}LiF foil monitor is shown in red. Note the resonances at high neutron energies that highlight the need for the ^{235}U monitor.

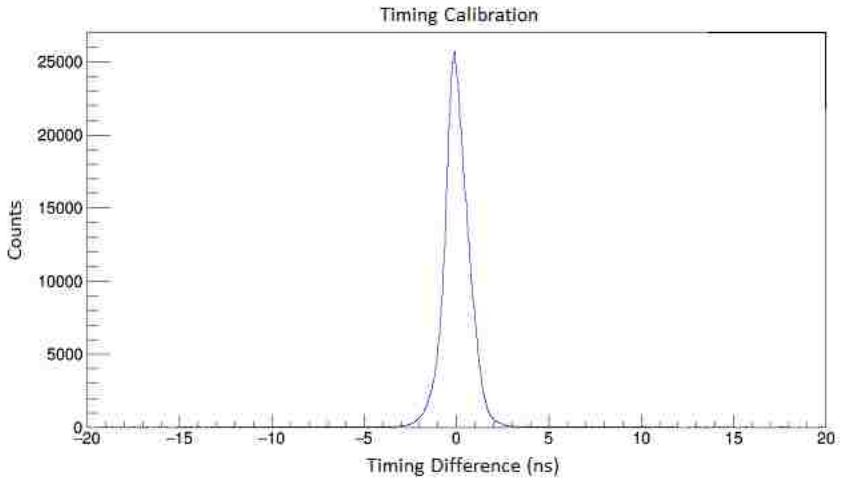

Figure 2.5. Timing difference in ns between the reference crystal (chosen to be crystal 0) and crystal 1. Crystal 1 was chosen arbitrarily as an example but a similar plot exists for each crystal in DANCE.

BaF_2 for the detectors has a secondary benefit for energy calibration. Radium is a chemical analog to barium and as such, there is a small impurity of radium found in each detector of DANCE. Since radium is an alpha emitter, this is a significant source of counts. These counts can be differentiated from gamma detections using pulse-shape discrimination. Pulse-shape discrimination exploits the different characteristic signatures produced by different types of radiation for particle identification. Gammas detected in BaF_2 generate very fast signals whereas alphas generate relatively slowly decaying signals. Examples of signatures produced by gamma rays and alpha particles are shown in Figure 2.6. These two can be differentiated by defining short and long time intervals of the pulse for integration to differentiate these two. As the names imply, the short integral is an integral over the early time portion of the signal ($\sim$100 ns) and the long integral is an integral over the entire decaying signal ($\sim$1000 ns). In a gamma event, these two integrals will return nearly the same value, but in an alpha event the two integrals will return different values. Figure 2.7 shows a two dimensional histogram generated by plotting results of the short integral vs the long integral. If gates are set around the alpha events, these events can be used as a relative energy calibration performed on a run-by-run basis. The peaks in the alpha spectrum are fit and these are used to apply minor

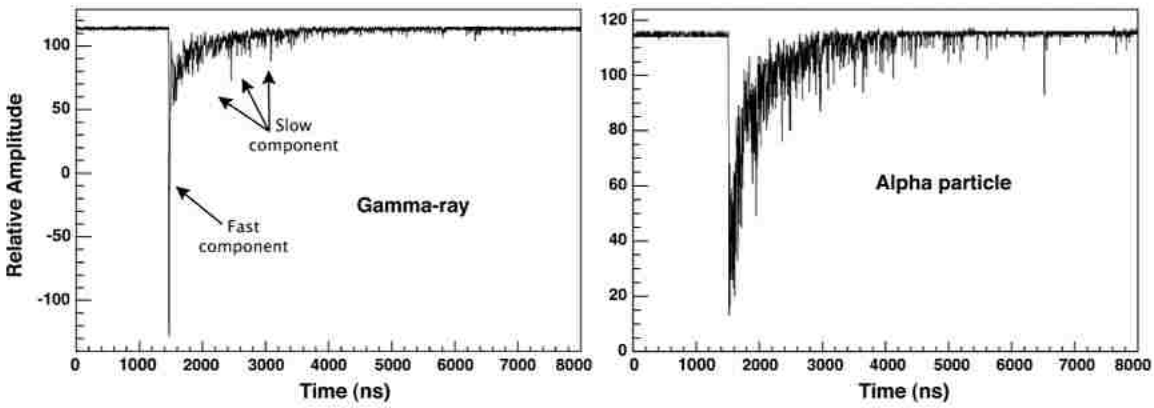

Figure 2.6. Example traces of a gamma ray detection (left) and an alpha particle detection (right) in the detectors of DANCE[20].

Table 2.1. The isotopic purity of the 6 samples. The first column shows where each sample was prepared. The bold percentages denote which sample's purity is being reported in each line. The exception is the last line which corresponds to the purity of ^{Nat}Ge.

Germanium Sample Mass Fraction (%)						
Preparation Location	Purity	^{70}Ge	^{72}Ge	^{73}Ge	^{74}Ge	^{76}Ge
ANL	^{70}Ge Sample	**95.85**	4.09	0.04	0.02	-
ANL	^{72}Ge Sample	0.29	**98.2**	0.29	1.04	0.18
ANL	^{73}Ge Sample	0.005	1.36	**96.34**	2.29	0.005
LANL	^{74}Ge Sample	0.01	0.16	1.9	**97.53**	0.4
MAJORANA	^{76}Ge Sample	0.004	0.009	0.028	12.68	**88.1**
LANL	^{Nat}Ge Sample	20.52	27.45	7.76	36.52	7.75

corrections to the energy calibration for each run. An example of an alpha spectrum after fitting is shown in Figure 2.8.

2.4. Samples

A number of samples were chosen for this experiment. The experiment took place over two separate runs and the samples were procured before each run. The first experiment used $^{70,72,73}Ge$ and the second used $^{74,76}Ge$. Table 2.1 shows the isotopic purity of the germanium samples. In addition to the germanium isotopes, a ^{208}Pb sample is used to assess the effects of neutron scattering, and a ^{197}Au sample is used for normalization.

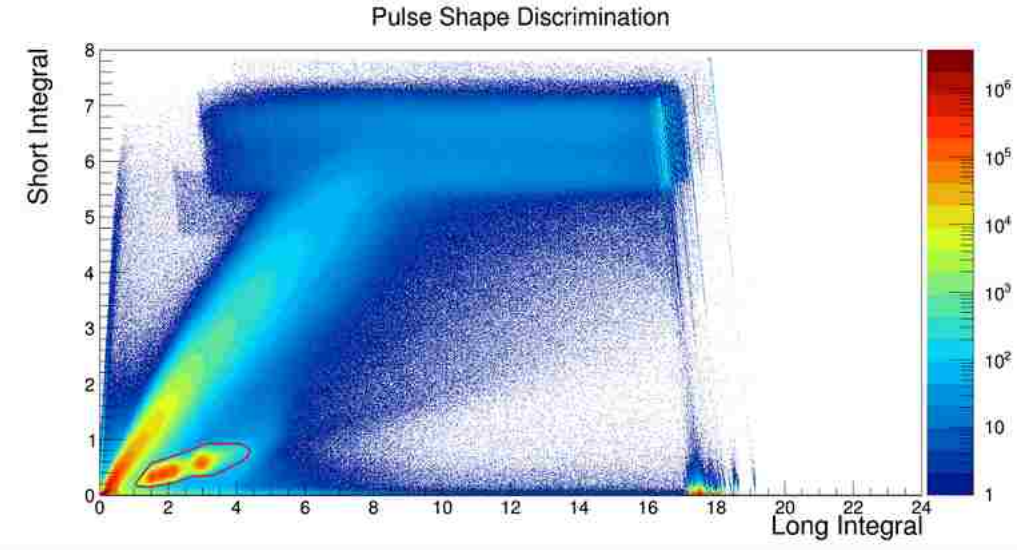

Figure 2.7. An example of a short integral vs long integral histogram generated from ^{74}Ge runs. The alpha events are outlined in red.

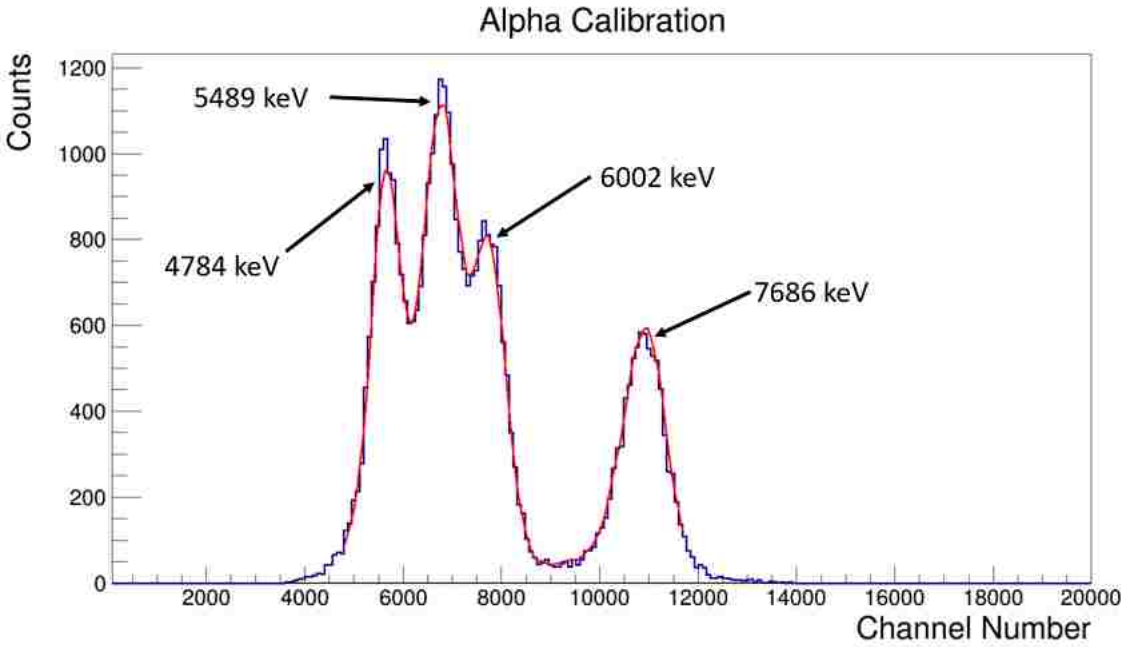

Figure 2.8. An example of an alpha spectrum in one BaF_2 crystal after the fitting has been performed for an energy calibration. The known alpha energies from the radium decay chain are shown on the graph.

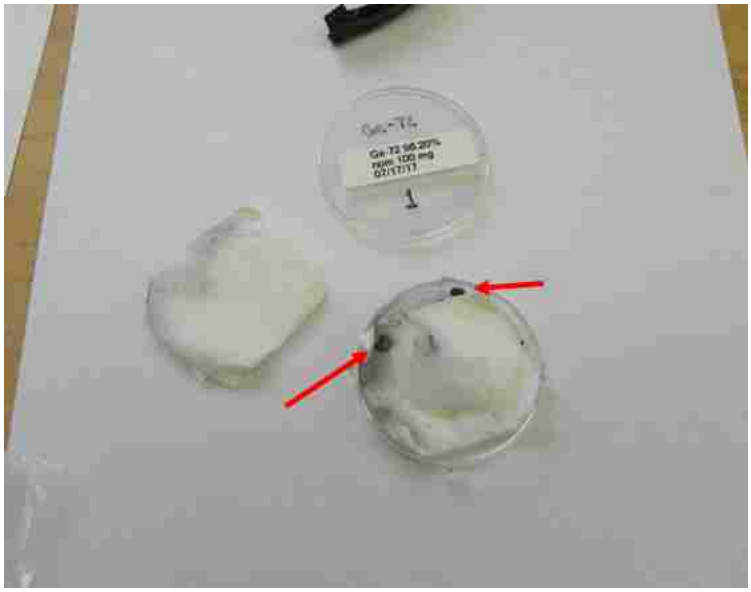

Figure 2.9. The damaged ^{72}Ge sample received at LANL. Two distinct layers can be seen here and a few others are amongst the padding.

The germanium samples used in the first experiments were fabricated from material supplied from Trace Isotopes as a metallic powder. The initial mass for each sample was 200 mg. The powder was then pressed at Argonne National Laboratory (ANL) into cylindrical pellets with approximately 5-mm radii. The pellets were shipped to Los Alamos National Laboratory (LANL). Despite careful packaging, upon arrival the pellets were determined to have been mildly damaged by the shipping process. The samples had splintered into flat, layered disks. An example of the damage sustained by the samples is shown in Figure 2.9. The pieces from each sample were carefully layered and sandwiched between kapton tape. The components used to assemble the samples were weighed before and after the assembly in order to determine the mass of material in each sample. Some pictures of the assembled samples are shown in Figure 2.10. Care must be taken when assessing the quantity of sample material that lies outside the central mass and was addressed using samples from the second experimental run.

Two samples for the second run (^{74,Nat}Ge) were fabricated at LANL using a slightly different technique in order to produce solid samples that would better hold together. We placed the powder samples in a press, compressed it in a clamp, placed the entire setup

Figure 2.10. The reassembled germanium samples. Some turned out better than others. The least important sample, ^{Nat}Ge (lower right), was assembled first and the most important, ^{72}Ge (upper left), was assembled last. This choice paid off as the most important sample wound up being the most intact.

into an oven, and pressed the sample under heat for 12 hours. Figure 2.11 shows the result of a sample pressed using this method. These samples are of much higher integrity than the fractured samples produced without heating. In order to determine the fraction of the previous samples that are not within the central mass, we compare the signatures of the fractured natural germanium sample to that of the solid sample. As mentioned previously, the only sample that was not produced using this metallic powder pressing method was ^{76}Ge. This sample was provided by collaborators at the MAJORANA project as a small chip off of their detector. Some finalized samples are shown in Figure 2.12.

2.5. Data Collection

The first component of the experiment was carried out over the course of 14 days in January of 2018. Between 4 and 5 days of data were collected on the ^{72}Ge sample, 3 days on ^{70}Ge, 2-3 days on ^{Nat}Ge, 1 day on ^{73}Ge, and 1 day on ^{197}Au. A significant amount of ^{208}Pb data was taken from an experiment that occurred earlier in the LANSCE run cycle. A similar time allotment for samples was chosen for the second component of the experiment.

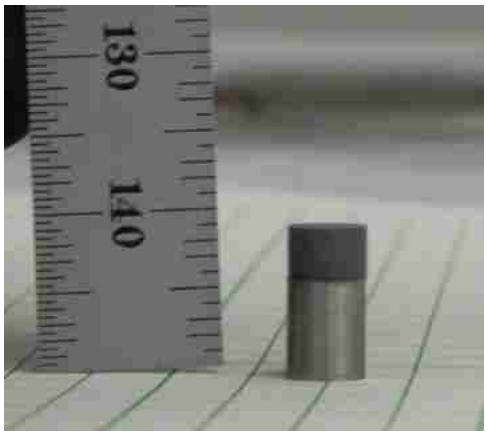

Figure 2.11. A sample of natural germanium produced using the heated press method. The sample (darker) sits atop the piston used in the press.

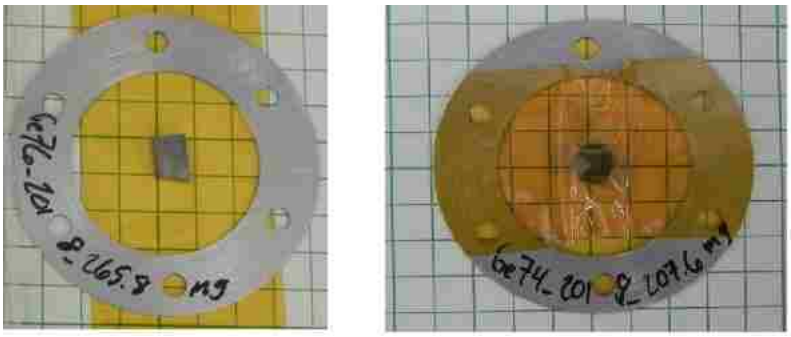

Figure 2.12. Left: the chip off of the MAJORANA detector serving as a ^{76}Ge sample. Right: the cylindrically pressed ^{74}Ge sample.

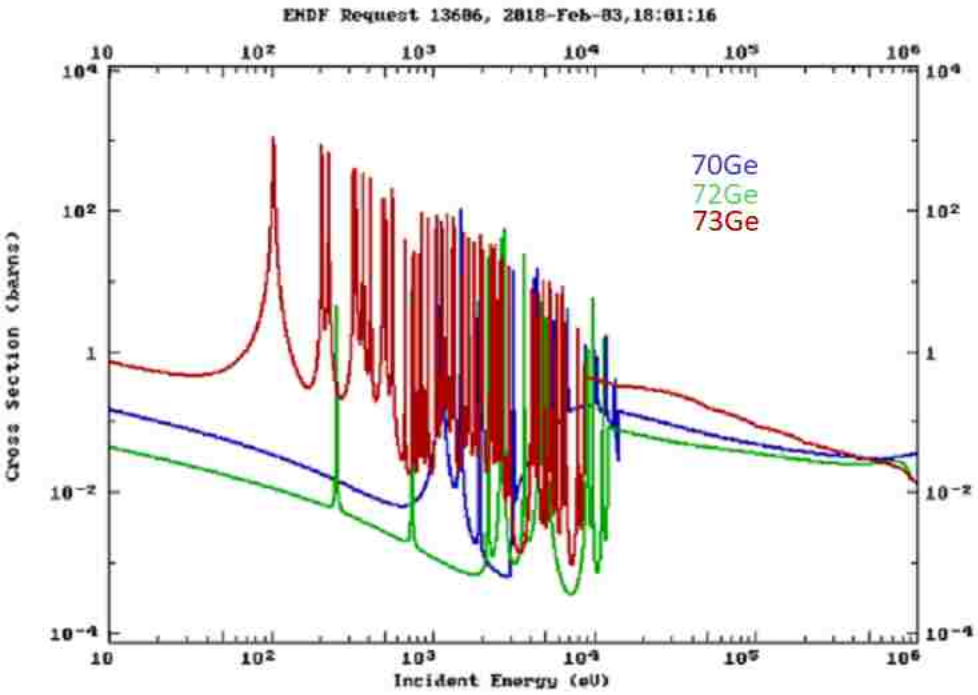

Figure 2.13. The evaluated (n,γ) cross-sections for ^{70}Ge, ^{72}Ge, and ^{73}Ge from ENDF.

About 6 days of beam time each were devoted to data collection with ^{74}Ge and ^{76}Ge, 2 days were devoted to ^{Nat}Ge, 4 days were devoted to ^{208}Pb, and 1 day of ^{197}Au data was taken.

Earlier it was mentioned that ^{Nat}Ge was the least important sample, but more time was spent collecting data for it than ^{73}Ge. Germanium has 32 protons so ^{72}Ge and ^{70}Ge are even-even nuclei. Because of pairing effects, this leads the neutron capture cross section for ^{73}Ge to be much larger than that of ^{70}Ge and ^{72}Ge. As a result, much less time is required to obtain sufficient statistics for ^{73}Ge. For reference, the evaluated cross sections for ^{70}Ge, ^{72}Ge, and ^{73}Ge from ENDF are provided in Figure 2.13. These cross sections are calculated using a combination of theoretical models and the limited experimental data for total cross sections (both neutron scattering and capture). The spectrum shown has been generated by knitting together two different evaluations, one for the resonance region and one for the unresolved region. These evaluated cross sections are useful for estimating expected count rates and relative influence of the different isotopes in a sample but are not actually measured directly.

Chapter 3. Data Analysis

The analysis for DANCE is relatively involved. A few concepts regarding the data should be explained before the analysis can be detailed. Because gamma rays often Compton scatter in one crystal and then deposit energy into one or more crystals, neighboring crystals that make simultaneous detections can be grouped as a cluster and treat them as likely a single gamma-ray detection. The cluster multiplicity refers to the number of clusters that make detections within the timing coincidence window. The sum of the energies detected from all clusters is called E_{sum}. The data is stored in a 3 dimensional histogram whose axes are E_{sum}, E_n (neutron energy), and M_{cl} (cluster multiplicity). It is instructive, however, to select a subset of multiplicities and project onto the E_{sum}-E_n plane. In Section 3.4 of this thesis selection of the multiplicity range is described. An example of the resulting 2 dimensional E_{sum}-E_n histogram is shown in Figure 3.1.

Since DANCE is a 4π calorimeter, entire gamma cascades are detected. This means that E_{sum} spectra will differentiate reactions based on the Q value of the reaction. A few examples of typical E_{sum} spectra are shown in Figure 3.2. These spectra are acquired by further projecting the 2 dimensional histogram obtained from multiplicity selection onto the E_{sum} axis. Because the detection efficiency is less than 100%, the E_{sum} spectra exhibit a peak just below the Q value and a sharp drop off above.

3.1. Background Subtraction

An important step in the process of analyzing this data was subtracting backgrounds. Each germanium sample contains varying impurities of the other stable germanium isotopes. Although the impurities are small, contributions from neutron capture on these impurities can still be significant especially in neutron energy regions containing resonances. In addition to isotopic contamination, additional background originates from neutrons that often scatter off the sample rather than capture in it. Many of these neutrons are passively suppressed by

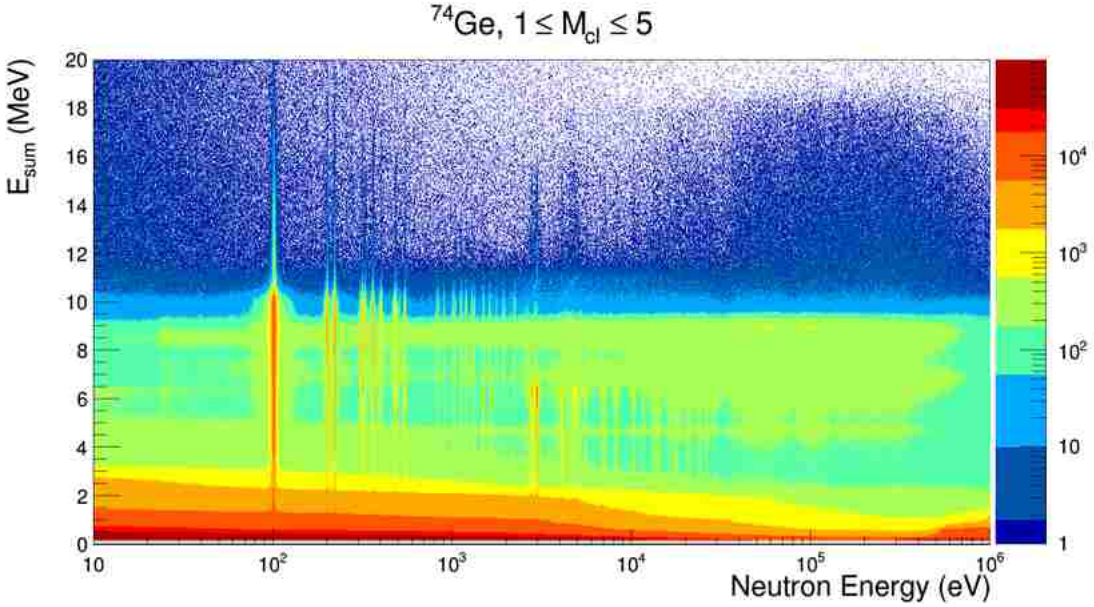

Figure 3.1. Shown here is the E_{sum}-E_n-M_{cl} histogram projected onto the E_{sum}-E_n plane for multiplicities 1-5.

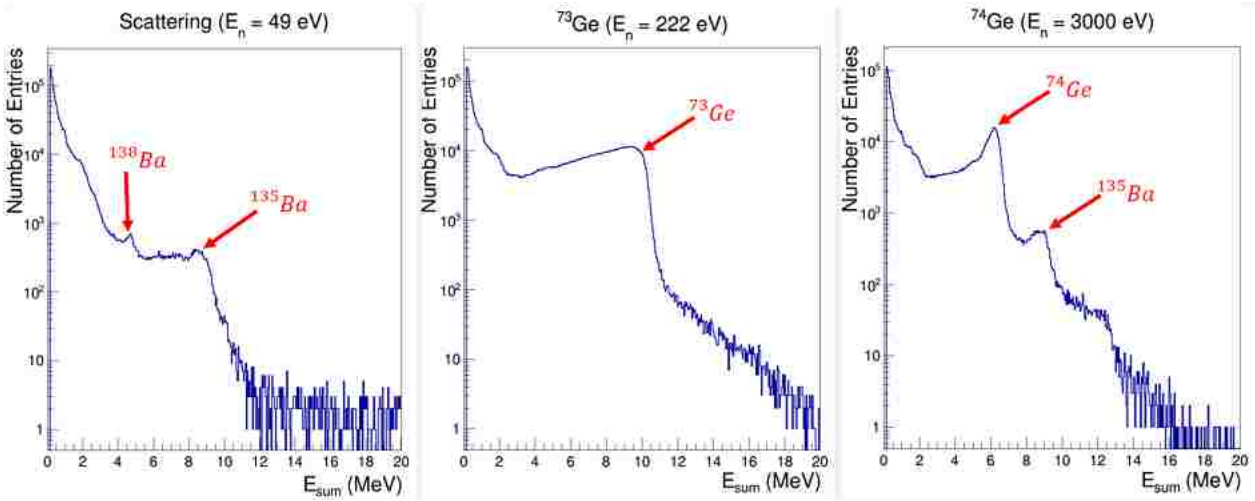

Figure 3.2. A few example E_{sum} spectra generated from the ^{74}Ge data. The neutron energy regions here have been chosen to display examples of various contributions in our data. Left to right: 1) scattering, 2) ^{73}Ge(n,γ), and 3) ^{74}Ge(n,γ).

a LiH shell surrounding the target location, nonetheless, some neutrons reach the detectors and present a background.

Neutron scattering produces a slightly different signature in the data than neutron captures do. When neutrons scatter off the samples, they are not detected directly by the BaF_2 but rather capture on the barium in the detector and cause gamma cascades of their own. As a result, rather than seeing resonances at certain incident neutron energies as vertical lines in the E_{sum}-E_n as with neutron captures in the sample, we see horizontal bands (continuous in E_n around E_{sum} energies corresponding to the neutron capture Q value of various barium isotopes. The main isotopes responsible for this background are ^{135}Ba (Q value: 9.107 MeV), ^{134}Ba (Q value: 6.973 MeV), and ^{138}Ba (Q value: 4.723 MeV).

Various backgrounds can be subtracted off using the Q value for each reaction to discriminate between background and data. In the absence of pileup, no counts at E_{sum} energies above the Q value for a reaction can be attributed to that reaction. Thus all counts above the Q value are from background sources whether from isotopic contamination or from neutron scattering. Therefore, the data above the Q value for neutron capture on our desired isotope can be fit and the degree to which each reaction contributes to the background below the Q value can be determined. The various background contributions can then be subtracted off using the scaling acquired by the fit. This procedure is applicable to backgrounds with Q values greater than the Q value for neutron capture to be measured. These backgrounds are subtracted one by one beginning with the highest Q value.

For demonstration purposes, the background subtraction process is outlined explicitly from the ^{74}Ge sample (Q value = 6.51 MeV). Using this procedure, ^{73}Ge (Q value = 10.20 MeV) is subtracted first and then scattering (Q value = 9.11 MeV) next working downward in Q value. The 2 dimensional histograms of E_{sum} vs E_n are iterated through on a bin-by-bin basis in neutron energy for both the sample of interest and the background sample. Projecting each neutron energy bin onto the y-axis, an E_{sum} histogram for both our sample of interest and the background sample are acquired. With a simple ratio of integrals over

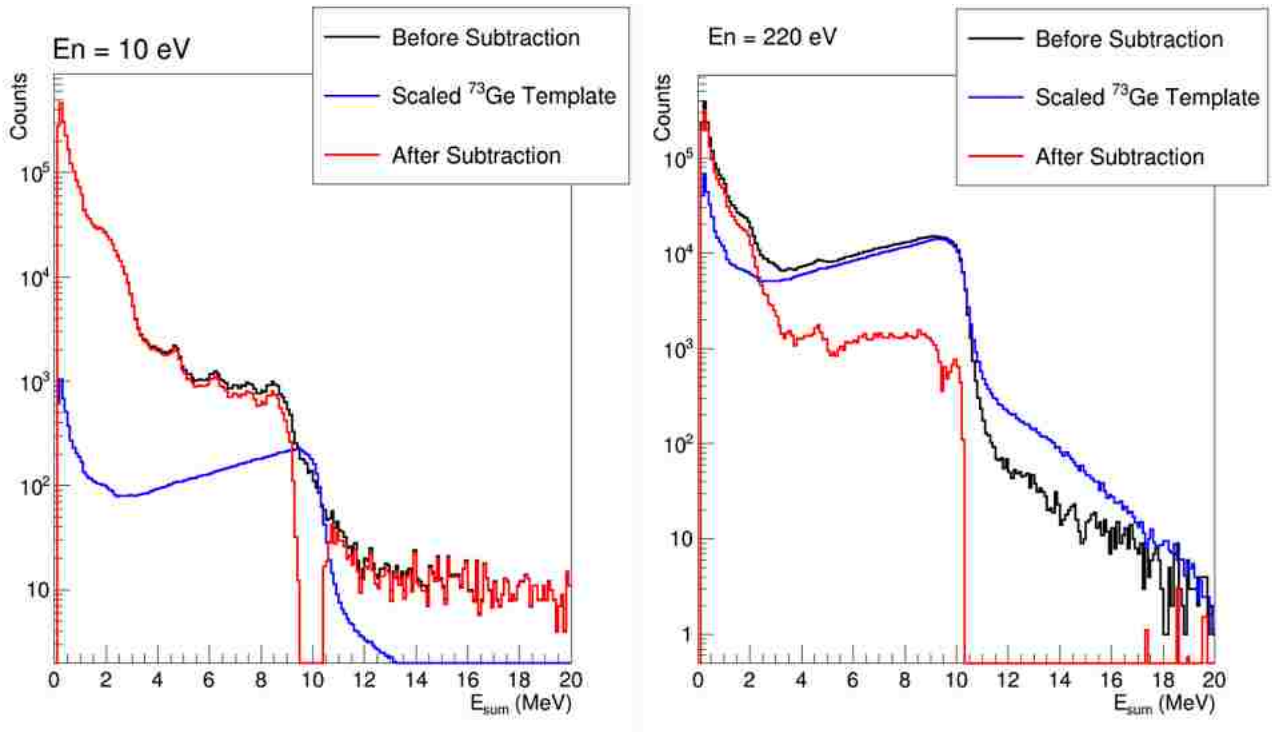

Figure 3.3. Examples of this ^{73}Ge background subtraction from data on the ^{74}Ge sample: Raw data (black), scaled ^{73}Ge spectrum (blue), and ^{74}Ge spectrum after background subtraction (red). Left: gated on neutron energies near 10 eV (away from all resonances). Right: gated on neutron energies near a ^{73}Ge(n,γ) resonances at 220 eV.

the relevant E_{sum} regions, the background signature can be scaled to match what appears in the sample of interest. Examples of the scaled E_{sum} histgorams produced during this procedure are shown in Figure 3.3. Note that oversubtraction in the high E_{sum} sometimes occurs but this has a negligible effect on the data in the E_{sum} region of interest below the capture Q value for ^{74}Ge. The results of this subtraction are shown in Figure 3.4. Once the ^{73}Ge is subtracted, the same procedure is performed for scattering background using our lead sample data. The results of that process for the ^{74}Ge sample are shown in Figure 3.5.

In the case of the ^{74}Ge example, the last remaining isotopes with greater than a 0.1% impurity are ^{72}Ge and ^{76}Ge. Due to the lower sample abundance and smaller cross section, the contribution from neutron capture on ^{72}Ge at its peak cross section to the overall yield is about 7% of the contribution from ^{76}Ge. Thus ^{72}Ge can be neglected. Since the Q value for ^{76}Ge is separated by only about 400 keV from that of ^{74}Ge, it is difficult to fit the

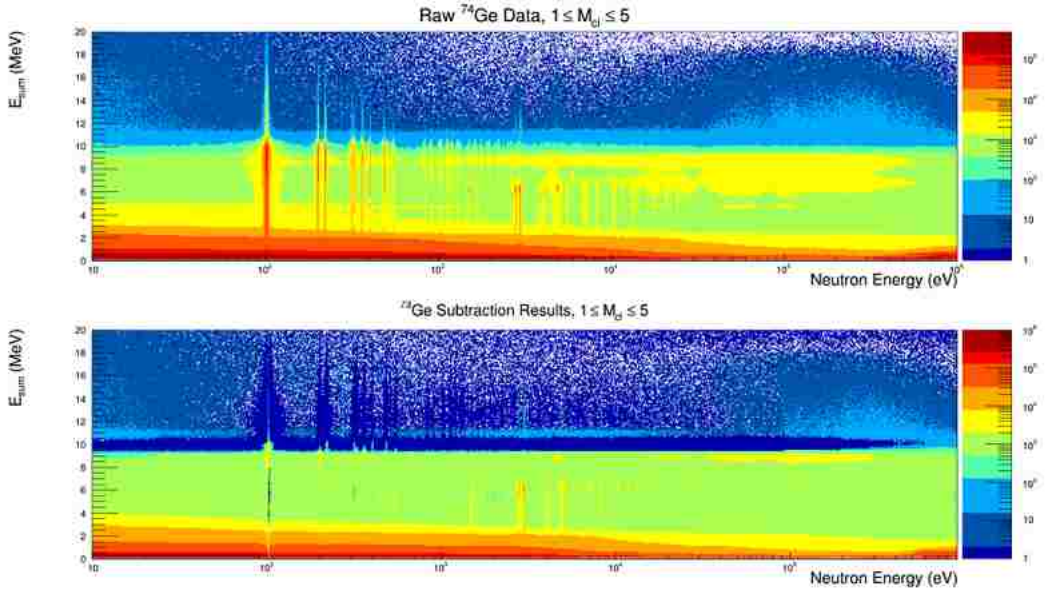

Figure 3.4. (Top) Raw E_{sum} vs neutron energy data for the ^{74}Ge sample. (Bottom) Same as above after subtracting ^{73}Ge(n,γ) background using the procedure described in text.

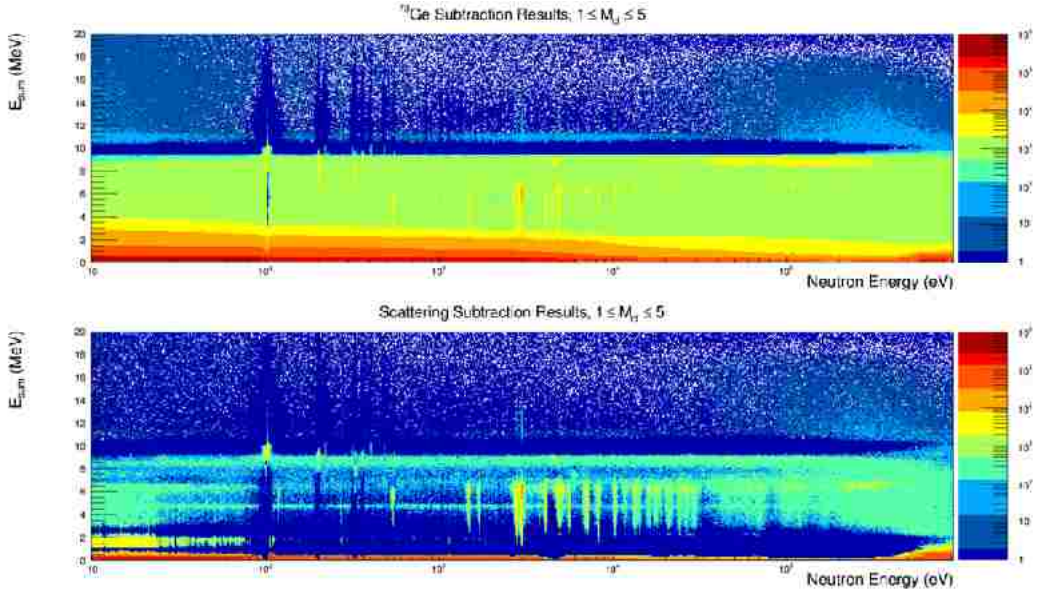

Figure 3.5. (Top) ^{73}Ge-subtracted E_{sum} vs neutron energy data for the ^{74}Ge sample. (Bottom) Same as above after subtracting scattering background using the procedure described in text.

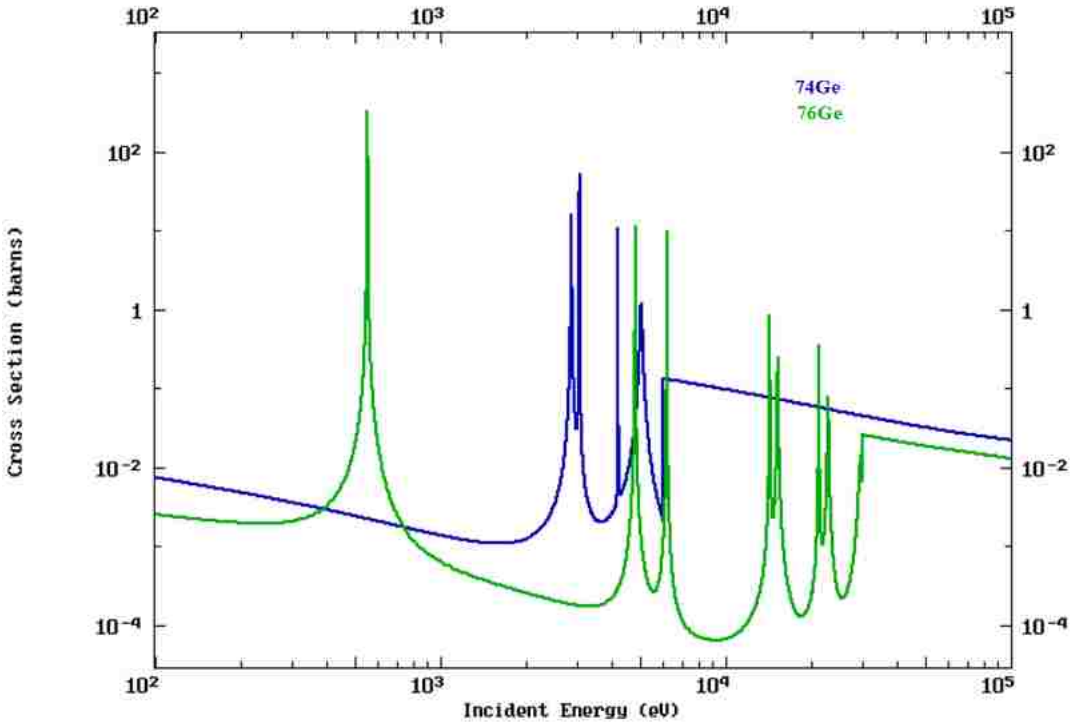

Figure 3.6. Evaluated neutron-capture cross sections for ^{74}Ge and ^{76}Ge from the ENDF database[21]. The prominent and isolated ^{76}Ge resonance around 500 eV is used for peak matching.

background in a bin-by-bin nature. Rather than proceed the same way as ^{73}Ge and scattering backgrounds, a different approach is needed. The contribution of ^{76}Ge to the overall yield in our sample can be determined by gating on a known resonance of ^{76}Ge and finding the scaling factor in a region where the contribution from ^{76}Ge in the ^{74}Ge data is enhanced. Even though the energy resolution of the detectors cannot distinguish the resonances of these two isotopes, evaluated cross sections help identify a prominent ^{76}Ge resonance to find the scaling factor. A comparison of the evaluated cross sections of ^{74}Ge and ^{76}Ge from the ENDF database is shown in Figure 3.6. A suitable resonance for peak matching must satisfy two conditions: 1) it must be a large resonance since the impurities in the samples are small, and 2) it must be isolated so that the overall yield in this energy region is dominated by neutron capture on the isotope causing the background (in this case, ^{76}Ge).

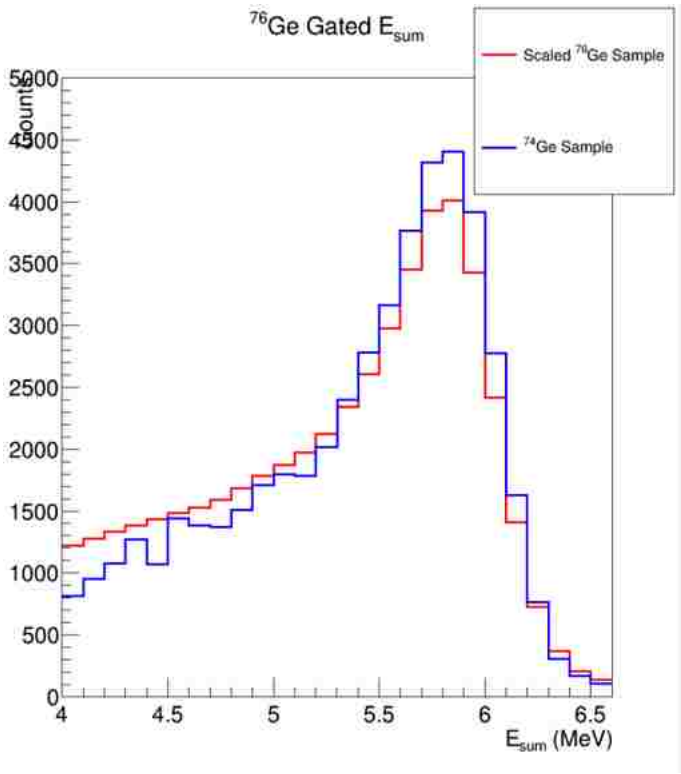

Figure 3.7. E_{sum} histograms from the ^{76}Ge resonance used to find a scaling factor for background subtraction. Note that the histogram from ^{76}Ge has been scaled here using the scaling factor determined for background subtraction.

In the case of ^{74}Ge, we can see in Figure 3.6 that the best ^{76}Ge resonance that satisfies our peak matching conditions occurs around 500 eV incident neutron energy. We gate on this resonance in neutron energy in both the ^{74}Ge sample and the ^{76}Ge sample data sets, project onto the y-axes to acquire E_{sum} histograms, and find a scaling factor for the subtraction by integrating over the relevant E_{sum} range. Figure 3.7 shows the peak-matched E_{sum} histograms from the ^{74}Ge and ^{76}Ge samples. Now that a scaling factor has been acquired, the entire ^{76}Ge E_{sum}-E_n histogram is scaled using this factor and subtracted from the ^{74}Ge sample we are trying to measure. A comparison of E_{sum} vs E_n spectra before and after this process is shown in Figure 3.8.

Although we have used ^{74}Ge as an example here, the process is very similar for all other germanium samples, with one exception. This process does not work for ^{73}Ge since its Q value at 10.20 MeV towers over even the scattering background Q values. Some discussion

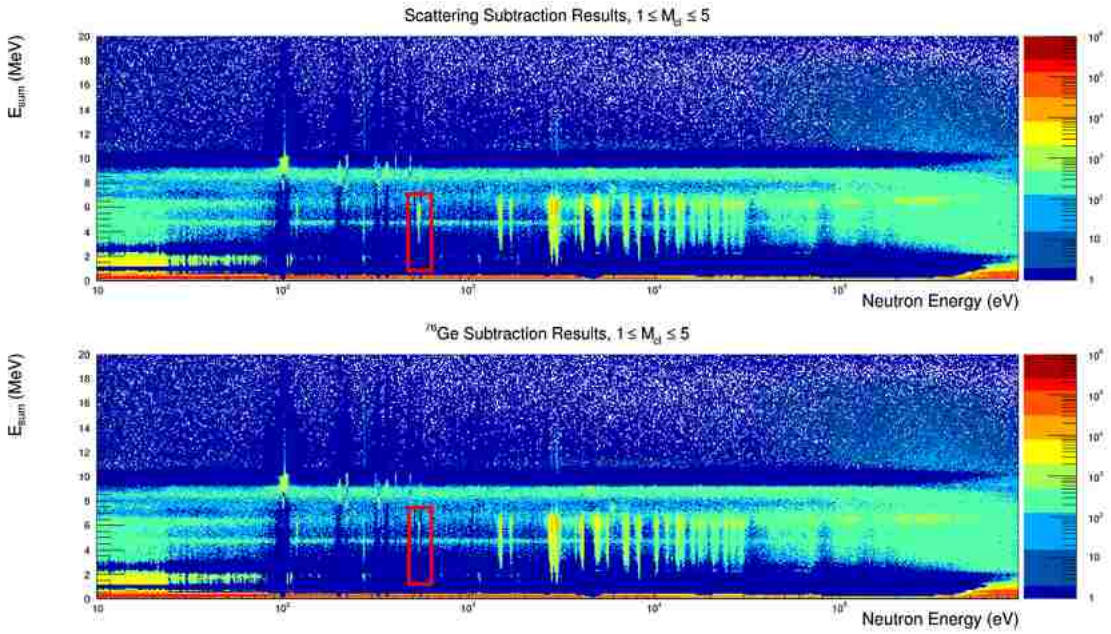

Figure 3.8. (Top) ^{73}Ge and scattering-subtracted data from the ^{74}Ge sample. (Bottom) The results of subtracting ^{76}Ge from the top spectrum. The ^{76}Ge resonance used to acquire the scaling factor is highlighted with a red box.

is devoted to a potential ^{73}Ge cross section measurement in Chapter 8 at the end of this thesis.

3.2. Neutron Flux Determination

In order to make an absolute cross section measurement, the yields must be normalized to the incident neutron flux for each energy bin. This is done using the information from the beam monitors. Additionally, the neutron flux at the beam monitor location needs to be normalized to the flux at the target location since the beam is slightly divergent. This is accomplished by using a thin gold target. Finally, corrections to the cross section are required to account for the use of thick targets. Thick targets attenuate the neutron beam at certain neutron energies due to the large total cross section.

3.2. Gold Normalization

Two beam monitors that are positioned about 2 meters downstream from DANCE are used to measure the neutron flux at their location; however, the flux at the beam monitors differs from that at the target location. In order to relate the neutron flux at the beam

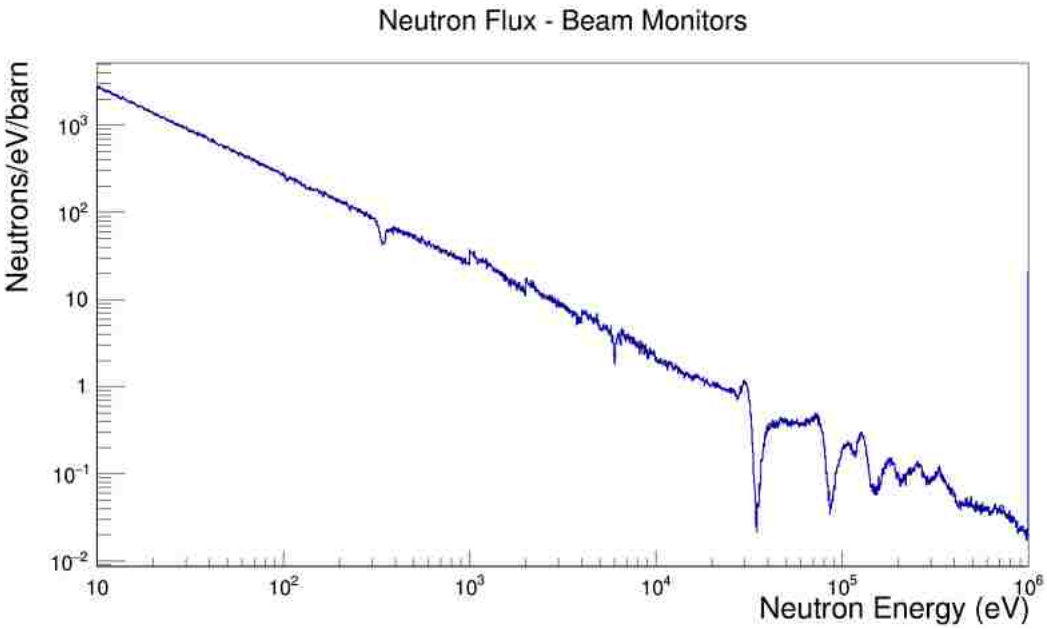

Figure 3.9. Neutron flux at flight path 14 as determined by the beam monitors downstream from DANCE.

monitors to the flux at the target location in DANCE, the cross section of an isotope with a well-known cross section is measured using the flux at the beam monitors. Then by fitting the resulting cross section measurement with the well known cross section, a scaling factor that relates the flux at the beam monitors to the flux at the target location is obtained. The isotope used for this purpose was ^{197}Au. A few things make ^{197}Au an ideal candidate for this procedure. First, it has a peak cross section of about 27 kilobarns at a low neutron energy resonance around 4.9 eV. The neutron flux at LANSCE, shown in Figure 3.9, is higher at lower neutron energies. The combination of ^{197}Au's large cross section and the location of this resonance at low neutron energy results in high statistics for this measurement. Consequently, we can use a very thin target and eliminate the need for corrections for self-shielding. The target used in this experiment was 5 kÅ thick as determined by Rutherford back scattering.

The cross section, $\sigma_{n,\gamma}^{Au}$, is calculated using the following formula where ϵ is the efficiency of detecting gamma rays after a neutron capture, Φ is the time-integrated neutron flux, N_{Au} is the number of gold atoms in the target, and $Y_{n,\gamma}^{Au}$ is the neutron capture yield:

$$\sigma_{n,\gamma} = \frac{1}{\epsilon\Phi}\frac{Y^{Au}_{n,\gamma}}{N_{Au}} \tag{3.1}$$

Making this measurement requires some analysis, specifically acquiring the proper capture yield. First, backgrounds need to be subtracted in order to ensure the calculated yield is exclusively due to capture. After this subtraction it was discovered that there was a low energy artifact in the background subtracted E_{sum} spectrum. This artifact is generated from retriggering on the tail of a legitimate gamma ray detection. In order to suppress this artifact, a blocking time is introduced. For a certain time period following a trigger, no data is recorded by DANCE. This removes the low-energy artifact caused by retriggering but develops the need for a dead time correction. Once a correction for dead-time is made, the capture yield and thus the cross section can be calculated.

3.2. Background Subtraction

Background subtraction on the gold sample data is more straightforward than with the germanium samples. Unlike the germanium samples, neutron capture on impurities in our gold sample form a negligible source of background. First, ^{197}Au is the only stable isotope of gold, so our stable sample contains no other gold isotopes. The only species in this sample are the original ^{197}Au and a small portion of ^{198}Hg which is born from β-decay of the ^{198}Au generated by neutron capture on the original sample. This small impurity can be ignored since the cross section for ^{197}Au is roughly five orders of magnitude larger than that of ^{198}Hg. With this in mind, the background is expected to be roughly linear in time of flight so our subtraction method will involve examining the background in the regions that neighbor the resonance of interest at 4.9 eV ($\sim$662 μs). By comparing the number of counts in the neighboring time-of-flight regions, we can acquire a slope for our linear background in the region of interest. A plot of this resonance in the time-of-flight regime with the background regions marked is shown in Figure 3.10. This slope will be used to scale the background at

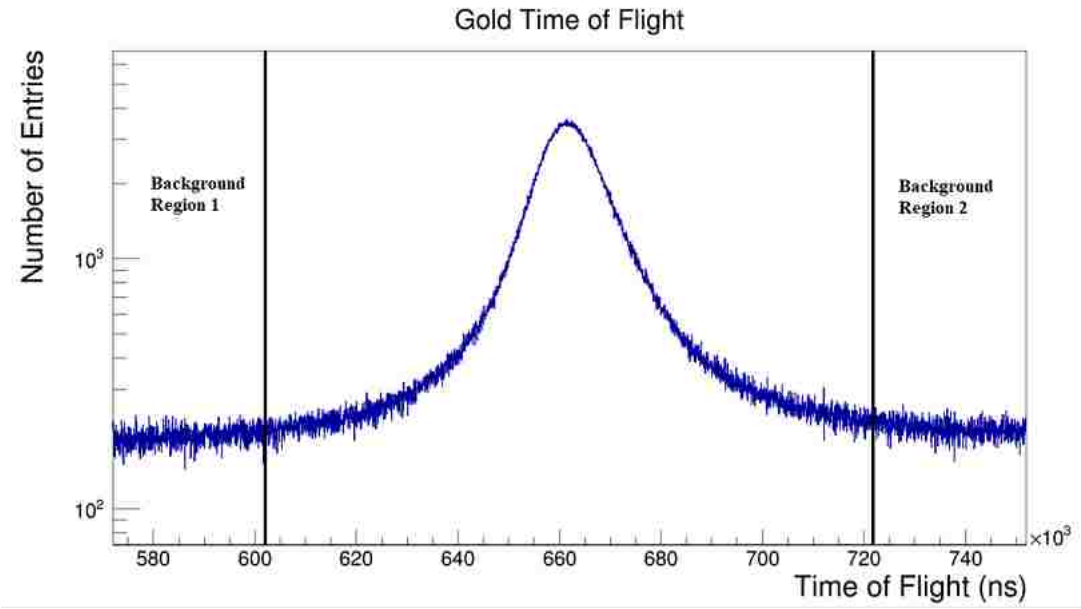

Figure 3.10. Raw yield of ^{197}Au in the time of flight regime. Neighboring regions used for background subtraction are shown on either side of the region of interest.

each neutron time-of-flight bin in our region of interest so that a background subtraction can be performed. An example of the E_{sum} results of this subtraction is shown in Figure 3.11.

3.2. Suppression of Retriggering

After subtracting the linear background, a low E_{sum} artifact was discovered that cannot be attributed to background. It appears only in the time-of-flight region where the capture cross section is large. If there is retriggering on the tails of legitimate gamma-ray detections then we expect a low energy signature to appear in the time-of-flight regions with the greatest number of neutron captures and thus gamma ray detections. This matches well with the low energy artifact we see. If this retriggering is indeed the source, the low energy artifact can be suppressed with the introduction of a blocking time in the data processing software. For a short time after a detection, we merely reject all other triggers that occur in DANCE. Background subtracted E_{sum} spectra using a variety of blocking times are shown in Figure 3.12. Note that the introduction of a blocking time of 1000 ns fully suppresses this retriggering phenomenon. It is important to suppress this low energy artifact because the efficiency of DANCE is roughly 100% to detect at least 150 keV of the gamma cascade

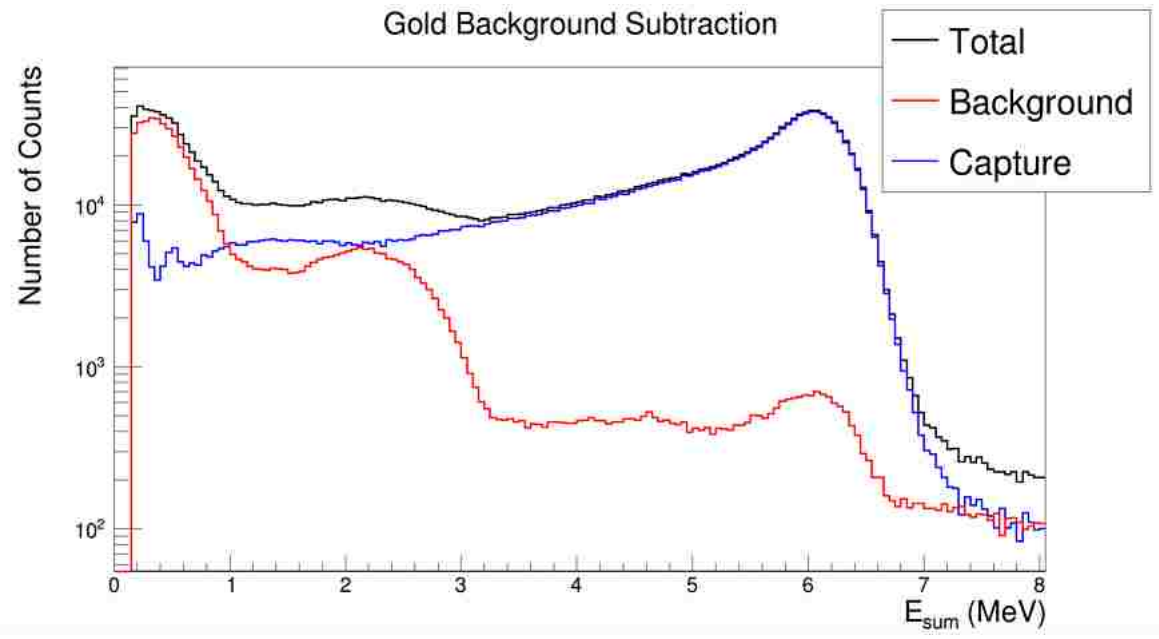

Figure 3.11. Results of the background subtraction for the gold sample. Includes the raw data, background scaled using our linear background assumption, and the results of the subtraction. Note: these spectra include the blocking time introduced in the section 3.2.3

following a neutron capture. So it is important to be able to confidently say that all of the counts, even at low E_{sum} energies, come from neutron capture and not some background or this low energy artifact.

With the introduction of a blocking time comes a need for one final correction to our gold data. During the blocking time DANCE vetoes all signals including legitimate capture events. A correction to the overall capture yield is applied to make up for the expected number of real capture events that occur during the blocking time and are thus discarded. If we consider the observed count rate per time of flight bin, C'_n, to be a function of the total number of counts, N_c, and the number of beam pulses, N_{t0} then we can use the process outlined by Jandel et al.[22] to account for dead time. The real count rate, C_n, with a dead time of τ_B can be calculated using:

$$C_n = -\ln\left(1 - \frac{C'_n}{1 - d_n}\right), \text{ where } d_n = \sum_{m=n-1}^{\frac{\tau_B}{\delta t}} C'_m \tag{3.2}$$

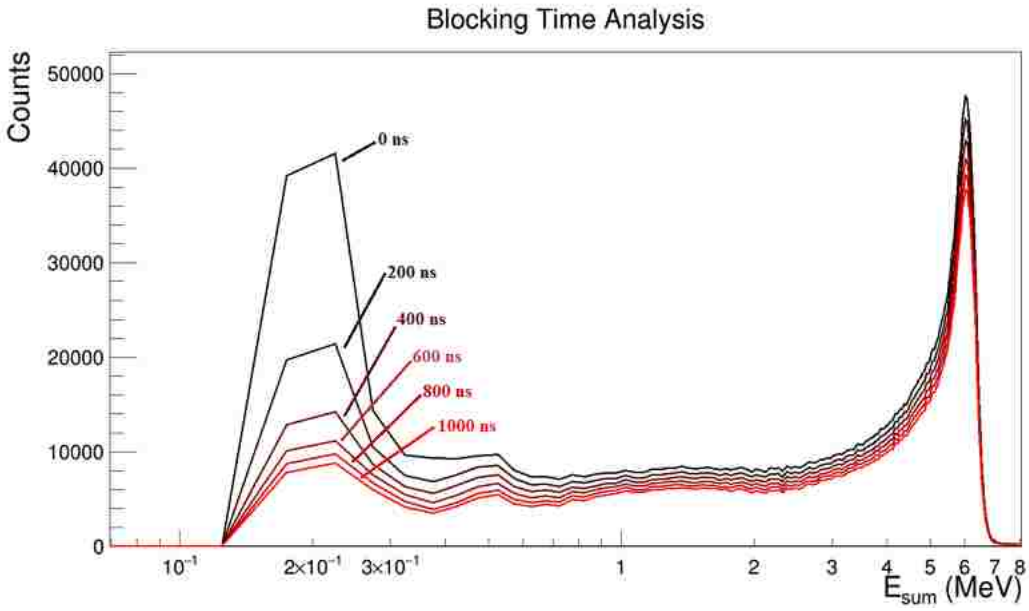

Figure 3.12. Background subtracted E_{sum} spectra using blocking times varying from 0-1000 ns. Note that the disappearance of the low energy artifact lends credence to the hypothesis that the artifact was born out of retriggering on legitimate gamma detections.

where δt is the time-of-flight bin width and C_n is the real count rate. A ratio of C_n/C'_n can be calculated using this formula for each time-of-flight bin in order to correct for the events lost during dead time. A plot of this ratio vs neutron energy is shown in Figure 3.13. As one might expect, away from the capture resonance region where the event rate is low the correction for dead time is correspondingly low. Likewise the correction increases as the cross section, and thus event rate, increases. This results in a peak correction factor of about 11%.

With this correction factor we have accounted for all backgrounds and idiosyncrasies to acquire a clean neutron capture yield in our gold sample. Now we can readily calculate the cross section using Equation 3.3 where Y_{Au} is the background subtracted yield from the gold target, d is the dead time correction factor, and σ_{BM} and Y_{BM} are the cross section and yield of the beam monitor, respectively;

$$\sigma_{Au} = d\frac{Y_{Au}}{N_{Au}}\frac{\sigma_{BM}}{Y_{BM}}. \tag{3.3}$$

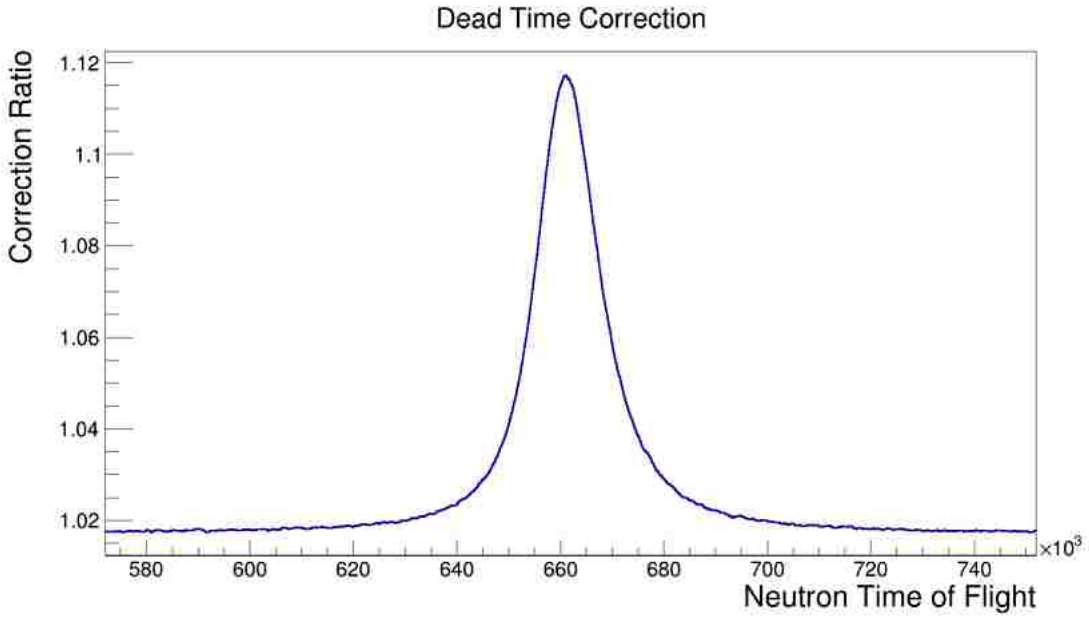

Figure 3.13. Dead time correction for the time-of-flight region corresponding to the 4.9 eV gold resonance.

Recall that this value represents the cross section of ^{197}Au using the neutron flux at the location of the beam monitors. This measured neutron flux differs from the flux at the target location by some multiplicative factor due to the divergence of the neutron beam. This factor carries over to our cross section measurement as well, so the next step is to fit our gold measurement to the well-known cross section. The multiplicative factor derived from this fit will ultimately relate the neutron flux at the beam monitors to the flux at the target location. The result of this fit is shown in Figure 3.14. The uncertainty from this fit is given by the output of the MIGRAD algorithm used to perform the fit. This uncertainty is negligible in comparison to the 4% uncertainty in gold atoms which is the dominating uncertainty for this particular measurement.

3.3. Thick-Target Corrections

The germanium samples used in these experiments are not exquisitely thin like the gold sample. Because of smaller cross sections, targets were made to be substantially thicker. A typical thickness for these samples was approximately 3 mm. With this thickness, on certain strong resonances neutrons can be scattered by the target and never reach the beam

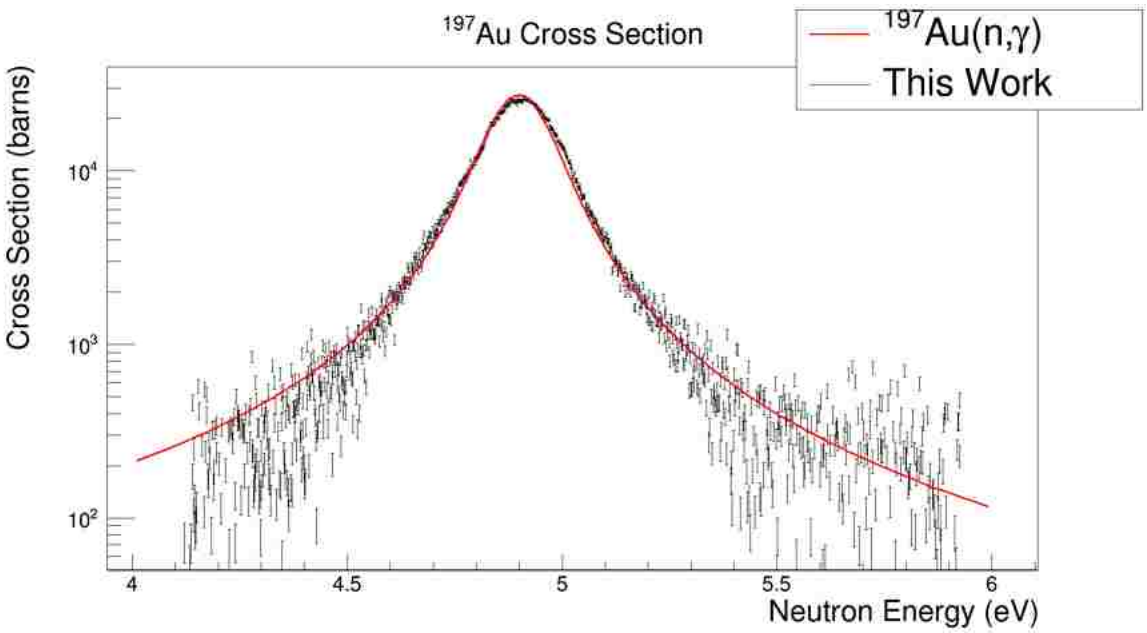

Figure 3.14. A comparison of the well known ^{197}Au cross section to that measured in this experiment. This is the result of fitting the multiplicative factor to match the measured cross section to the well-known values.

monitors to be included in neutron flux measurement. Corrections to the flux must be made to account for this attenuation effect. The number of neutrons attenuated in the target, dN, is a function of the number of incident neutrons, N, the total cross section, σ_{tot}, and the target thickness dx given in units of atoms per barn:

$$dN = -N\sigma_{tot}dx. \tag{3.4}$$

Using this equation we can derive the number of unreacted neutrons at a given location x inside the sample:

$$N(x) = N_0 e^{-\sigma_{tot}x}, \text{ where } N_0 = N(0). \tag{3.5}$$

By examining the neutron transmission through our sample, we can define parameters corresponding to an effective area and effective thickness of our target. Our samples have a diameter of 5 mm, and the beam has a diameter of about 1 cm at the target location.

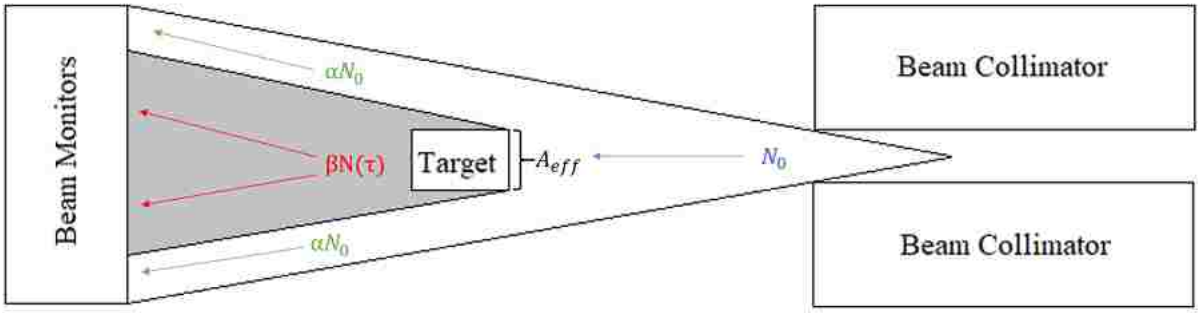

Figure 3.15. A schematic detailing the breakdown of neutrons detected by the beam monitors. Note: schematic not to scale.

Consider the number of neutrons detected by the beam monitors, N_{BM}, to be a function of the neutrons transmitted through our target, $N(\tau)$, and neutrons that missed the target, N_0. Using equation 3.5, we arrive at the following equation for the number of neutrons detected by the beam monitors:

$$N_{BM} = \alpha N_0 + \beta N(\tau) = N_0(\alpha + \beta e^{-\sigma_{tot}\tau}) \tag{3.6}$$

Figure 3.15 shows a schematic of neutrons being attenuated by the target, where α represents the portion of neutrons that miss the target, τ represents the target thickness, and β is related to the effective area A_{eff}. Mathematically, $\beta \approx \frac{A_{eff}}{A_{beam} - A_{eff}}$. We can use the evaluated total cross section from ENDF [21] to find the neutron energy with the highest transmission probability. At this neutron energy we can determine a normalization constant to relate N_{BM} to N_0 which allows us to simplify Equation 3.6 using $\alpha = 1 - \beta$. With this simplification we arrive at the following equation:

$$f_a = \frac{N_{BM}}{N_0} = 1 - \beta + \beta e^{-\sigma_{tot}\tau} \tag{3.7}$$

In order to determine the β and τ parameters, we fit this curve determined by the evaluated total cross section to our experimental data around the largest resonance. For our ^{74}Ge example this takes place right around 5 keV neutron energy. Effectively, the β

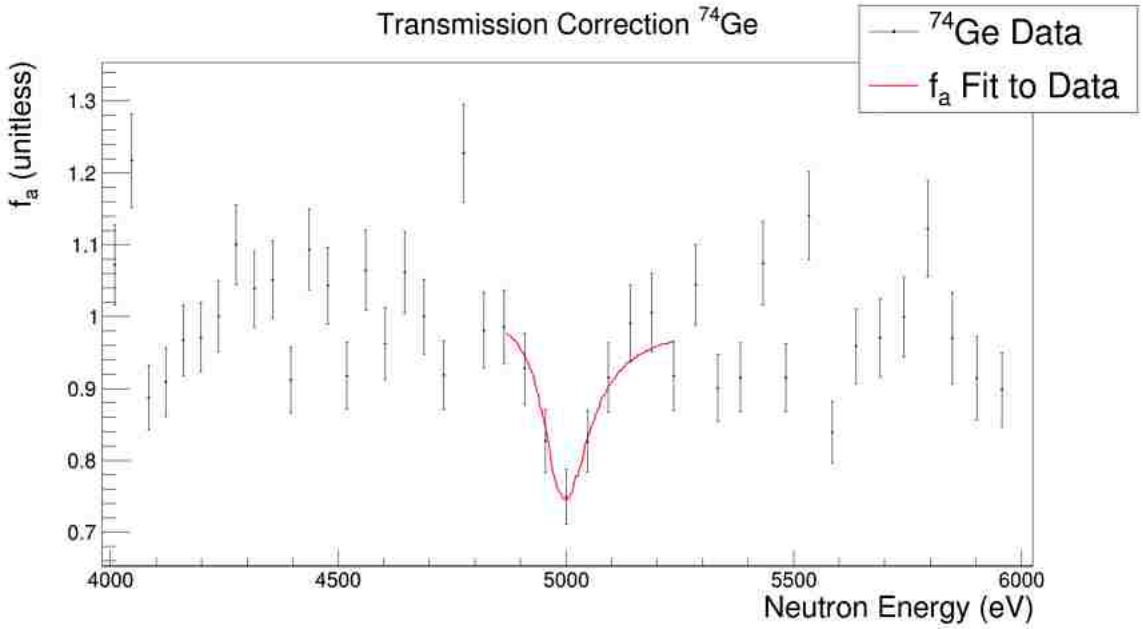

Figure 3.16. The fit for β and τ to the experimental data for ^{74}Ge. This is the most defined and prominent resonance in the ^{74}Ge total cross section and makes an ideal fitting candidate.

parameter determines the depth of resonances and the τ parameter determines the width. The fitted data points for our ^{74}Ge sample are shown in Figure 3.16.

In this case, the fit determined parameter values of $\beta = 0.33 \pm 0.13$ and $\tau = 0.0028 \pm 0.0019$ barns^{-1}. Knowing that $\beta \approx \frac{A_{eff}}{A_{beam} - A_{eff}}$ and that our neutron beam profile is roughly constant with a diameter of 1 cm at the target location, we can calculate the effective area of our target. For the example of ^{74}Ge, we find that the effective area is $A_{eff} = 0.194 \pm 0.06$ cm^2. This effective area both agrees with our measured sample area of 0.196 cm^2 and falls entirely within the effective beam area of 0.785 cm^2. The broader results of this fitting process for ^{74}Ge are shown in Figure 3.17. As Figure 3.18 shows, the neutron transmission corrections are actually quite small in the astrophysically relevant energies of 30 and 90 keV, so these corrections will make a relatively small impact to the Maxwellian-averaged cross sections. As such, the important results of these calculations are confirmations that the sample had a realistic effective area and was completely within the homogeneous section of our neutron beam.

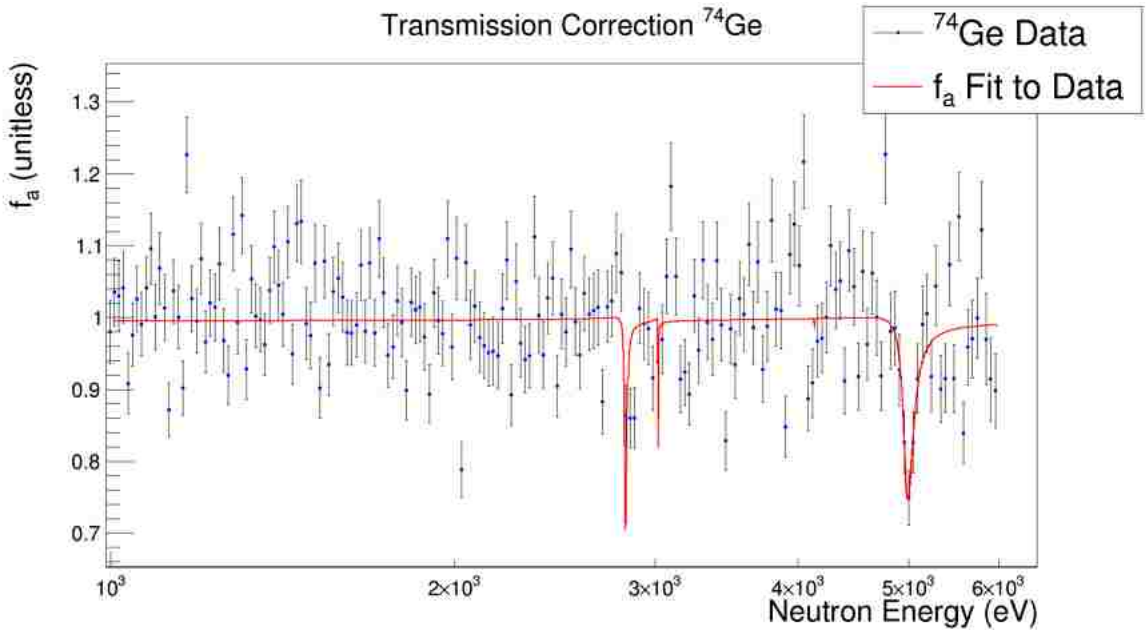

Figure 3.17. The overall results of the fit of β and τ in the transmission probability including the experimental data for ^{74}Ge.

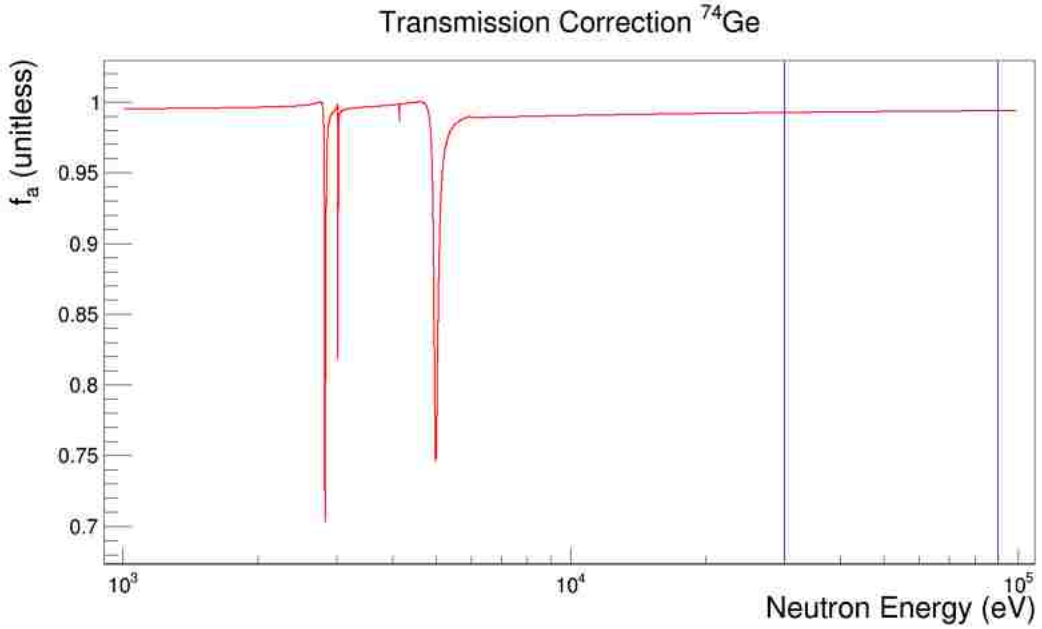

Figure 3.18. A broad spectrum of the neutron transmission corrections for our ^{74}Ge sample. The two vertical lines correspond to the astrophysically relevant neutron energies at 30 and 90 keV.

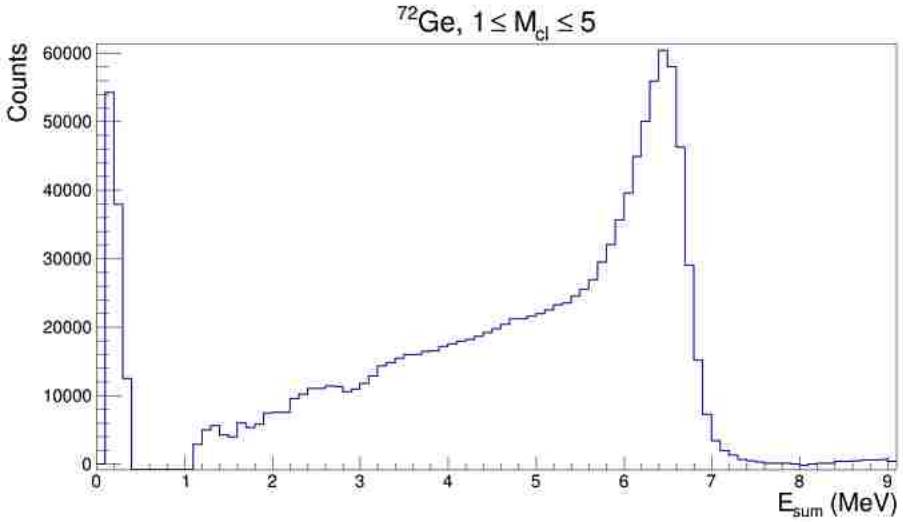

Figure 3.19. Background subtracted E_{sum} spectrum centered on a capture resonance for ^{72}Ge. Around 3 MeV the E_{sum} tail becomes less well behaved because of a low signal-to-background ratio in the low E_{sum} energy range. This region is excluded in the final analysis and requires efficiency corrections.

3.4. Detector Efficiency

Recall that in the case of gold normalization, the efficiency of DANCE is very nearly 100%. This is unfortunately not the case for the germanium data because of a low signal-to-background ratio in the low E_{sum} energy region. This feature is displayed in an example E_{sum} spectrum from ^{72}Ge shown in Figure 3.19.

When integrating over E_{sum} histograms to calculate the yield, a restricted subset of energies must be chosen that excludes the low-energy region compromised by the background subtraction. We choose a lower edge E_{sum} cutoff energy and then integrate to the Q value for the reaction to acquire the yield. Since we are calculating the yield from only a portion of the region containing real events, our adjusted efficiency must be calculated. This is done using a suite of simulation software made up of two components: DICEBOX and Geant4. DICEBOX is an algorithm used for generating gamma cascades from neutron capture[23]. A chosen excitation energy, called E_{crit}, is determined, below which all level information is well known. For excitation energies above E_{crit} where level information is missing, a random discretization of a continuous level density model is used to approximate the levels. The

gamma cascades generated by DICEBOX are then used as input for a Geant4 simulation. Geant4 is used to model the detection of the simulated gamma cascade by DANCE. By applying the same multiplicity and E_{sum} cuts to the simulated data, we determined the efficiency of detecting a gamma ray from neutron capture in our restricted E_{sum} range.

In order to produce accurate simulations of neutron capture on germanium nuclei, we collaborated with physicists at Charles University in Prague, Czech Republic who model the level schemes of nuclei for DICEBOX simulations[24]. Parameters used for the input to DICEBOX are determined by comparing the energy distribution of gamma rays for different cluster multiplicities. Multi-Step Cascade (MSC) spectra were produced for capture resonances of each germanium isotope. By gating on the Q value for the reaction, we can suppress all backgrounds for this data. These show the energy distribution of gamma rays for a given multiplicity and inform the choice of the level density model for input to the DICEBOX simulations. A preliminary example of several such distributions is shown in Figure 3.20.

The output for DICEBOX is used to model the detection response of DANCE in a Geant4 simulation. Using this method, the effect of different E_{sum} cutoff energies on the efficiency correction was investigated. A plot of these corrections calculated for a similar experiment is shown in Figure 3.21[25]. As expected, higher cutoff energies lead to lower efficiencies. Thus the cutoff energies were chosen to be as low as possible while still omitting the compromised lower energy region. Additionally, the shape of the E_{sum} spectrum on different resonances depends on the spin-parity of the level being populated. An important result of previous simulation efforts was showing that inclusion of multiplicity 1 events removes the efficiency's dependence on the spin-parity of the populated state[25]. Removing the efficiency's dependence on spin-parity is crucial so that one efficiency correction can be applied across the neutron energy spectrum.

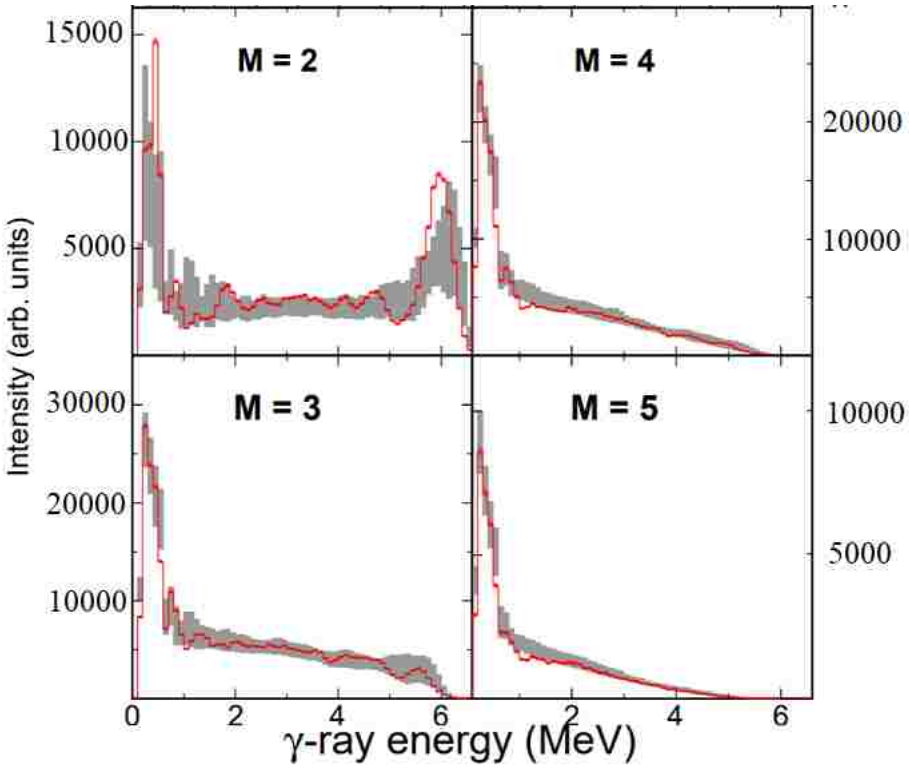

Figure 3.20. A preliminary comparison of MSC spectra for ^{72}Ge. The red curves are Q value gated data and the gray shadows show the spectra generated using DICEBOX. The width of the DICEBOX curves show the uncertainty in the simulations.

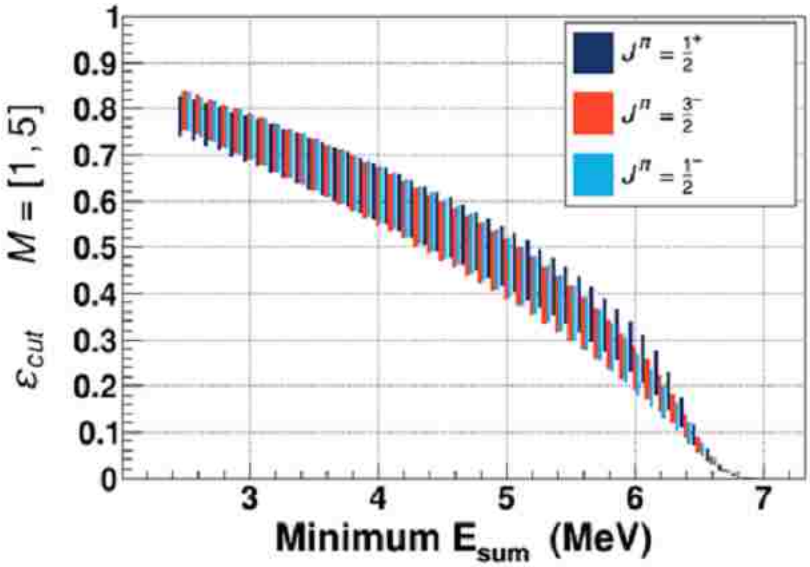

Figure 3.21. Efficiency corrections vs minimum E_{sum} calculated for ^{68}Zn(n,γ) by Kevin Macon[25]. The vertical bars show the uncertainty of the efficiency result.

Chapter 4. Cross Section Results

First recall the equation needed to calculate the neutron capture cross section in a DANCE experiment:

$$\sigma_{n,\gamma} = \frac{1}{\epsilon\kappa f_a}\frac{Y_{n,\gamma}}{N_{Ge}}\frac{\sigma_{BM}}{Y_{BM}}. \tag{4.1}$$

Here ϵ is the detection efficiency for the energy cuts as determined by simulation, κ is the neutron flux normalization factor, f_a is the thick-target correction factor, σ_{BM} and Y_{BM} are the cross section and yield of the beam monitors, respectively, $Y_{n,\gamma}$ is the background subtracted DANCE yield, and N_{Ge} is the number of germanium atoms. Using the measured neutron-capture cross sections, Maxwellian-averaged cross sections (MACS) were determined. MACS are essential to determining the stellar reaction rate of an s-process isotope, so a comparison of this work to current evaluated MACS is also presented. As with any scientific measurement, proper calculation and propagation of error is essential to achieve correct and meaningful results. The uncertainties in the cross-section measurements come from a few sources. First, the uncertainty in the counts recorded by both DANCE and the beam monitors are calculated assuming Poisson statistics. There is also uncertainty associated with the flux normalization factor, which is dominated by the uncertainty in the number of gold atoms determined through Rutherford scattering. Finally, there is uncertainty associated with the efficiency calculations. For these cross section measurements, the efficiency calculation dominates the overall uncertainty.

Figure 4.1 shows the neutron capture cross section for ^{74}Ge measured in this work compared to the evaluated cross section made by Iwamoto *et al.* in the ENDF database[26]. This evaluated cross section is divided into two regions at 6 keV neutron energy. Below 6 keV is known as the resonance region. The cross section was evaluated using Breit-Wigner formalism where resonance energies and widths were modified to reproduce the measured total cross section of natural germanium. From neutron energies above 6 keV the evaluated

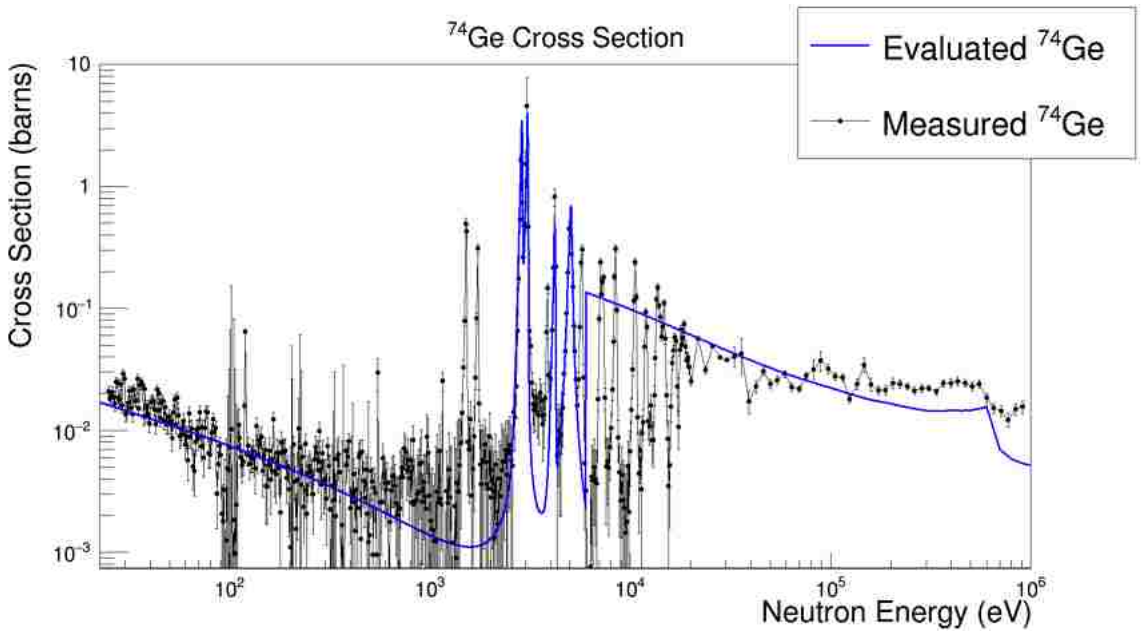

Figure 4.1. Neutron capture cross section of ^{74}Ge compared to the ENDF/B-III.0 evaluated cross section from the NNDC database.

cross section is calculated using an optical model fit to the previously available experimental data. The neutron energy resolution of the evaluated cross sections presented in this thesis were broadened using the R-matrix code SAMMY[27][28]. Note that portions of this measurement where the cross section is small have comparatively large uncertainties. This is due largely to the lower statistics in these regions. However, these regions do not contribute significantly to the Maxwellian-averaged cross section since it will be dominated by the resonances and the neutron energy regions closer to the astrophysically relevant energy regions ($kT = 30$ keV and $kT = 90$ keV).

The energies of neutrons in a stellar environment is described by a Maxwell-Boltzmann distribution dependent on the temperature. By folding the Maxwellian-distributed neutron energies with the measured neutron-capture cross section, a Maxwellian-averaged cross section is calculated. This value is used in astrophysical models to produce s-process abundance curves. The MACS is calculated using the following equation:

Table 4.1. A comparison of this work to previous values for MACS with kT energies ranging from 5 keV to 100 keV for ^{74}Ge.

^{74}Ge MACS Comparison			
kT (keV)	This Work $\langle\sigma\nu\rangle$ (mb)	NNDC[21] $\langle\sigma\nu\rangle$ (mb)	KADoNiS[29] $\langle\sigma\nu\rangle$ (mb)
5	92.2 ± 22.9	120.3	106
10	61.2 ± 7.9	86.6	70.2
20	43.1 ± 2.7	58.0	46.9
30	37.1 ± 1.9	45.5	37.6 ± 3.9
40	34.1 ± 1.6	38.5	32.6
50	32.2 ± 1.4	33.89	29.0
60	30.9 ± 1.3	30.7	26.3
70	29.9 ± 1.2	28.4	
80	29.1 ± 1.1	26.6	23.4
90	28.5 ± 1.1	25.1	
100	27.9 ± 1.0	24.0	22.0

$$\begin{aligned}\langle\sigma\nu\rangle &= \frac{2}{\sqrt{\pi}}\frac{1}{(kT)^2}\int_0^\infty \sigma(E_n)E_n e^{-E_n/kT}dE_n \\ &\approx \frac{2}{\sqrt{\pi}}\frac{1}{(kT)^2}\sum_a^b \sigma_{E_n}E_n e^{-E_n/kT}\delta E_n\end{aligned} \tag{4.2}$$

This approximation is necessary since our results give the neutron capture cross section in discrete points as opposed to a continuous function of energy. Additionally the cross sections were measured in the energy region of 10 eV to 1 MeV, rather than across all possible energies. Nonetheless, this approximation is a very good one because the vast majority of neutrons at the astrophysically relevant temperatures will have energies well within this range. MACS were calculated for kT energies ranging from 20 keV to 100 keV using our measured neutron capture cross section. A comparison between this work and previous values from National Nuclear Data Center (NNDC)[21] and Karlsruhe Astrophysical Database of Nucleosynthesis in Stars (KADoNiS)[29] is provided in Table 4.1.

A few notable conclusions can be drawn by comparing these values. First, MACS calculated using this work generally agree with the KADoNiS values but have smaller uncertainties. Recall that a main motivation for performing these measurements was to reduce the

uncertainty in s-process abundance predictions. Second, we can see that both the NNDC and the KADoNiS values seem to be more heavily dependent on kT. In the case of KADoNiS, the only directly measured MACS was at 30 keV using the activation technique. The other reported values are inferred rather than directly measured[30]. The NNDC values are based on theoretical models and limited experimental cross section data at high energies. Since we performed a direct measurement of the neutron capture cross section via the neutron time-of-flight method, our calculated MACS do not rely on this extrapolation method to acquire values at different thermal energies. This is particularly important for the MACS at $kT = 90$ keV that has never been directly measured until now. Recall that the weak s-process happens during two stages: helium burning and carbon burning. KADoNiS contains measured MACS for helium burning at $kT = 30$ keV but this work is the first direct measurement of the MACS for carbon burning at $kT = 90$ keV.

Chapter 5. Results for Other Isotopes

The previous chapter showed only the results for the analysis process applied to our arbitrarily chosen example isotope, ^{74}Ge. The results for the remaining even-even stable germanium isotopes are presented in this chapter. Figures 5.1, 5.2, and 5.3 show the final results for the rest of the germanium isotopes.

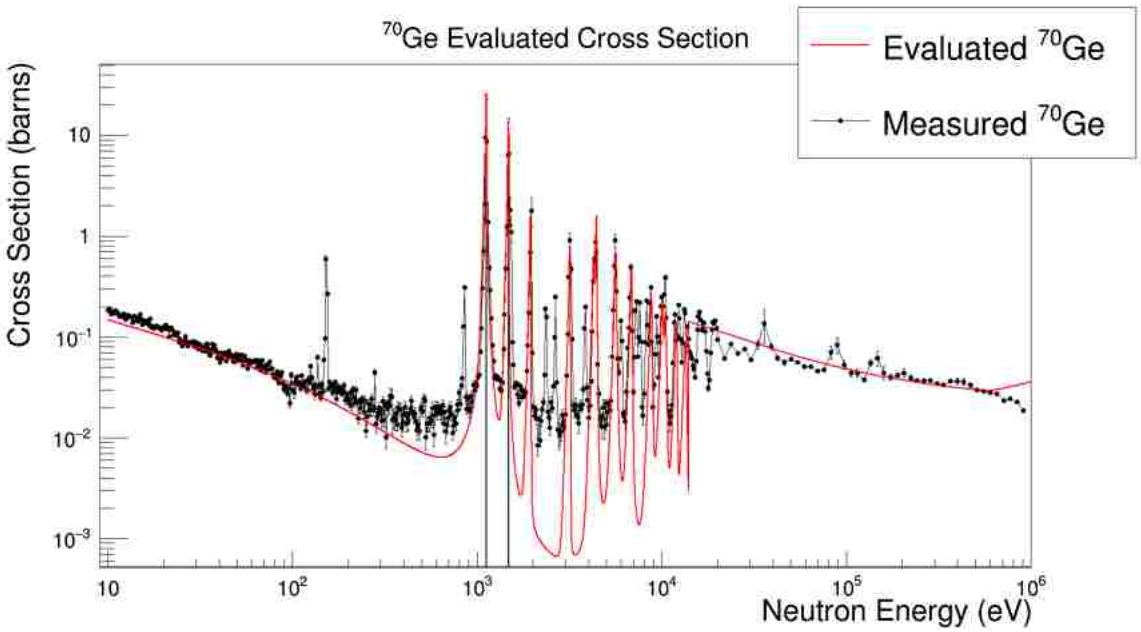

Figure 5.1. Neutron capture cross section of ^{70}Ge compared to the ENDF/B-III.0 evaluated cross section from the NNDC database.

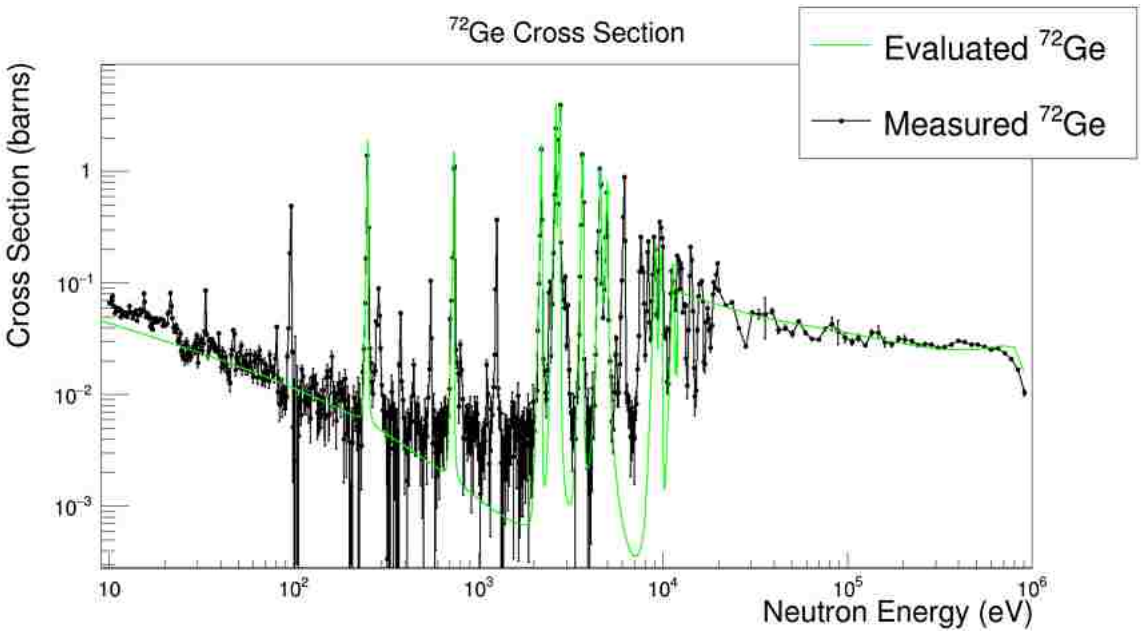

Figure 5.2. Neutron capture cross section of ^{72}Ge compared to the ENDF/B-III.0 evaluated cross section from the NNDC database.

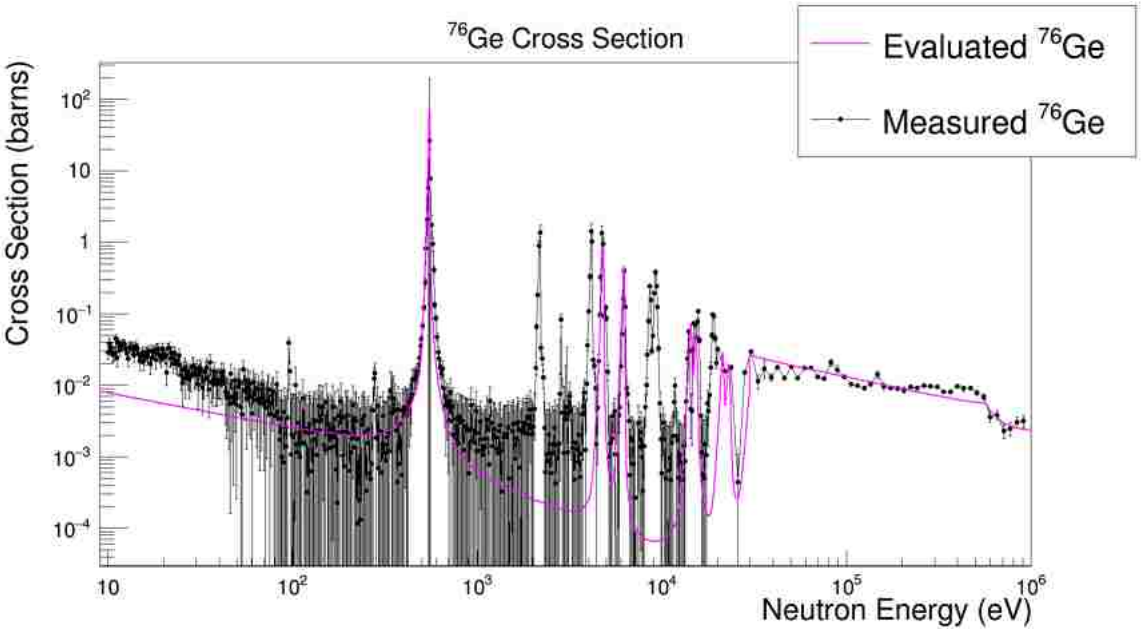

Figure 5.3. Neutron capture cross section of ^{76}Ge compared to the ENDF/B-III.0 evaluated cross section from the NNDC database.

Just like we did for ^{74}Ge, once we determined the neutron capture cross sections the next step was to calculate the MACS. The results of those calculations are shown in Tables 5.1, 5.2, and 5.3.

Table 5.1. A comparison of this work to previous values for MACS with kT energies ranging from 5 keV to 100 keV for ^{70}Ge.

^{70}Ge MACS Comparison			
kT (keV)	This Work $\langle\sigma\nu\rangle$ (mb)	NNDC[21] $\langle\sigma\nu\rangle$ (mb)	KADoNiS[29] $\langle\sigma\nu\rangle$ (mb)
5	158.9 ± 34.5	208	201
10	117.2 ± 10.0	155.2	145
20	89.2 ± 3.7	110.1	106
30	77.0 ± 2.5	89.4	88 ± 5
40	69.8 ± 2.0	77.4	75
50	64.8 ± 1.7	69.5	69
60	61.0 ± 1.5	63.8	63
70	58.0 ± 1.3	59.6	
80	55.5 ± 1.2	56.3	55
90	53.4 ± 1.1	53.7	
100	51.5 ± 1.0	51.5	49

Table 5.2. A comparison of this work to previous values for MACS with kT energies ranging from 5 keV to 100 keV for ^{72}Ge.

^{72}Ge MACS Comparison			
kT (keV)	This Work $\langle\sigma\nu\rangle$ (mb)	NNDC[21] $\langle\sigma\nu\rangle$ (mb)	KADoNiS[29] $\langle\sigma\nu\rangle$ (mb)
5	143.0 ± 16.0	101.5	199
10	97.1 ± 5.5	76.3	133
20	65.8 ± 2.8	60.5	91
30	54.3 ± 2.2	53.1	73 ± 7
40	48.4 ± 1.9	48.5	63
50	44.9 ± 1.7	45.2	57
60	42.5 ± 1.6	42.7	52
70	40.7 ± 1.4	40.8	
80	39.4 ± 1.3	39.3	47
90	38.3 ± 1.2	38.0	
100	37.4 ± 1.1	36.9	43

Table 5.3. A comparison of this work to previous values for MACS with kT energies ranging from 5 keV to 100 keV for ^{76}Ge.

^{76}Ge MACS Comparison			
kT (keV)	This Work $\langle\sigma\nu\rangle$ (mb)	NNDC[21] $\langle\sigma\nu\rangle$ (mb)	KADoNiS[29] $\langle\sigma\nu\rangle$ (mb)
5	70.0 ± 56.6	32.6	58
10	40.7 ± 15	19.2	39.8
20	25.2 ± 4.0	17.3	26.7
30	20.3 ± 1.9	16.9	21.5 ± 1.8
40	17.8 ± 1.1	16.1	18.2
50	16.2 ± 0.8	15.2	16.3
60	15.1 ± 0.6	14.4	15
70	14.2 ± 0.5	13.6	
80	13.5 ± 0.5	13.0	13
90	12.9 ± 0.4	12.4	
100	12.4 ± 0.4	11.8	12.3

^{76}Ge has the same story as ^{74}Ge where the MACS reported by KADoNiS was measured at $kT = 30$ keV using the activation method and then values were extrapolated across the thermal energy range. ^{70}Ge is the only germanium isotopes where time-of-flight data exists. Walter and Beer measured the neutron capture cross section using the time-of-flight technique in the neutron energy range of 3.5 to 240 keV in 1985[31]. We have expanded that energy range massively down to 10 eV and up to 1 MeV. Additionally, our measurement lowers the uncertainty on the MACS by roughly a factor of 2.

Chapter 6. Germanium Cross Section Conclusions

The stellar reaction rate for each weak s-process isotope heavily affects the abundance of isotopes produced downstream. Accurate measures of neutron capture cross sections are essential to calculating these reaction rates and thus predicting the abundances of intermediate mass elements ($60 \leq A \leq 90$). The first part of this thesis details the measurement of neutron capture cross sections for the stable even germanium isotopes so that accurate reaction rates can be calculated for these weak s-process isotopes.

Each weak s-process isotope acts as a bottleneck for isotope production downstream. The stable isotopes of germanium participate in the weak s-process and are thus important for determining weak s-process abundances. There are 5 stable germanium isotopes, ^{70,72,73,74,76}Ge. Prior to this work, experimental neutron capture cross section data was available for only ^{70}Ge and only in the neutron energy region of 3.5 to 240 keV. Additionally, experimentally determined Maxwellian-averaged cross sections were only available for ^{74}Ge and ^{76}Ge and only for the thermal energy of $kT = 30$ keV. The results of this work are neutron capture cross sections ranging from 10 eV up to 1 MeV for ^{70,72,74,76}Ge. Using these neutron capture cross sections, MACS were also calculated for thermal energies ranging between $kT = 20$ keV and 100 keV.

6.1. ^{70}Ge Conclusions

First, we examine the previous results from the two nuclear databases (NNDC and KADoNiS). Figure 6.1 shows a comparison of the MACS values from NNDC, KADoNiS, and the values found in this work. First we see that the values in the two databases agree quite closely. Both MACS are calculated from evaluations are based on an experimental measurement of the ^{70}Ge neutron-capture cross section in 1985 by Walter and Beer[31]. They used a time-of-flight method and measured the cross section between 3.5 and 240 keV.

If we examine the evaluated cross section from NNDC we can see the cause of the discrepancy in MACS between the databases and this work. Figure 6.2 shows a comparison

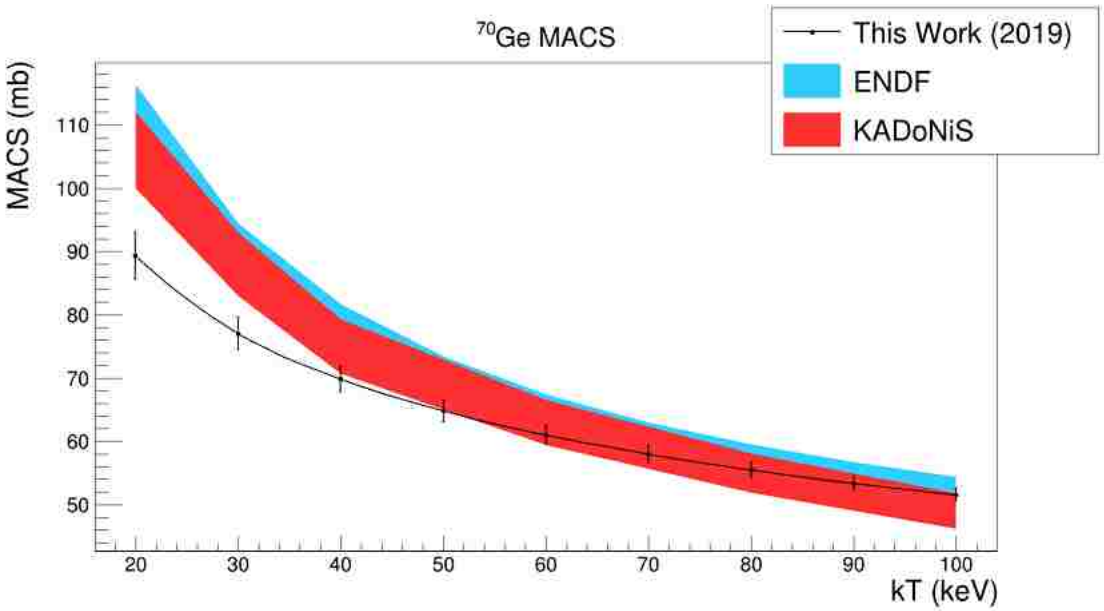

Figure 6.1. A comparison of the MACS of ^{70}Ge in this work to the evaluated values in the ENDF and KADoNiS databases.

of the measured cross section from this work to the evaluated cross section in the ENDF database. In the region between 3 keV and 14 keV, we see the evaluated cross section has an enhancement off-resonance. As Figure 6.3 shows, this structure is completely absent in the direct measurement made by Walter and Beer. Likewise, the feature is absent from our measurement. This off-resonance enhancement leads to an overvaluation of the MACS in the two databases compared to our direct measurement.

In order to make an apples-to-apples comparison, we broadened the neutron energy resolution of the evaluated cross section to match the energy resolution of our experiment using the R-Matrix code SAMMY[27]. SAMMY takes the resonance parameters from the evaluated cross section which contain all of the physics information in order to adjust the neutron energy resolution. As a product of using resonance parameters to perform the R-Matrix calculations, the off-resonance enhancement is removed. This implies that the off-resonance enhancement in the region of 3 to 14 keV is not based on the resonance parameters and thus not physical. When we compare the cross section measured in this work to this SAMMY-broadened evaluated cross section from ENDF (shown in Figure 6.4), we see much greater

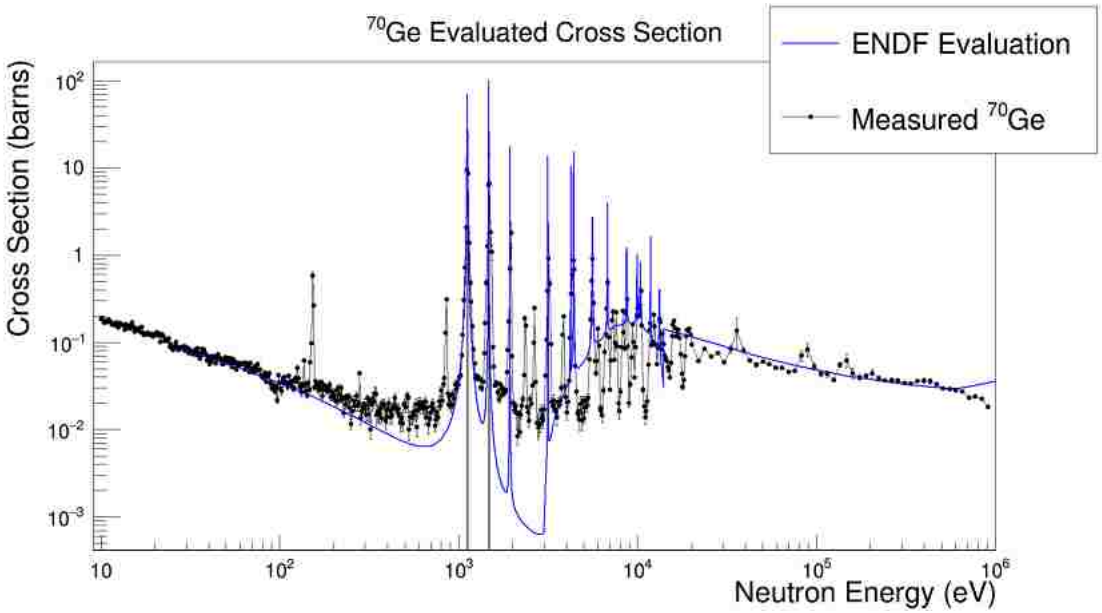

Figure 6.2. A comparison of the neutron-capture cross section measured in this work to the evaluated cross section in the ENDF database.

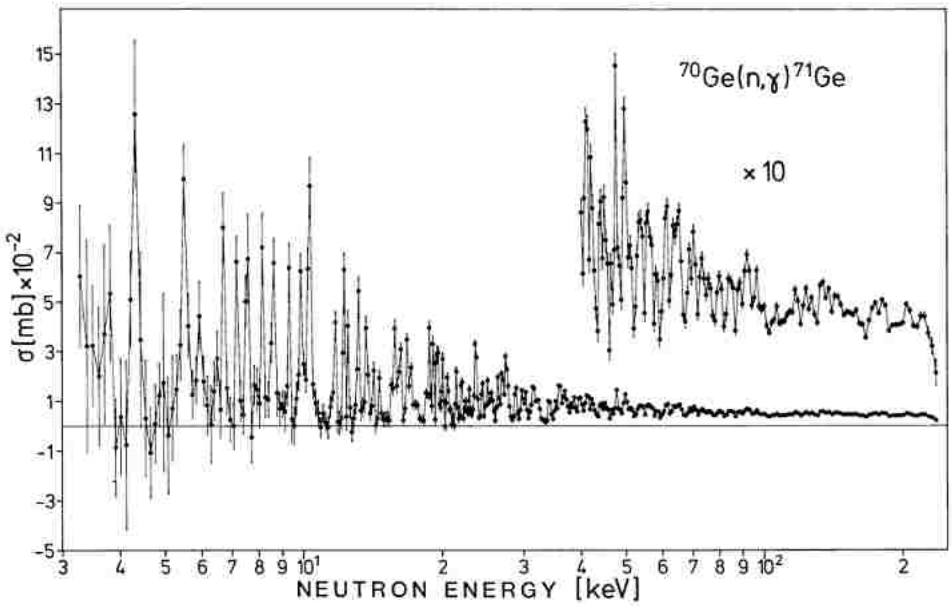

Figure 6.3. The neutron-capture cross section of ^{70}Ge as measured by Walter and Beer (1985)[31]

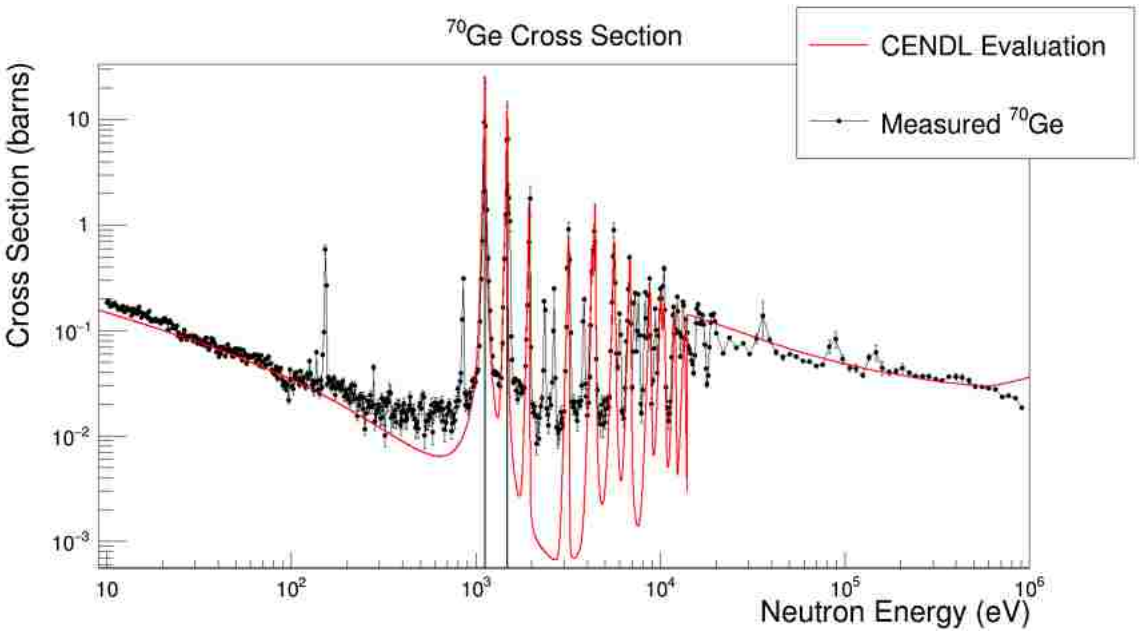

Figure 6.4. ^{70}Ge cross section. This work in black and resolution-broadened evaluated cross section in red (neutron energy resolution broadened using SAMMY R-Matrix code[27]).

agreement than with the unaltered ENDF evaluation. Additionally, when MACS values are calculated using the SAMMY-broadened evaluated cross section we find great agreement further suggesting that this off-resonance enhancement is non-physical. A comparison of the MACS values from this work to those from the databases including the SAMMY-broadened evaluation is shown in Figure 6.5.

6.2. ^{72}Ge Conclusions

The most notable result of these experiments is that of ^{72}Ge. Prior to this work no experimental data was available for this isotope. In some sense this makes ^{72}Ge the most significant measurement performed in these experiments. For a graphical comparison of ^{72}Ge values with this work, see Figure 6.6. When we look at this work compared to the theoretical values contained in the ENDF and the KADoNiS databases, we see that the ENDF values are heavily favored by this work. The thermal energy dependence appears to be quite similar for this work compared to the values in both databases.

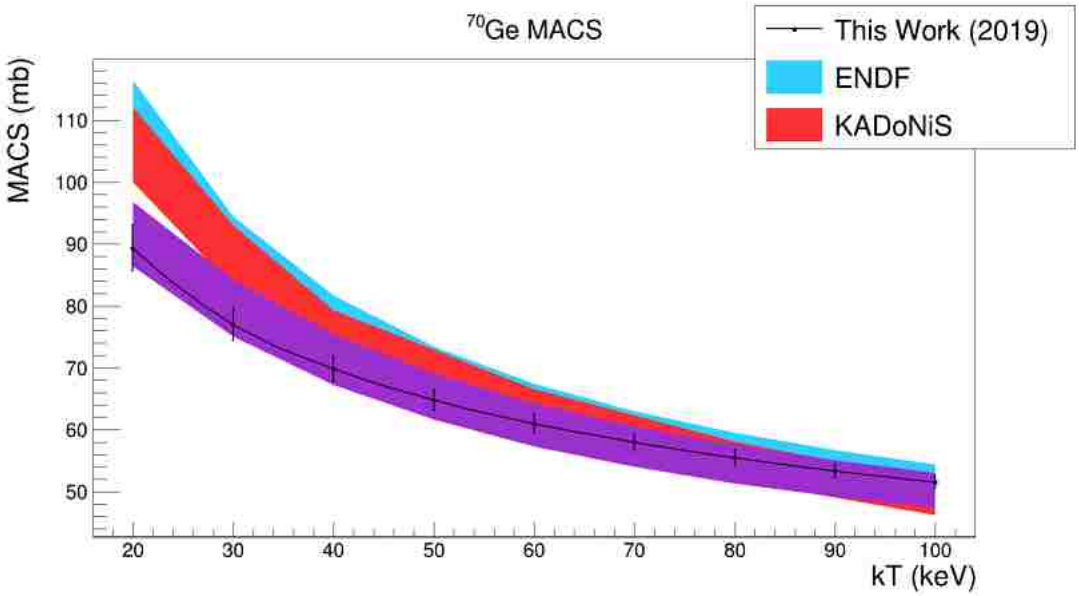

Figure 6.5. A comparison of the MACS of ^{70}Ge in this work to the evaluated values in the ENDF and KADoNiS databases including the values calculated from the SAMMY-broadened ENDF evaluated cross section.

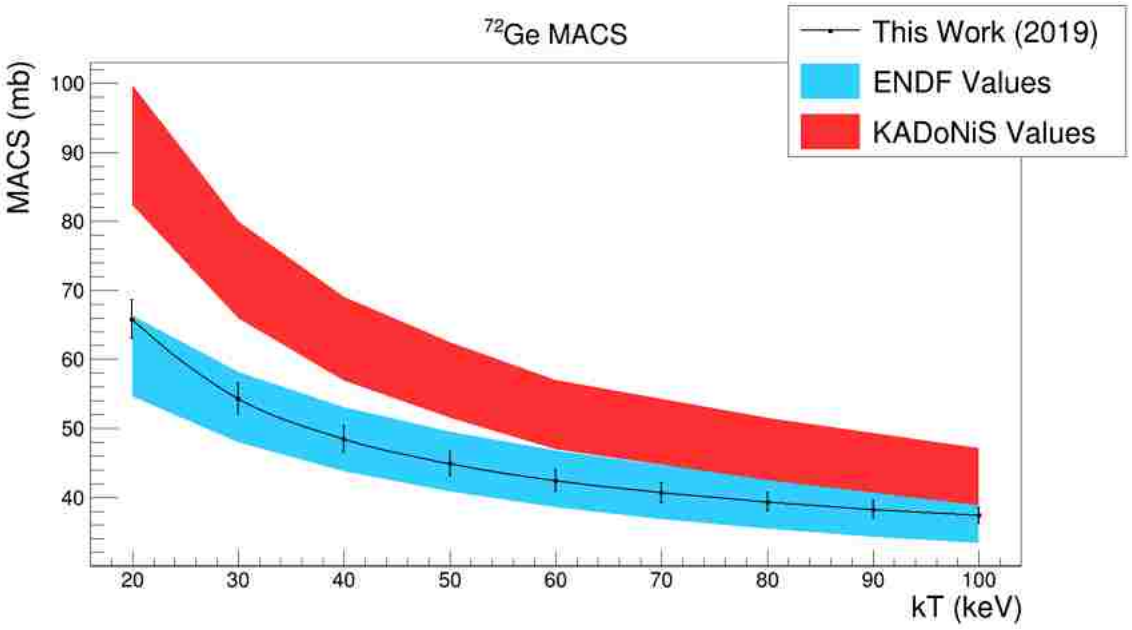

Figure 6.6. A comparison of the MACS of ^{72}Ge in this work to the theoretical values in the NNDC and the KADoNiS databases.

6.3. ^{74}Ge and ^{76}Ge Conclusions

The MACS of ^{74}Ge and ^{76}Ge have been directly measured at $kT = 30$ keV by Marganiec *et al* in 2009. The measurements were performed directly by using an activation technique as opposed to calculated from a direct measurement of the neutron-capture cross section. Marganiec *et al* exposed samples of ^{Nat}Ge to a neutron source using the ^{7}Li(p,n)^{7}Be reaction. This method simulates a thermal energy distribution for $kT = 25$ keV. Because the products of these neutron captures (^{75}Ge and ^{77}Ge) are unstable, the MACS can be determined by counting the activity of the samples after exposure to the neutron source. They then use theoretical models and cross section evaluations to infer the MACS at other thermal energies. These values are stored in the KADoNiS database. The values from the NNDC database are from ENDF evaluated cross sections.

First we compare our results for ^{74}Ge to those in the two databases. Figure 6.7 shows the MACS from this work plotted with the values in the databases. We find great agreement with the KADoNiS values at $kT = 30$ keV where the MACS was directly measured by Marganiec *et al*, however, the dependence on thermal energy is different. A similar trend is seen with the ENDF values and their thermal energy dependence. These discrepancies can be explained by examining the neutron-capture cross section measured in this work. Figure 6.8 shows a comparison of our neutron-capture cross section measurement with the ENDF evaluated cross section. A glaring discrepancy between the evaluation and the measured cross section is the transition point from the resonance region to the unresolved region. The evaluation begins the unresolved region around 5 keV whereas the measured cross section clearly shows defined resonances all the way up to approximately 15 keV. This results in an overestimation of the MACS at lower thermal energies where more emphasis is placed on this region. On the other hand, at high neutron energies we see an enhancement in the measured cross section when compared to the evaluation. This results in the opposite of what we see at low thermal energies. This behavior is clearly reflected in the MACS shown in Figure 6.7.

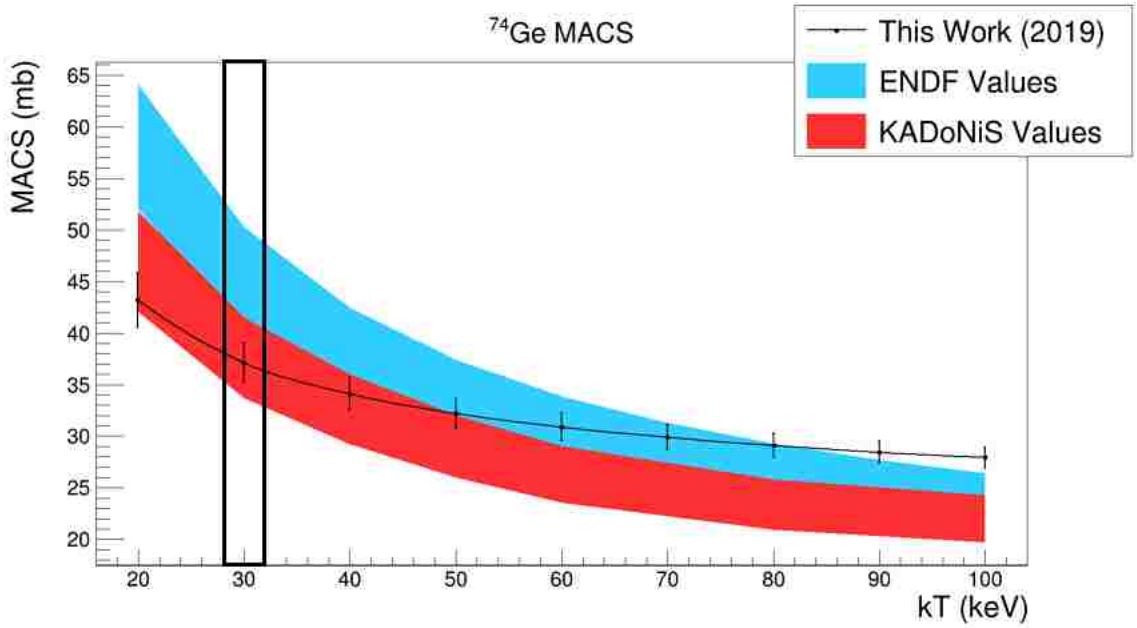

Figure 6.7. A comparison of the MACS of ^{74}Ge in this work to the theoretical values in the NNDC and the KADoNiS databases. The kT value for which the MACS was measured directly via activation technique is highlighted with a black box. This value is only in the KADoNiS database.

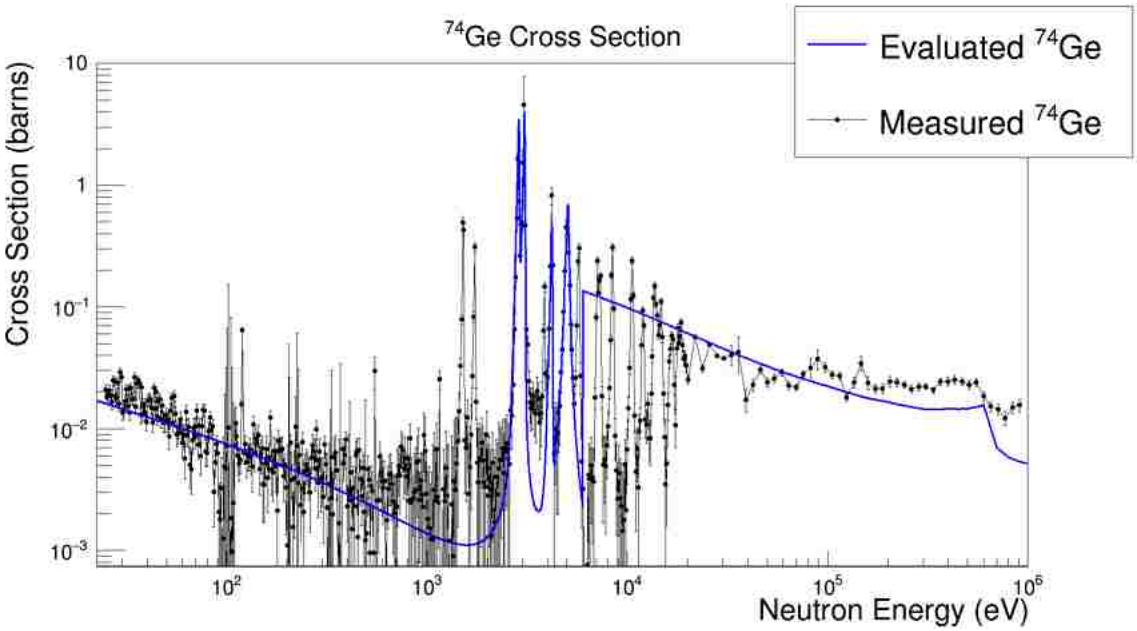

Figure 6.8. A comparison of the neutron-capture cross section measured in this work with the evaluated cross section in the ENDF database.

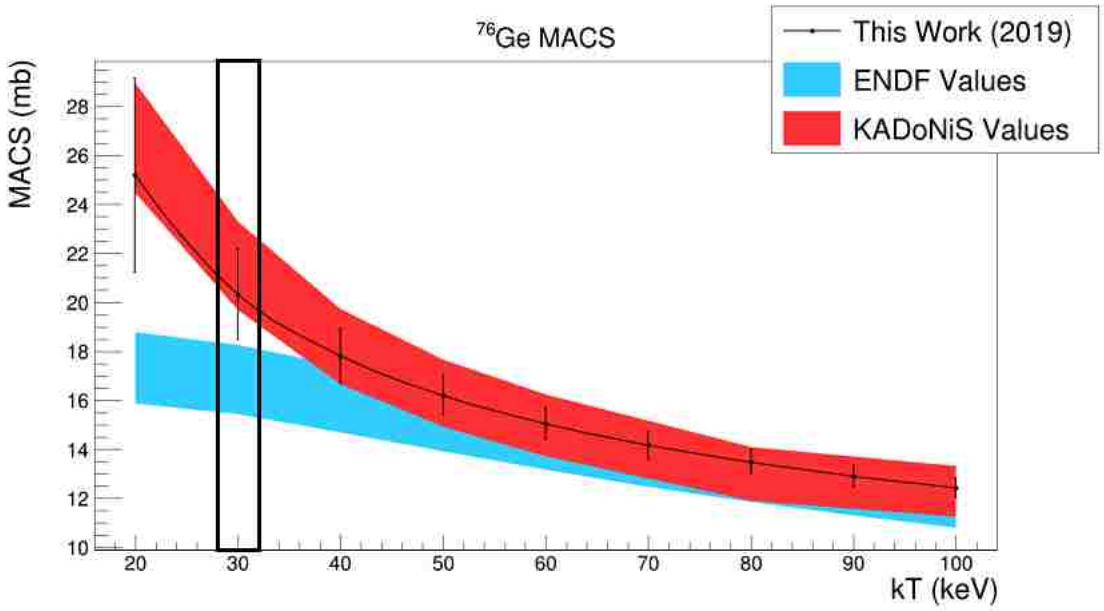

Figure 6.9. A comparison of the MACS of ^{76}Ge in this work to the evaluated values in the NNDC and the KADoNiS databases. The kT value for which the MACS was measured directly via activation technique is highlighted with a black box. This value is only in the KADoNiS database.

The MACS at $kT = 30$ keV for ^{76}Ge was measured the same way as ^{74}Ge. These values are stored in the KADoNiS database. Just as before, the values from the NNDC database are calculated from an evaluated cross section from ENDF. Figure 6.9 shows a comparison of the MACS measured in this work and the values in the two databases. Our measurement heavily favors the KADoNiS values. To explain the discrepancy, we once again compare our measured neutron-capture cross section with the evaluated cross section in the ENDF database. This comparison is shown in Figure 6.10. We can see that there are a number of large resonances between 8 keV and 30 keV present in the measured cross section that are absent in the evaluated cross section. These missing resonances make significant contributions to the MACS especially at lower kT values. This leads to the discrepancy we find between the ENDF MACS values and the measured values at lower thermal energies.

6.4. ^{73}Ge Discussion

In this work we have measured the neutron-capture cross section of the even stable germanium isotopes. Notably absent has been the stable isotope of ^{73}Ge. Recall that the

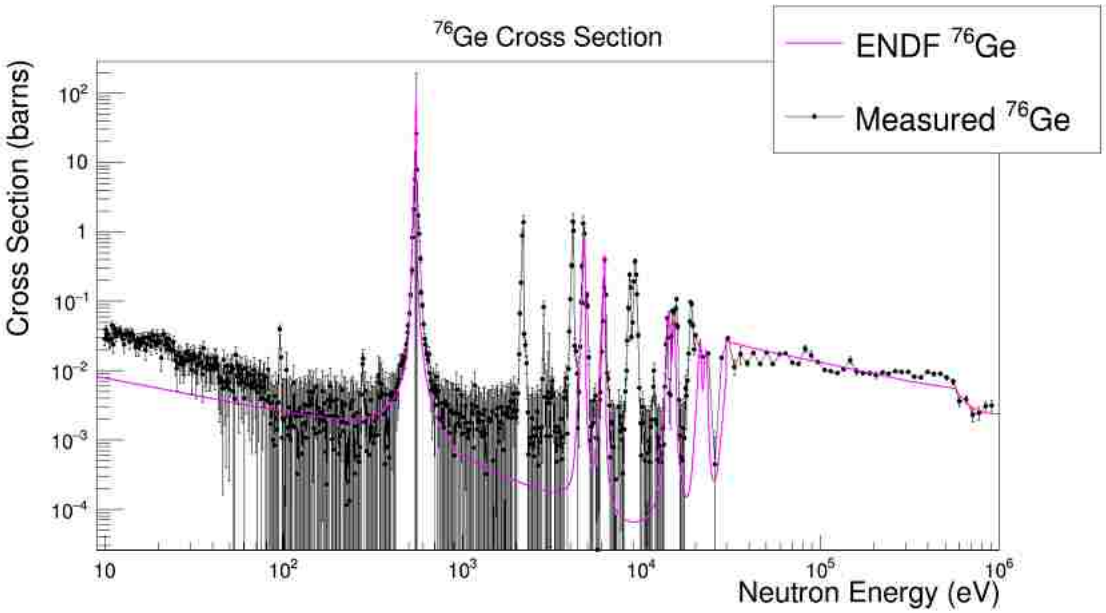

Figure 6.10. A comparison of the measured cross section from this work to the evaluated cross section in the ENDF database.

background subtraction process outlined in this thesis requires that the background reactions have Q values greater than the reaction of interest. The neutron-capture Q value of ^{73}Ge is greater than all the other reactions in this experiment so this process is not applicable. Rather than attempt to make a measurement, we present some preliminary analysis and discussion for this isotope.

Since the capture Q value for ^{73}Ge (10.2 MeV) rises above all background Q values, we can gate only on that part of the signal that lies above all backgrounds. This will allow us to view a qualitative approximation of the capture yield which we can arbitrarily scale to match the evaluated cross section in the ENDF database. While not a strict measurement, we can make some judgements about the validity of the evaluated cross section from our two databases. Figure 6.12 shows a comparison of the evaluated cross section from ENDF with values from this work arbitrarily scaled to match. While this is not a measurement, we can use this comparison to identify any potentially important flaws in the evaluated cross section. We find generally good agreement with the evaluated cross section. Additionally, we can compare the MACS values from this arbitrarily scaled cross section to those from the

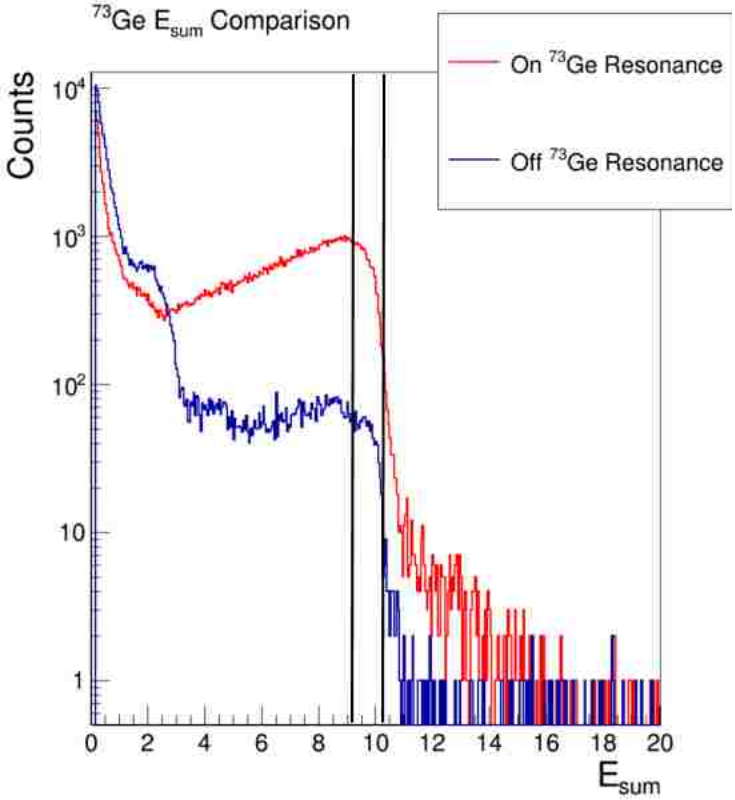

Figure 6.11. E_{sum} spectra on and off resonance from ^{73}Ge. Two vertical lines are laid over the top to indicate the E_{sum} cutoff energy such that the yield is free of background.

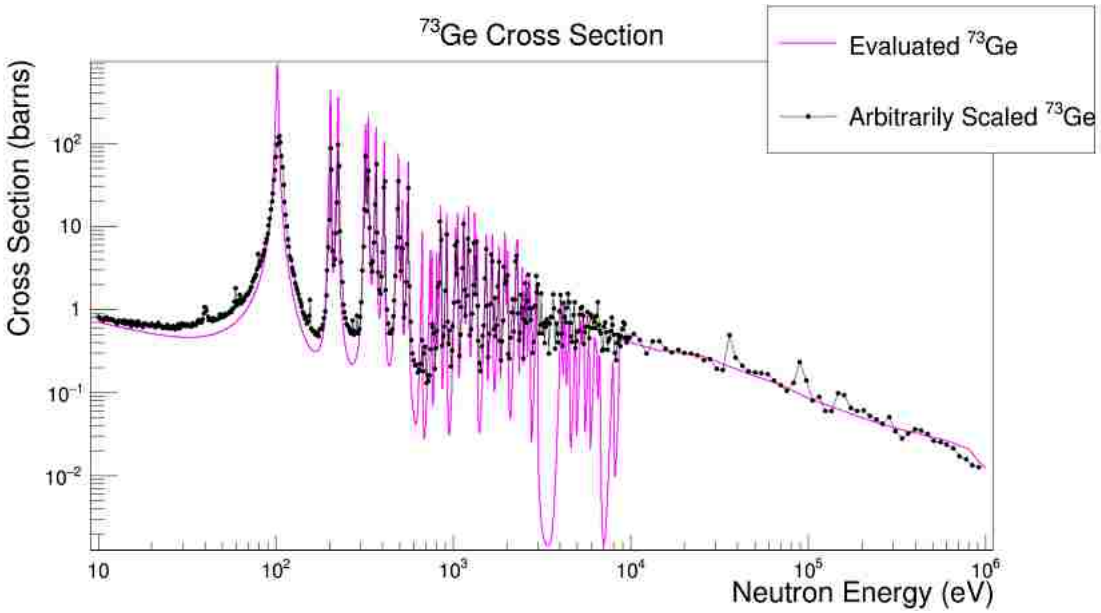

Figure 6.12. A comparison of the evaluated cross section of ^{73}Ge from ENDF with values from this work arbitrarily scaled to match.

NNDC and KADoNiS databases. This comparison is shown in Figure 6.13. These values do not constitute a rigorous measurement but this simple analysis should serve to bolster the confidence of astrophysicists using the KADoNiS MACS values in their nucleosynthesis calculations.

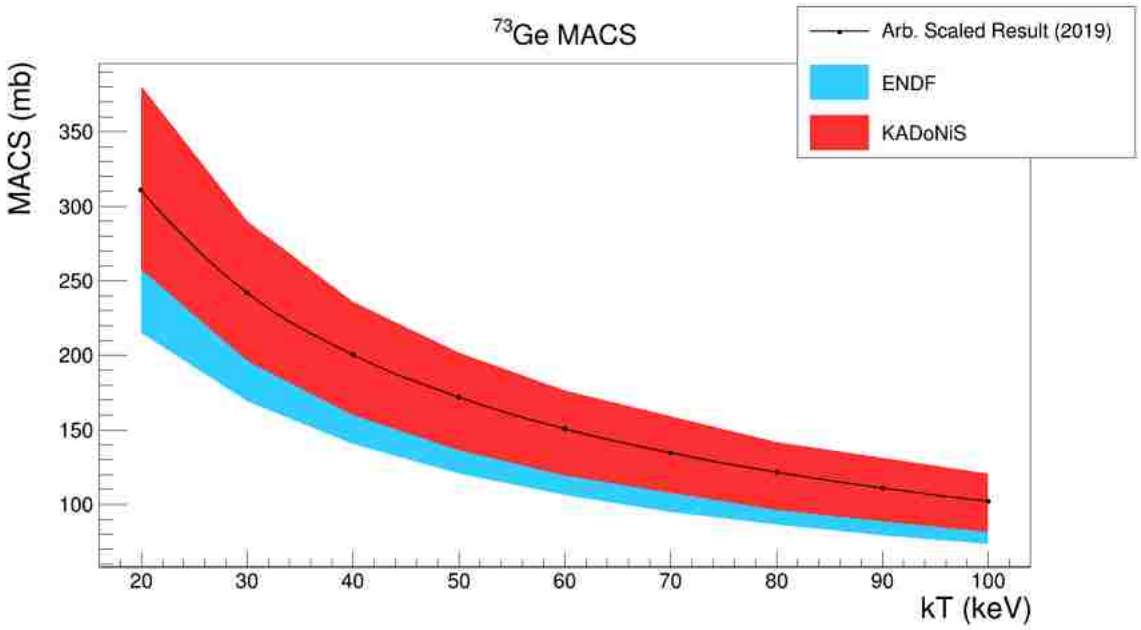

Figure 6.13. A comparison of the MACS of ^{73}Ge from the arbitrarily scaled values in this work to the evaluated values in the NNDC and the KADoNiS databases.

Chapter 7. β-Delayed Neutron Emission

7.1. Background and Motivation

β-delayed neutron emission is a process wherein a radioactive isotope undergoes β-decay immediately followed by emission of a neutron. This is energetically allowed when the parent nucleus β-decays to an excited state of the daughter that lies above the neutron separation energy of the daughter [32]. A schematic diagram including example level schemes of this process is shown in Figure 7.1. This method of decay has important implications for a number of fields including the functioning of nuclear reactors, non-proliferation of nuclear weapons, and the structure of atomic nuclei. Additionally, β-delayed neutron emission can provide insight into the structure of atomic nuclei since it is a phenomenon that occurs only in neutron-rich isotopes. Finally, the impact that β-delayed neutron emission has on the synthesis of heavy elements is of particular interest.

When a nucleus undergoes fission, it splits into fission fragments, a few neutrons, and releases energy in the form of gamma rays. If ^{235}U captures a neutron and becomes ^{236}U, it can undergo nuclear fission and release more neutrons. Nuclear reactors exploit a chain reaction of these nuclear fissions in order to produce heat. Since the reactor relies on a steady supply of neutrons to be captured by the nuclear fuel, knowing both the magnitude and the time dependence of the neutron flux present in the reactor is of critical importance [33]. In addition to the prompt neutrons produced by the fission itself, the fission fragments are neutron-rich nuclei some of which can undergo β-delayed neutron emission. As such, researchers must account for their contribution to the overall neutron flux since the neutron flux affects how a reactor operates.

β-delayed neutron emission also provides for a technique in detecting the presence of fissile materials. A non-invasive method has been proposed by Slaughter et al. to detect nuclear weapons in cargo shipments [34]. Playfully deemed "the nuclear car wash", this technique involves pulsing a beam of neutrons into the cargo shipments, which will induce nuclear fission

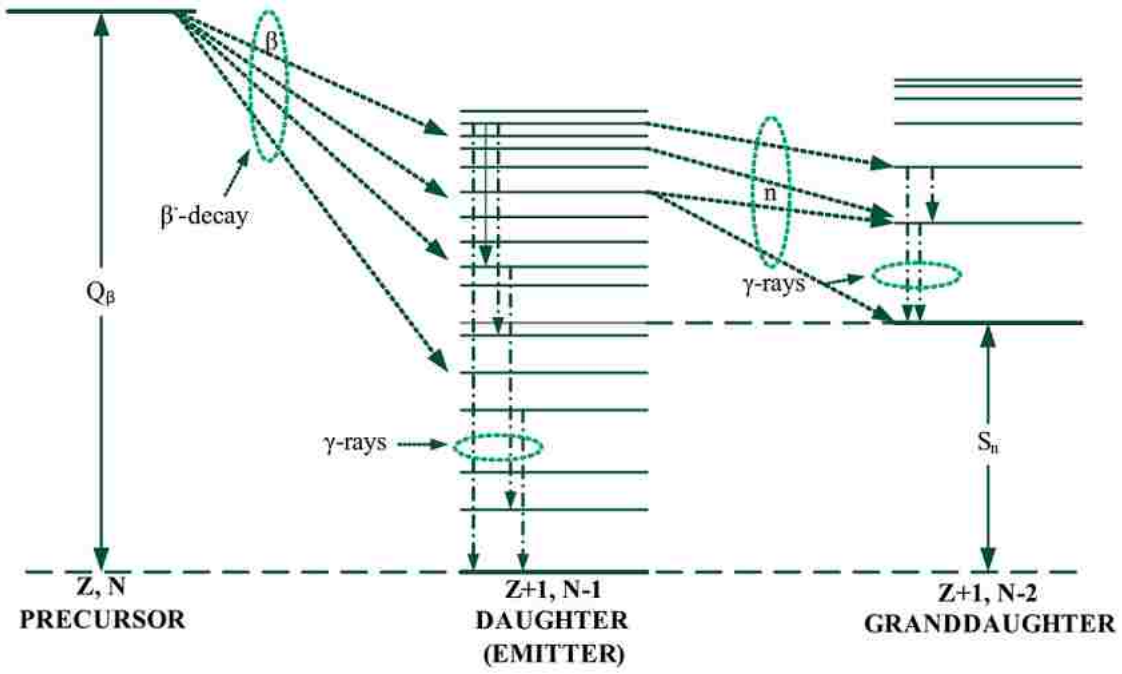

Figure 7.1. A schematic depicting the process of β-delayed neutron emission[32].

events in any nuclear weapons materials. The fission fragments will in turn emit β-delayed neutrons and gamma rays that can be detected and identified using conventional radiation detector systems. This technique presents a few advantages. First, it can be performed with minimal invasion since both the pulsed neutrons and the resulting β-delayed neutrons and gamma rays easily penetrate barriers. Second, the β-delayed neutrons and the gamma rays produce a signature that is unlike any typical backgrounds created by activation from the pulsed neutrons. In order to use this technique, however, both the β-delayed gamma-ray and neutron properties of fission fragments need to be known.

The astrophysical r-process, as opposed to the s-process, is characterized by rapid neutron captures. These neutron captures occur on a timescale shorter than β-decay occurs and thus the r-process can synthesize very neutron-rich isotopes. Towards the end of the r-process is a freeze out phase where neutron density drops and rapid neutron capture ceases. During the freeze out phase, the neutron-rich nuclei decay back to stability and produce the isotopic abundances we observe in the Universe. The observed isotopic abundances from the r-process are shown in Figure 7.2. The site(s) of the astrophysical r-process is currently unknown,

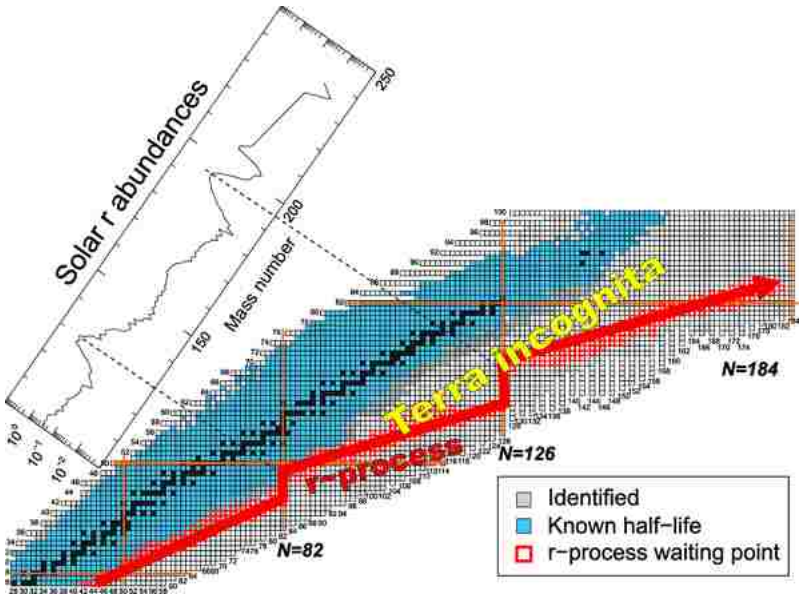

Figure 7.2. Observed isotopic abundance pattern created by the r-process along with a depiction of the r-process path overlaid on the chart of the nuclides [37].

however, the most likely candidates include core-collapse supernovae [35] and neutron star mergers [36].

The role of β-delayed neutron emission in the r-process occurs primarily during the freeze out phase. Without β-delayed neutron emission, the abundance peaks will be heavily centered around stable isotopes produced by the β-decay chains originating from closed neutron shell nuclei. This is because nuclei with closed neutron shells have much smaller neutron-capture cross sections. As a result, waiting points appear in the r-process around closed neutron shells where a relatively high density of isotopes are accumulated [38]. Without β-delayed neutron emission, these waiting point nuclei would simply undergo a series of β-decays until they reach stability. Therefore, the abundance pattern around the waiting points would be preserved. Figure 7.3 shows a comparison of the width of s- and r-process peaks. The neutron rich, pre-freeze out r-process abundances exhibit imbalances due to the binding energy differences of even-even, odd-odd, and odd-even nuclei [39]. These pairing effects lead to a jagged distribution in the s-process and in the pre-freeze out r-process abundances. The effect of β-delayed neutron emission causes a smoothing out of these abundance

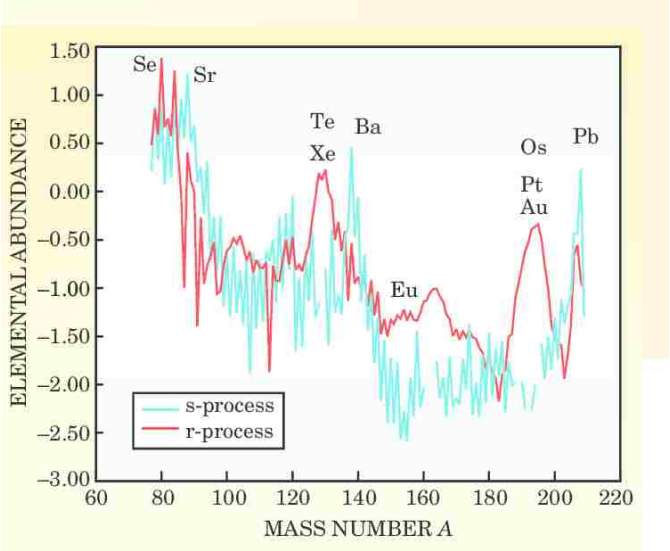

Figure 7.3. Observed solar abundances of the heavy elements. The r-process is shown in red and the s-process is shown in blue [41]. Note the width of the peaks in the r-process and the s-process. This broadening effect is due to β-delayed neutron emission.

peaks as the hypothetical, straight β-decay chain is broken a portion of the time [40]. A comparison of the actual r-process abundances to hypothetical abundances in the absence of β-delayed neutron emission is shown in Figure 7.4. In order to accurately predict the r-process abundances we observe in the Universe, we must be able to account for β-delayed neutron emission. An important step toward accounting for β-delayed neutron emission is measuring the branching ratios of r-process isotopes.

In conventional experiments, the neutron energy spectrum and the β-delayed neutron emission branching ratio (the probability of emitting a neutron immediately following a β-decay) are measured independently using different experimental setups. For example, Beta-delayed neutron measurements at RIKEN (BRIKEN) is designed to measure the β-delayed neutron emission branching ratio [43]. In these types of experiments, radioactive nuclei are implanted on a tape, they decay, and any neutrons emitted are moderated by a plastic moderator and detected by ^3He tubes. These experiments have high efficiency for detecting neutrons but the moderation process removes all information about the neutron energy spectrum. On the other hand, experimental setups like the Versatile Array of Neutron

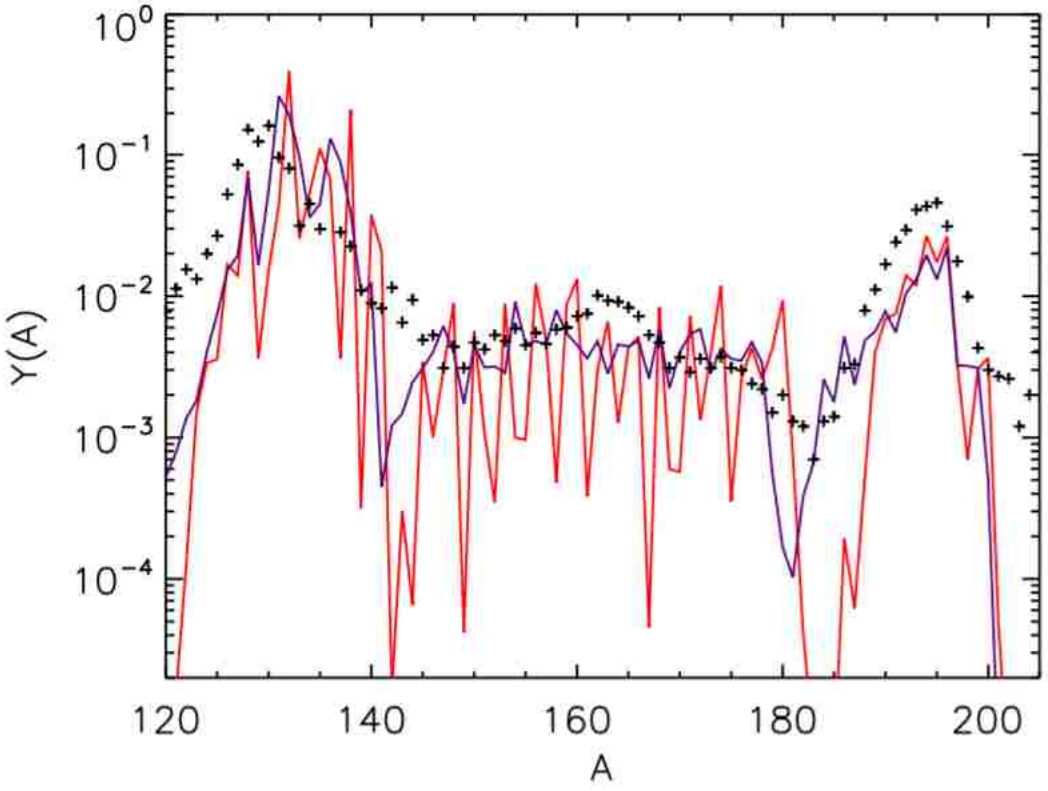

Figure 7.4. A comparison of predicted r-process abundances with β-delayed neutron emission (blue), without (red), and the observed abundances (black points) [42].

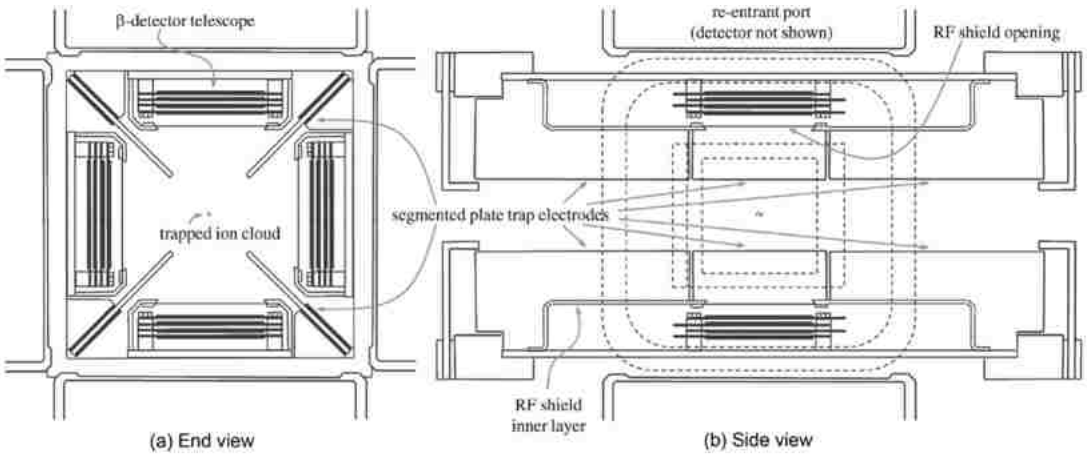

Figure 7.5. (a) an end view of a linear Paul trap with 4 plane electrodes. (b) side view of an example linear Paul trap with electrode segments pointed labeled[48]

Detectors at Low Energy (VANDLE) have been designed to measure both the neutron energy spectrum and the branching ratio simultaneously through neutron time-of-fight spectroscopy [44]. Just like with BRIKEN, this experimental setup relies on direct neutron detection to perform a measurement.

7.2. Ion Traps

Ions can be trapped using a combination of electric and magnetic fields. One such variety of ion trap is the Paul trap [45]. Also called a quadrupole ion trap, this device consists of two hyperbolic electrodes that function as end caps and a ring electrode whose center is the trapping location of the ion cloud [46]. This configuration works by alternating the voltages on the hyperbolic end cap electrodes so that the ion cloud oscillates between being pulled towards the electrodes (elongated) and being pushed away from the electrodes (flattened like a disk). A variation of this design, called the linear Paul trap, replaces the previously described trapping electrodes with four axially-segmented plate or rod electrodes placed at the corners of a square. Generally, the electrodes are segmented in three sections with the outer sections replacing the statically charged ring electrode and the middle sections being used to generate the oscillating quadrupole fields that were generated previously by the hyperbolic end caps [47]. A diagram of this segmentation is shown in Figure 7.5.

Linear Paul traps are particularly useful for studying radioactive decay because there are gaps between the trapping electrodes in which various detectors can be stationed. These detectors can be used to measure decay radiation from trapped radioactive ions. One such ion trap is the Beta-decay Paul Trap (BPT) at Argonne National Laboratory (ANL). This is a version of a Paul trap designed specifically for high precision β-decay studies [48].

7.3. Recoil-Ion Time-of-Flight Technique

A novel technique for measuring both the neutron energy spectrum as well as the branching ratio of β-delayed neutron emission was pioneered by physicists at Argonne National Laboratory and Lawrence Livermore National Laboratory that only employs detection of the recoiling ion and beta. This bypasses the difficulty of direct neutron detection faced by other experimental setups with similar goals. Assuming the trapped ion decays at rest, the velocity of the recoiling ion is given by Equation 7.1.

$$v_r = -\frac{1}{m_r} \sum i m_i v_i \tag{7.1}$$

This comes simply from conservation of momentum. v_r and m_r denote the velocity and mass of the recoil ion and the variables denoted by v_i and m_i are the velocity and mass of the emitted particles (beta, gamma-rays, neutrino, conversion electrons, etc.), respectively. In principle, if a neutron is emitted then we must account for both the momenta of the leptons and the neutron. However, since the mass of the neutron is so much greater than the mass of the leptons we can neglect their electron's contribution to the recoiling ion's momentum. We can see that a trapped ion that undergoes β-delayed neutron emission will recoil with a greater energy than one that undergoes simple β-decay since the neutron is $\sim$2000 times heavier than the electron, which will allow their discrimination via time-of-flight spectroscopy.

Two types of detectors are employed to perform these measurements. The first is an organic plastic scintillator set up to be a ΔE-E telescope configuration. This is a common

detector configuration used in nuclear physics consisting of a detector that allows only a small amount of energy to be deposited (ΔE) and one positioned directly behind it in which the remaining energy is deposited (E). This allows for particle identification as different types of particles deposit different proportions of their original energy into the ΔE detector. The other type of detector used to perform this recoil ion time-of-flight method is called a Microchannel Plate (MCP) detector. MCPs are made of a highly resistive material with an array of microscopic holes that go from one face straight to the other. When a particle passes through an electrically biased MCP, a cloud of electrons are produced that are used to generate a signal. In the recoil ion time-of-flight technique, we detect and identify β-particles detected in the ΔE-E telescopes and recoil ions detected in the MCP detectors. Since the β particle travels so much faster than the recoiling ion, its detection can be used as an initial time for the decay. The following detection of the recoiling ion gives an end time so we can determine the time of flight. Since the recoil ion travels faster after a β-delayed neutron emission than a simple β-decay, we expect to observe two distinct peaks in the time-of-flight spectrum if a nuclide undergoes β-delayed neutron emission part of the time. An example time-of-flight spectrum is shown in Figure 7.6. Using this method, we can reconstruct the neutron energy spectrum using the time of flight and conservation of momentum. Additionally, the branching ratio can be extracted by comparing the number of counts in each time-of-flight peak. The number of counts in each peak corresponds to the number of decays observed of each type. Thus we can measure the branching ratio, or fraction of decays that a neutron is emitted in the decay of a trapped radioactive sample.

7.4. Previous Work

7.4. Proof-of-Principle Experiment

In 2011, an experiment was performed at ANL using the BPT to test the recoil ion time-of-flight method to measure the β-delayed neutron energy spectrum and branching ratio of ^{137}I [50]. A schematic of the BPT setup can be seen in Figure 7.7. ^{137}I was chosen since it is a β-delayed neutron emitter with a well-studied neutron energy spectrum and a precisely

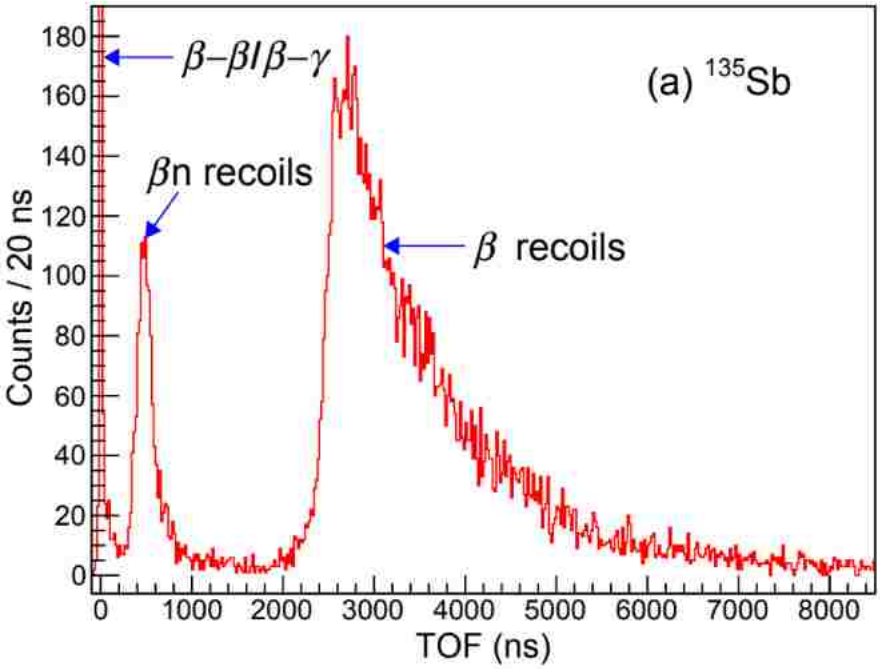

Figure 7.6. Recoil ion time-of-flight spectrum of ^{134}Te and ^{135}Te after β-delayed neutron emission and β-decay respectively of ^{135}Sb [49]. Figure adjusted from original to show only the spectrum for ^{135}Sb.

known branching ratio. Just as expected, two distinct peaks form corresponding to β-delayed neutron emission and β-decay. This experiment determined that the recoil ion time-of-flight technique was a valid approach by measuring the β-delayed neutron energy spectrum and branching ratio. The results of this proof-of-principle experiment are discussed in Chapter 9.

7.4. First Campaign

The first research campaign using this technique started in 2013 to examine some proposed improvements to the experimental setup and take advantage of increased beam intensity using the CAlifornium Rare Isotope Breeder Upgrade (CARIBU) at ANL. The alterations to the experimental setup primarily involved detector placement and number of detectors. These changes were made to increase the detection efficiency for beta and recoil ion events. The number of ΔE-E telescopes and MCPs was increased from one each to two each. They were set up on all four sides of the trap such that across from each MCP was a

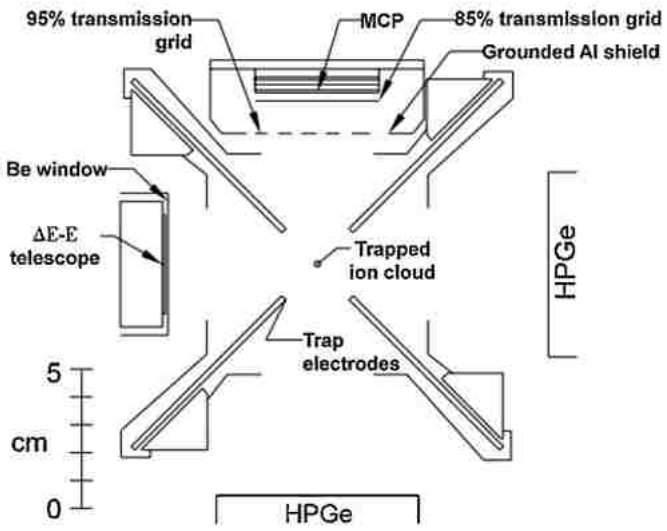

Figure 7.7. Cross sectional view of the BPT including electrodes and detectors used in the proof of principle experiment of the recoil ion time-of-flight technique[48].

ΔE-E telescope. This increases the solid angle of the detectors roughly by a factor of two. A schematic of the new experimental setup can be seen in Figure 7.8. For this experiment, ^{134}Sb was used because it does not undergo β-delayed neutron emission and was believed to have a simple β-decay scheme. This makes it a good candidate to assess the efficiency of this adjusted experimental setup. In addition to determining overall detection efficiency, this experiment developed a technique used to determine the charge state distribution of the recoiling ions [51].

The neutron energy spectra and branching ratios of seven β-delayed neutron emitters were also studied in this first campaign with the BPT. Czeszumska *et al* studied ^{137,138}I and ^{144,145}Cs [52] while Alan *et al* studied ^{135,136}Sb and ^{140}I [49]. The conclusions of these experiments are discussed in Chapter 8. With the development of these experimental techniques it was determined that future work would benefit from a dedicated ion trap and detector system being built for β-delayed neutron emission studies.

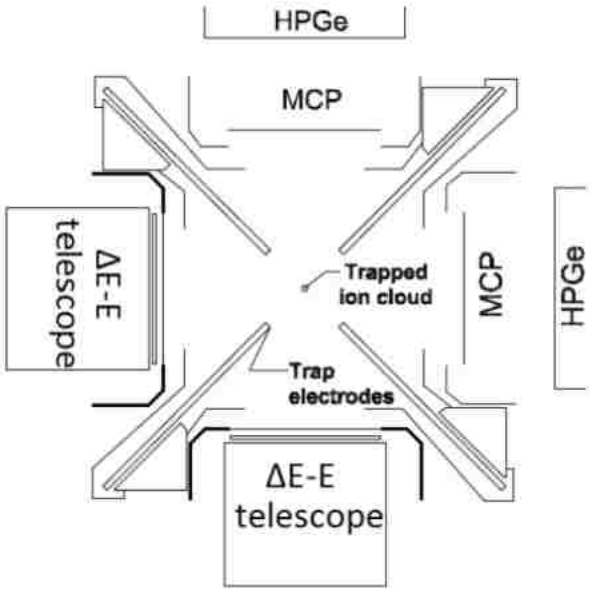

Figure 7.8. Cross sectional view of the BPT configuration for the 2013 experiment. Figure taken from Siegl *et al* [51].

Chapter 8. Next Generation Trap Design

The goal for the next generation ion trap for β-delayed neutron emission studies at ANL is a design that builds on the strengths of the BPT while minimizing its weaknesses. One such weakness of the BPT is that the plate electrodes provide large surfaces for β scattering, which must be accounted for in the analysis of any experiment performed using the BPT. This problem can be reduced by using rod electrodes instead of plate electrodes, which reduces the amount of material available for β scattering. An element of the trap design in need of optimization is the size of the detectors and their distance from the center of the trap. We investigated both of these using simulations to determine the optimal configuration.

8.1. Simulation Techniques

Our simulations of β-delayed neutron emission experiments use a suite of software in four parts: a β-decay event generator code adapted from [53], SIMION [54], Geant4 [55], and the analysis framework ROOT [56]. The decay code accepts a control file detailing parameters of the decay such as the isotope, β-ν angular correlation coefficient, and charge state; a file that details the level scheme of the daughter nucleus taken from the Reference Input Parameter Library (RIPL) nuclear database [57]; number of decays; size of the ion cloud being trapped; and a parameter to choose whether or not β-delayed neutron emission occurs. The program outputs three files: 1) a master file outlining the initial parameters for all decay events, 2) a SIMION input file, and 3) a Geant4 input file. The next steps can occur simultaneously. SIMION is a software package used for simulating ion trajectories in electric fields generated by static or radio-frequency electrodes. This software package is used to track the recoiling ion and in particular will be used to simulate the recoil ion trajectories between the trap center to the plane of the MCP detectors. The other leg of this simulation procedure is simulating the interaction of β particles, neutrons, conversion electrons, and γ rays with components of the ion trap and the detectors. This is handled by a Geant4 simulation that tracks these decay products and simulates their physical interaction with all trap components

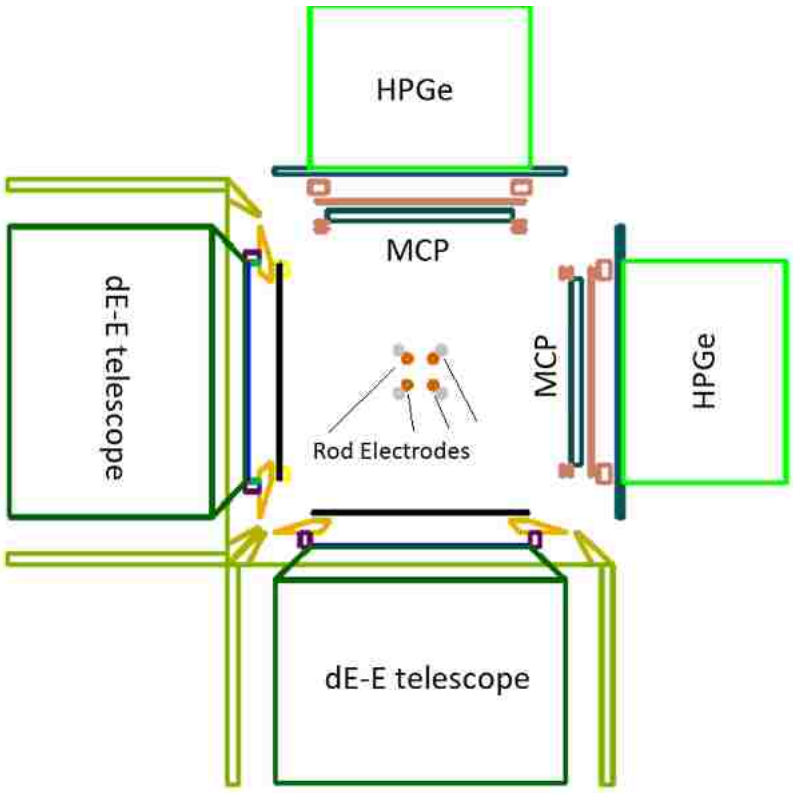

Figure 8.1. Cross-sectional diagram of the ion trap and detector system used in the Geant4 simulations for a next-generation device for β-delayed neutron studies.

and detectors. A cross sectional view of one such Geant4 simulation is shown in Figure 8.1. Once these independent simulations are complete, their outputs are combined together with the master file to form a ROOT file containing all of the data.

8.2. Simulated Data

A large amount of information is dumped out of these simulations. The master branch of the resulting ROOT tree contains information about the initial conditions of the βs, neutrons, and recoiling ions including velocity vectors, initial positions, and time of decay. The SIMION branch contains positions where ions make contact with anything in the trap, kinetic energy at contact, and time of contact. The Geant4 branch contains energy deposition information in the ΔE and E plastic detectors. From all of this simulated data, a few bits of important information about the response and overall efficiency of the detector system can be determined.

Of particular concern are various coincidences between β particles and recoil ions. These are broken into 180° and 90° categories based on which detectors are in coincidence. An important metric used in these simulations is the ratio of 180° to 90° coincidences. This value varies greatly between simple β-decays and β-delayed neutron emission. In simple β-decay, it is much more likely to detect a recoil ion in coincidence with a β at 180° than 90° because the direction of the recoil ion is dictated mostly by the momentum of the β particle. In β-delayed neutron emission, however, the likelihood of 180° and 90° coincidences is roughly equal. This is because the direction of the emitted neutron is largely uncorrelated with that of the β particle. Since the neutron emission dominates the recoil of the ion, there is little correlation between the β direction and the direction of the recoiling ion. Thus the 180° to 90° ratio is very close to 1 for cases of β-delayed neutron emission.

Another use for this important ratio is determining the charge state-distribution of the recoiling ions in the trap. This technique was developed by Siegl *et al* in the 2013 campaign with ^{134}Sb [51]. Ions with a higher charge state will feel a greater effect from the RF electrodes. Therefore, by examining the overall dependence of β-ion coincidences on RF-phase and assuming a geometrically decreasing charge state distribution, we can determine the charge state distribution of the ion cloud. An example of the results of this technique are shown in Figure 8.2. This technique requires β-decay only since ions recoiling after a neutron emission have enough energy to minimize the effects of the RF-phase. The 2013 campaign used ^{134}Sb as a calibration to determine the intrinsic MCP efficiency because it exclusively undergoes β-decay with no neutron emission and decays to the ground state of ^{134}Te approximately 98.6% of the time [58]. In future experiments, this technique can be used with isotopes that undergo β-delayed neutron emission by simply gating on longer times of flight associated with no neutron emission.

The β-neutrino correlation coefficient ($a_{b\nu}$) influences the observed 180° to 90° ratio. As a result, simulations can allow us to determine the average $a_{b\nu}$ of the observed decay. The range of valid $a_{b\nu}$ values is from 1 (perfectly correlated) to -1 (perfectly anti-correlated).

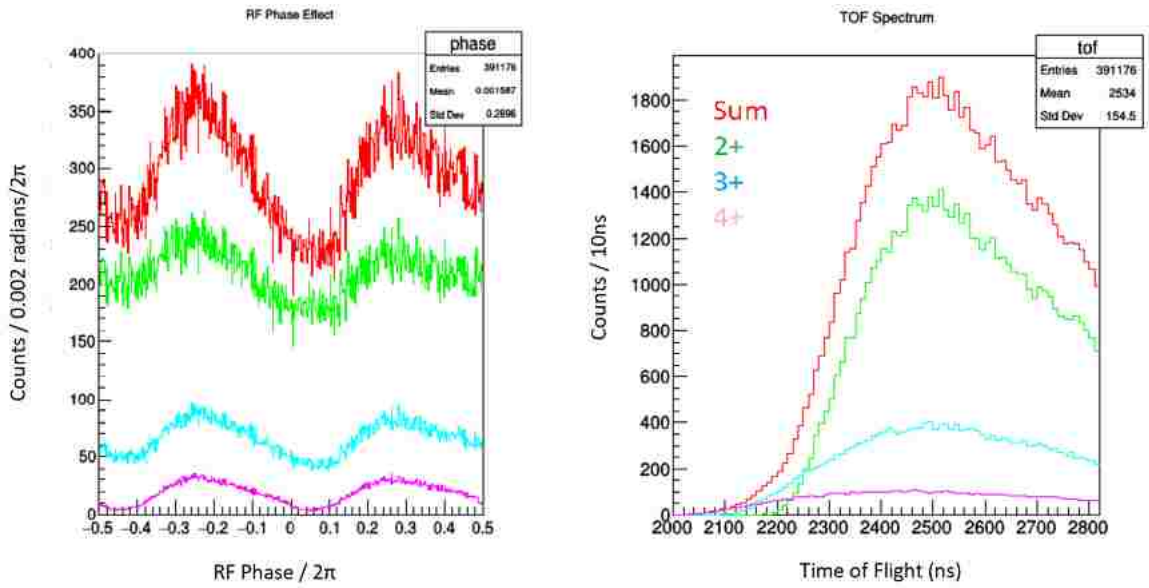

Figure 8.2. (Left) The effect of β-ion coincidence count rate vs RF-phase. (Right) The time-of-flight spectra acquired by the RF-phase fitting technique.

If these two extremes are simulated and the resulting 180° to 90° ratios are used to fit the data, then an average $a_{b\nu}$ can be determined. So the simulations can be used to determine charge state distribution and $a_{b\nu}$ using the 180° to 90° coincidence ratio. In addition to these important quantities, the ion cloud can also be determined using simulations. This is accomplished via a simple fit of the time of flight spectra, which is shown in Figure 8.3.

8.3. Next Generation Trap and Detector System

The techniques discussed above have established a simulation suite as a powerful tool for β-delayed neutron emission experiments using recoil ion time-of-flight spectroscopy. The utility of simulations for ion trapping is not limited to analysis, however. The primary motivation for my simulation work is to investigate the designing of a dedicated, next-generation ion trap and detector system for such experiments. The main objective for the new instrument will be to increase overall detection efficiency while improving precision of measurements made with the recoil-ion method. This is often a trade off we face in detector design. For instance, we can drastically increase detection efficiency by placing detectors extremely close to the center of the trap, however, the precision of measured times of flight

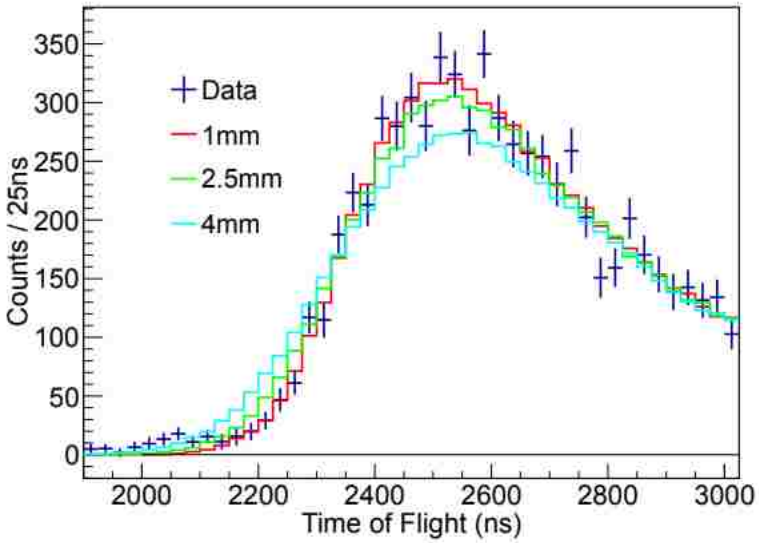

Figure 8.3. An example of fitting ion cloud size to time of flight data using simulations. Figure from Ref. [59]

would be far too low to discriminate between recoil ions from β-delayed neutron emission and β decay. We can eliminate this problem by placing detectors further away from the center of the trap, but in order to maintain the same level of solid angle coverage, the detectors would have to be made larger. There are physical as well as manufacturing limitations with how large a detector can be so a compromise between detector size and distance from the ion cloud must be made. Finally, a significant weak point observed in the previous experiments was the β detection threshold. Lowering of the β energy detection threshold is a key objective in the design of the new plastic ΔE-E telescope detectors.

8.3. MCP Design

When it comes to selecting a detector size, we have to consider MCP manufacturing limitations. At the time of this writing, the largest MCP that can be reliably produced by the manufacturer is approximately 100 x 80 mm^2. Since we have a limit on MCP size, we must simply choose a distance from the center of the trap that strikes a desired compromise between solid angle coverage and time of flight uncertainty. This distance for the next generation trap is chosen to be 65 mm. This is the furthest distance the MCP can be placed from the center of the trap while simultaneously covering the entire solid angle width that

the ion cloud can see between the rod electrodes. The ΔE-E telescopes actually have neither restriction since plastic scintillators have neither the manufacturing limitation nor the time of flight problem (βs are used as the time of flight trigger because they are the fastest decay product that can be reliably detected and is present after each decay). For simplicity, the distance for the ΔE-E telescope is chosen to be the same. This allows for the ion trap chamber to have a square radial cross section and the detectors to be centered on the sides as shown in Figure 8.1.

8.3. ΔE-E Telescope Design

Another consideration for the next generation ion trap is the design of the ΔE-E telescopes. A few aspects of the previous telescope design can be improved. The previous ΔE-E detector setup is a thin circular disk for a ΔE placed in front of a thick, cylindrical E detector. One design that was investigated is a similar setup that replaces circular ΔE and cylindrical E with square ΔE and rectangular prism E. This moderately increases solid angle and opens the possibility for other upgrades as well.

A common occurrence in these trapping experiments is a neutron detection in the ΔE-E telescope. Segmentation of the ΔE detector offers some worthwhile benefits in this field. With segmentation of the detector(s) some position sensitivity is gained. The benefit of position sensitive ΔE-E detectors is that neutron-recoil ion coincidences can be identified. Since the path of nuclei after neutron emission is essentially a straight line, a position sensitive ΔE-E telescope combined with the already position sensitive MCP allows us to determine whether the signals produced by the ΔE-E was due to scintillation light produced by a neutron or a β. We investigated the degree to which this position sensitivity allows us to screen for neutron detections. Finally, adjustments to the light guides were investigated in an attempt to increase the light collection efficiency and thus lower the β detection threshold. Simulations played a critical role in finalizing the detector design for the next generation ion trap.

Table 8.1. Detector size, distance, and solid angle comparisons between the previous setup and two proposed configurations. The proposed configurations are identical except one uses circular while the other uses square ΔE-E telescopes.

Detector Comparison						
Generation	MCP Area (mm^2)	MCP Distance (mm)	Total MCP Solid Angle (%)	ΔE-E Area (mm^2)	ΔE-E Distance (mm)	ΔE-E Solid Angle (%)
Previous	2116	52.5	10.2	8824	101	9.9
Proposed (Circular ΔE-E)	6800	65	17.5	9852	58	14
Proposed (Square ΔE-E)	6800	65	17.5	10000	58	14

8.4. Results

8.4. Detector Size

The first adjustment made to the detector system was increasing the MCP size and adjusting the detector locations. Both adjustments were aimed at increasing the solid angle that the detectors subtend and thus increasing the geometric efficiency of our detector system. A comparison of detector sizes and locations between the previous generation ion trap and the one being designed is shown in Table 7.1. The two proposed configurations for the next generation ion trap are identical except one uses circular while the other uses square ΔE-E telescopes. The effect this has on solid angle is negligible so the choice of circle vs. square was decided using other factors. Both of the proposed detector configurations provide approximately a factor of 2 increase in solid angle coverage over the previous trap design. This is expected to have a large effect on overall detection efficiency, however, in order to determine the exact effect both traps were simulated.

We can come up with a few metrics to assess detection efficiency of these ion trap designs. At a very basic level, we can determine the percentage of single βs and recoil ions detected out of the number of βs and recoil ions generated. The increase in efficiency of detecting

Table 8.2. A comparison of various detection efficiencies between ion trap generations. Singles are any time a particle is detected with no other consideration. β-recoil ion coincidences are events where both a β and a recoil ion are detected. NOTE: no post-processing of MCP events has occurred (i.e. their intrinsic efficiency is assumed to be 100% for the sake of comparing results of solid angle differences).

Detection Efficiency Comparison						
Generation	β Singles (Left)	β Singles (Bottom)	Recoil Singles (Right)	Recoil Singles (Top)	180° Coincidences	90° Coincidences
Previous	6.70 %	6.75 %	5.09 %	5.08 %	3.62 %	0.29 %
Proposed	11.37 %	11.32 %	10.68 %	9.79 %	9.69 %	1.00 %

single events should scale directly with the solid angle increase in the individual detectors. Additionally, β-recoil ion coincidences are of utmost importance to the experiments that will occur in the next generation ion trap. It follows then that an important measure of efficiency is the number of β-recoil-ion coincidences detected out of the total events generated. The detector's efficiency in detecting coincidence events reveals much more about the effectiveness of a detector configuration for β-delayed neutron emission experiments. For a complete picture, the single detection efficiencies are also determined but special attention should be paid to coincidence detection efficiencies. A table comparing these various efficiencies is shown in Table 7.2. Since the difference in solid angle coverage between square and circular ΔE-E telescopes is negligible, I have included only the efficiency calculations for the previous generation and the proposed design with square ΔE-E telescopes.

I simulated 1,000,000 β-decay events of ^{134}Sb with a 2^+ charge state and an $a_{b\nu}$ of 1 for both ion traps. Efficiencies are defined simply as the number of events detected as a percentage of the total number of events generated. These efficiencies will be different for different decay values and isotopes, however, they are useful as relative measures of efficiency between trap designs. Recall that the proposed designs exhibit roughly a factor of two increase in solid angle coverage for each individual detector. We observe a corresponding factor of two increase in single detection efficiency between the previous and proposed designs. Of particular importance is the detection efficiency of β-recoil ion coincidences and here we

see a significant result. The increase in detection efficiency did not scale directly with increased solid angle coverage like we expected for the single events. Rather than a factor of two increase, we actually see about a factor of three increase in the coincidence detection efficiency. This is due to a kinematic focusing effect for fast recoils and is highly encouraging for the performance of the next generation trap.

8.4. Segmentation

The next adjustment to be investigated was segmentation as a means to screen neutron detections. The purpose of the ΔE-E telescope is to detect β particles to be used as a trigger for the decay. Neutrons will occasionally deposit energy in the plastic detectors, which leaves a signature similar to β particles. This contributes to the background observed in these experiments. Segmenting the plastic ΔE detector allows us to identify most of these neutron detections in the plastic detectors.

The principle of rejecting neutron detections using segmented plastic is simple. Ions recoiling as a result of β-decay are much slower than those recoiling as a result of neutron emission. Slower ions are more heavily perturbed by the RF fields produced by the trap. Therefore, the location of ion detection on the MCP should not be correlated with the location of β detection in the plastic detector. In the case of a neutron-ion coincidence, however, the ion is only weakly perturbed by the RF fields. Since the path of the neutron and the path of the ion are back-to-back, the locations of the neutron and ion detections are highly correlated. With simulation work, we can examine the extent to which this expected behavior can be exploited in order to identify neutron-ion coincidences.

For this investigation, the ΔE detector was segmented into four even portions corresponding to the four traditional quadrants in the Cartesian coordinate system. In order to determine how strong the expected neutron-ion correlation (or conversely, how weak the β-ion correlation) is, we can examine the detection location of the ion on the MCP when a detection is made in each quadrant of the segmented ΔE. Figure 8.4 shows the ion detection locations in 4 separate charts corresponding to the four quadrants for β and neutron detec-

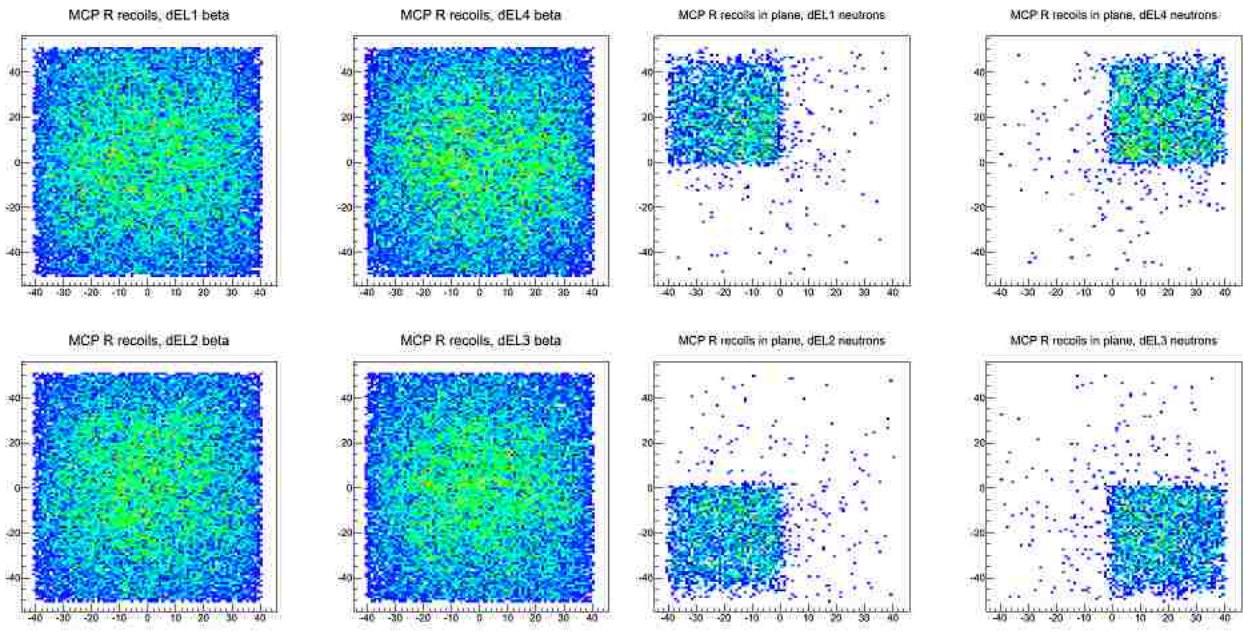

Figure 8.4. Ion detection locations for β (left) and neutron (right) detections in the 4 ΔE segments. The RF fields in the trap effectively destroy location correlation for the slowly recoiling ions associated with simple β decay whereas those associated with neutron emission have a strongly preserved path [60].

tions. What we see is a heavy correlation between neutron-ion detection locations and no correlation in the β-ion case. This is exactly what we expected and appears to be a significant phenomenon. Therefore, we can effectively exclude most erroneous neutron detection coincidences by identifying these events and analyzing them separately. The shape of these segments has light collection implications and so the shape was determined using a separate type of simulation, which I describe in the next section.

8.4. Light Collection Efficiency

A serious limitation encountered during the previous β-delayed neutron emission experiments with the BPT was an unexpectedly high β threshold in the plastic ΔE-E detectors. Any β particles that deposited less than about 70 keV of energy into the ΔE detector did not produce a signal above the electronic threshold and was not recorded. In order to probe the cause of this threshold, I performed a series of simulations on the ΔE-E plastsic telescope system. Typically our simulations ignore complicating factors like light collection and

instead record only the total amount of energy deposited into detector volumes. Post processing applies efficiency cuts to model thresholds and detector efficiencies. Since we wished to examine the source of the β threshold, I altered the simulations to model the finer details of a β detection in the plastic detector. Rather than simply record the energy deposited in the plastic, I had the plastic simulate the optical photons produced during a scintillation event. By including the light guides we can model the actual transportation of these optical photons from the detector to the photomultiplier tube (PMT).

The first question these simulations can help answer is the shape of the ΔE-E segments. The two proposed designs we investigated are shown in Figure 8.5. The first is a simple lateral and vertical bisection creating four equally sized squares. The second design is four equally sized triangles created using diagonal bisections. The main concern which dictates the choice of segment design is light collection. Therefore, the simulations to decide the segmentation scheme focused on scintillation photons that escape the edge(s) on which the light guides will be attached. In order to probe this property of the differently shaped segments, individual segments were simulated using Geant4. These segments were attached to a mock light guide and the number of photons that escape the end of the light guide was counted. The triangular segment allowed approximately 20% more light to escape the detector. This difference is likely the result of a more simple and straight-forward light guide geometry for the triangular segment. The long side with no corners allows more light to traverse the light guide directly.

With optical photon simulation it became clear that the design of the light guides themselves contribute to a great deal of loss of light between the scintillator detector and the PMT. Every time a photon comes into contact with the mylar foil that encases the light guide and detector, it has a chance to be absorbed rather than reflected. Since this effect dominates our loss of light, we can increase light transportation efficiency by reducing the number of reflections encountered between detector and PMT. A few ways to accomplish this task were investigated and will be implemented in the design for the new detector system.

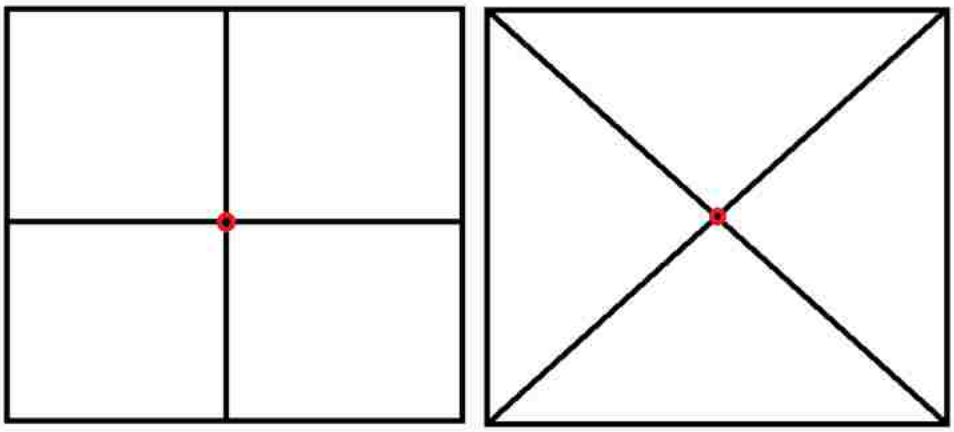

Figure 8.5. The two proposed segmentation schemes, square vs triangle.

A schematic for the modules used in the BPT is shown in Figure 8.6. The light guide attaches to the ΔE detector, curves 90°, traverses the long edge of the E detector, and crooks twice before making contact with the PMT. This is an inherently unfavorable design for light collection efficiency but is unfortunately necessary due to physical constraints on the detector module size. Although major changes to the light guide shape (such as removing all bends) cannot be accomplished, some minor changes can be made to decrease the number of reflections before entering the PMT.

The first change that can be made involves the length of the light guides. This length is dictated by the depth of the E detector since the PMT must slide in behind the E detector. The purpose of the E detector in any ΔE-E telescope is to have an infinite effective thickness to the particles it is intended to detect. The idea is that all particles are completely stopped and thus deposit all of their energy into the E detector. For the BPT, this detector was made to be 4 inches thick. This thickness is sufficient to stop β particles with energies of approximately 30 MeV. We expect a maximum β energy of approximately 15 MeV so we can actually shorten our E detector by 2 inches without a loss of efficiency. This translates to a reduction in light guide length from 18 cm to 9 cm. With a shorter path to travel there is a lower average number of reflections needed to make it from the detector to the PMT. Since each interaction with the boundary of the light guide presents a chance for the photons to

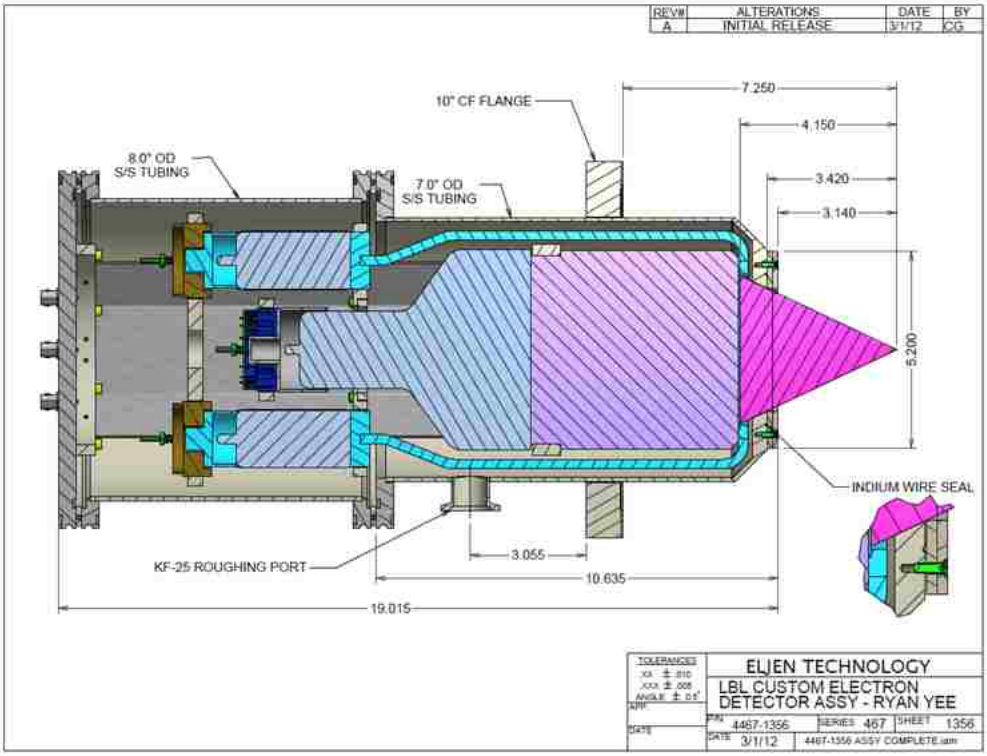

Figure 8.6. This is a cross-sectional drawing of the ΔE-E telescope module used in the 2013 campaign of BPT experiments at CARIBU.

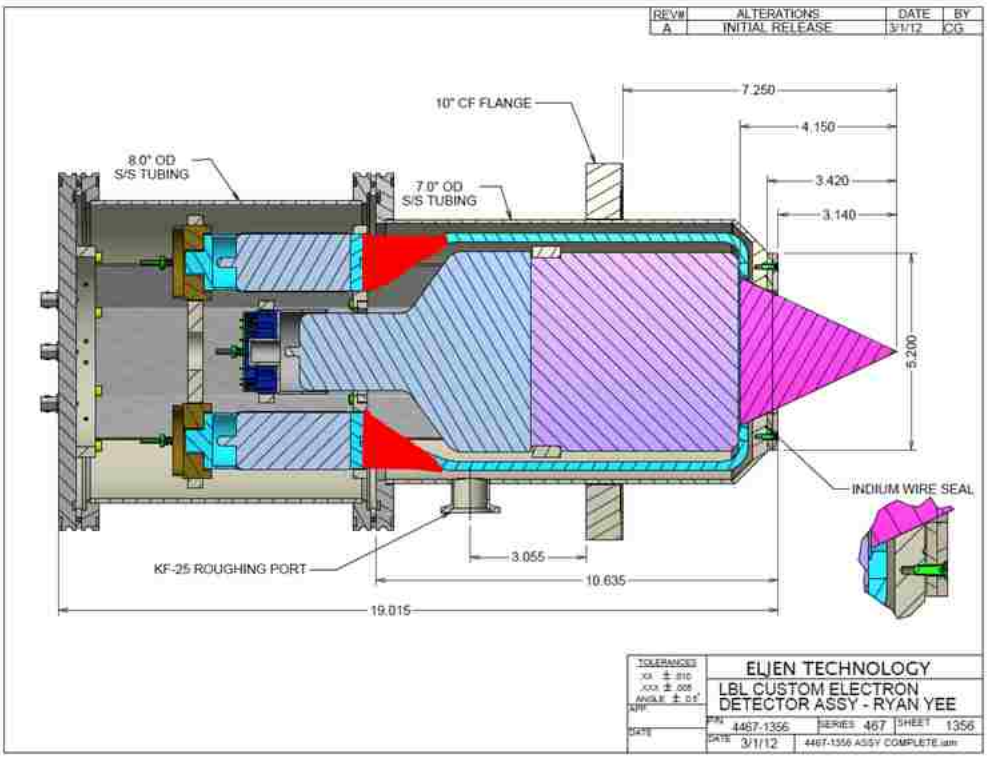

Figure 8.7. A schematic view of the ΔE-E telescope module edited to show flared light guide design.

be absorbed rather than reflected, this is the primary source of light loss in our system. In addition to shortening them, we can remove a few of the crooks in the light guides, which introduce an unnecessary number of reflections between emission in the detector and the PMT. The original design for the ΔE-E telescope exhibits two 30° crooks so that the PMT can fit behind the telescope. By removing these crooks and replacing them with a flared design (shown in Figure 8.7) we can again reduce the number of reflections photons encounter between detector and PMT.

In order to investigate the effect these changes have on light transport, simulations were performed using groups of 350 keV electrons that bombard the detector face in evenly spaced locations. The output of these simulations were the optical scintillation photons exiting the light guide. Ultimately it is more useful to compare the percentage of photons that reach the PMT as a percentage of the total photons that are created as a product of scintillation. Table 7.3 shows the results of these simulations. What we find is that approximately 2.5

Table 8.3. The results of the two light guide adjustments. Results are reported as an average percentage of photons produced by scintillation that escape the light guide and make contact with the PMT.

Light Guide Adjustment Comparison		
	18-cm Light Guide	9-cm Light Guide
Crooked Light Guide	0.67 %	0.77 %
Flared Light Guide	1.4 %	1.73 %

times as much light escapes the short, flared light guides as the long, crooked design used in the BPT. We expect this to lower the β energy detection threshold from 70 keV to about 30 keV.

8.5. Conclusions and Commissioning

β-delayed neutron emission as a phenomenon has applications in fields ranging from nuclear structure to nuclear reactor operation and the non-proliferation of nuclear weapons. Additionally, β-delayed neutron emission plays a key role in r-process nucleosynthesis. Determining branching ratios of isotopes that undergo β-delayed neutron emission will improve nuclear structure models and allow for a more accurate prediction of the abundance of r-process elements. In order to determine β-delayed neutron emission branching ratios, a time of flight method will be employed using a dedicated ion trap that has finished the design phase.

The next generation ion trap will be known as the BEtA-Recoil Trap (BEARtrap). Through the use of extensive simulations, BEARtrap was designed using the BPT currently installed at Argonne National Laboratory as a jumping off point. Several upgrades and improvements were made for the next generation trap. BEARtrap features rod electrodes in place of the BPT's plates in order to minimize backgrounds from ions outside the ion cloud. Additionally, the size and location of the MCPs and ΔE-E telescopes were altered to increase the geometric efficiency seen in the BPT by a factor of 3. Segmentation was also added to the ΔE detector as a means of rejecting neutron detection in the telescope. This eliminates a significant background present in previous experiments using the BPT. Finally

adjustments to the light guides were made to increase the light collection efficiency of the ΔE detector. We expect the adjustments to lower the β threshold by as much as 50%. This is significant as the β threshold lowered the overall efficiency of the BPT to detect β-recoil coincidences.

Now that the design for BEARtrap has been finalized, construction and commissioning are the final requirements before original research can be performed using BEARtrap. At the time of this dissertation, components for BEARtrap are being assembled. The commissioning process will include examination of the decay of two unstable isotopes: ^{92}Rb and ^{137}I. These isotopes have well studied decay schemes. ^{92}Rb decays via simple β-decay to the ground state of ^{92}Sr 95.2(7)% of the time [61]. This makes it an ideal candidate to characterize the response of the β detectors. ^{137}I, on the other hand, is a well-studied β-delayed neutron emitter. With a branching ratio of $P_n = 7.14(23)\%$ [58] and well-known neutron energy spectrum, ^{137}I is an ideal candidate to characterize BEARtrap's β-delayed neutron emission response. In addition to the commissioning run, beam time has already been secured for a pair of original scientific experiments. These will follow the successful commissioning of BEARtrap and will take place at Argonne National Laboratory.

Chapter 9. β-Delayed Neutron Studies and BEARtrap Conclusions

The neutron capture process responsible for the production of the other half of elements heavier than iron is the r-process. The rapid capture of neutrons produces highly unstable, neutron-rich nuclei that decay back to stability after the the neutrons are all consumed. β-decay is the most common mode of decay for these r-process isotopes, however, β-delayed neutron emission is energetically allowed for these neutron-rich isotopes. β-delayed neutron emission has the effect of broadening the r-process peaks created by waiting points at closed neutron shells and evening out the jagged features caused by pairing effects. In order to predict the influence β-delayed neutron emission has on r-process abundances, the branching ratios must be measured. Additionally, the emitted neutron energy spectrum is of interest to r-process calculations as well as simulations of the neutron flux in nuclear reactors. The second part of this thesis explains the design and future construction of a next generation ion trap called BEARtrap dedicated to performing β-delayed neutron studies.

The unstable isotopes synthesized by the r-process decay back to stability after the neutron freeze out phase. For neutron-rich isotopes, there are two decay modes that can be taken back to stability: β-decay and β-delayed neutron emission. When nuclei β-decay, the nucleon number is preserved but β-delayed neutron emission leads to a loss of nucleons. This has the effect of spreading the peaks in the r-process abundance curve created by closed shells and evening out the jagged curve caused by pairing effects. Knowing the β-delayed neutron emission branching ratios is crucial to constructing theoretical models for higher neutron emission multiplicities that are used to predict the final r-process abundances.

9.1. Results of Previous Work

The recoil-ion time-of-flight technique described in this thesis allows for measuring the branching ratio and neutron energy spectrum simultaneously. This is accomplished through trapping radioactive ions and detecting not the neutrons but the βs and recoiling ions.

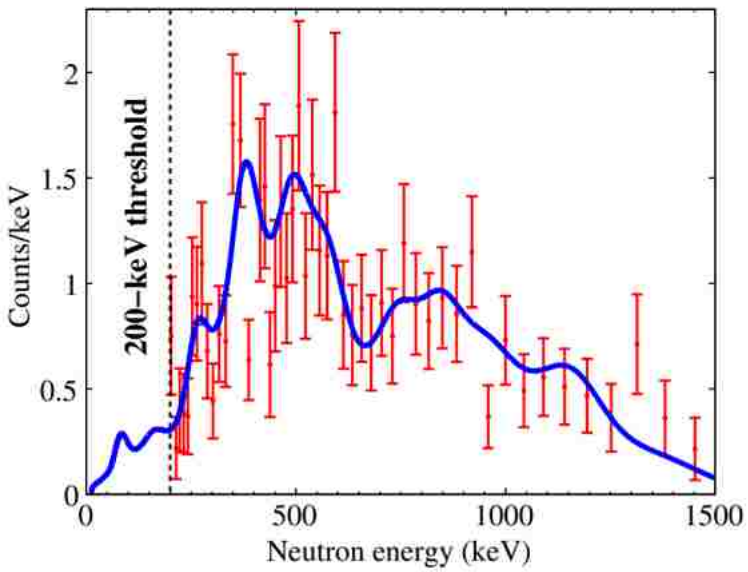

Figure 9.1. A comparison of the known neutron energy spectrum of ^{137}I (blue) to that measured during the proof of principle experiment (red) [50].

A proof-of-principle experiment was carried out successfully using the BPT at Argonne National Laboratory. ^{137}I was chosen to explore the efficacy of the time-of-flight technique because it has both a well measured neutron energy spectrum and a well known branching ratio. The accepted value for the β-delayed neutron emission branching ratio of ^{137}I is $P_n = 7.33 \pm 0.38\%$ while the value found using the time-of-flight technique in the proof-of-principle experiment was $P_n = 6.95 \pm 0.76\%$ [50]. Figure 9.1 shows the neutron energy spectrum measured during the same experiment. Recall that the strength of this technique lies in its ability to measure the branching ratio and the neutron energy spectrum simultaneously without detection of the neutron. This makes the time-of-flight technique particularly useful going forward when isotopes for which no information is known will be studied.

Follow up experiments using the BPT with more detectors showed improved results for both the neutron energy spectrum as well as the branching ratio. Figure 9.2 shows the neutron energy spectrum measured by Czeszumska *et al* [52]. Both the precision and the neutron energy resolution have been improved between this measurement and the proof-of-principle experiment. The work of this thesis shows that we expect even greater improvements in such

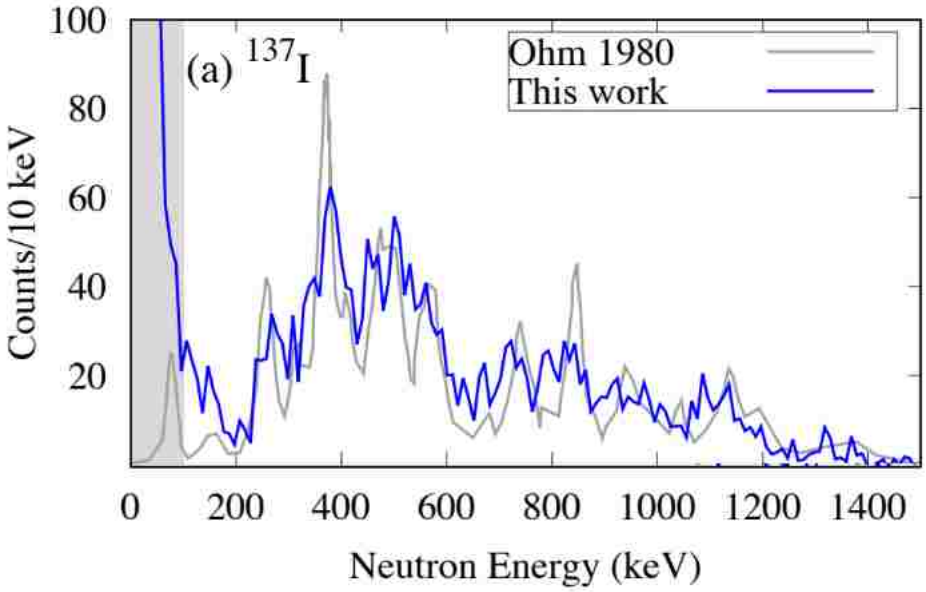

Figure 9.2. A comparison of the previously measured neutron energy spectrum of ^{137}I (gray) to that measured during the BPT experiment (blue) [52].

measurements using the next-generation ion trap for β-delayed neutron emission studies. In addition to the improved measurement of the neutron energy spectrum, the branching ratio was measured with a higher precision. Recall that the proof-of-principle experiment concluded that the branching ratio of ^{137}I was $P_n = 6.95 \pm 0.76\%$. The result of the follow-up experiment is that the branching ratio is $P_n = 7.18 \pm 0.50\%$. When comparing these results to the accepted IAEA value of $P_n = 7.33 \pm 0.38\%$ we find agreement with both results but a greater precision with the follow-up result. This precision will be further improved with BEARtrap.

9.2. BEARtrap

Once the principle of the time-of-flight technique had been proven and follow-up experiments had been performed, design efforts began to create a dedicated ion trap to perform these studies. This new trap will be called the BEtA-Recoil trap (BEARtrap). BEARtrap is based off of the Beta Paul Trap (BPT) used in the previous experiments and explored design improvements using a combination of SIMION and Geant4 simulations. The BPT's plate electrodes will be replaced with rod electrodes to reduce background from β scattering off the

electrodes, the size and distance of the detectors will be changed to increase geometric efficiency, the plastic detectors will be segmented to allow for identification of neutron-recoil ion coincidences, and the light guide design will be adjusted to increase light collection efficiency thus lowering the β detection threshold. All of these changes to the design of the BPT will allow BEARtrap to perform β-delayed neutron emission studies with greater precision. The design for BEARtrap is finalized and the components are currently being assembled. Commissioning beam time has already been awarded at Argonne National Laboratory (ANL) for ^{92}Rb (a simple β emitter) and ^{137}I (β-delayed neutron emission precursor isotope). These isotopes were chosen because they have well studied decays and can be made with high beam intensities at CARIBU at ANL. Once BEARtrap has been properly commissioned, its scientific campaign will likely begin with $^{134-136}$Sn for r-process nucleosynthesis and $^{98m,99-103}$Y for nuclear energy considerations.

Bibliography

[1] F. Hoyle. The synthesis of the elements from hydrogen. *Monthly Notices of the Royal Astronomical Society*, 106:343, 1946.

[2] Lepine-Szily , A Lpine-Szily, Alinka Descouvemont, Pierre Descouvemont, and Pierre . Nuclear astrophysics: Nucleosynthesis in the universe. *International Journal of Astrobiology*, 11:243–250, 10 2012.

[3] E. Margaret Burbidge, G. R. Burbidge, William A. Fowler, and F. Hoyle. Synthesis of the elements in stars. *Rev. Mod. Phys.*, 29:547–650, Oct 1957.

[4] Christopher Sneden, John J. Cowan, and Roberto Gallino. Neutron-capture elements in the early galaxy. *Annual Review of Astronomy and Astrophysics*, 46(1):241–288, 2008.

[5] D.D Clayton, W.A Fowler, T.E Hull, and B.A Zimmerman. Neutron capture chains in heavy element synthesis. *Annals of Physics*, 12(3):331 – 408, 1961.

[6] P. A. Seeger, W. A. Fowler, and D. D. Clayton. Nucleosynthesis of heavy elements by neutron capture. *Ap. J Suppl*, 97, 1965.

[7] F. Käppeler, R. Gallino, S. Bisterzo, and Wako Aoki. The *s* process: Nuclear physics, stellar models, and observations. *Rev. Mod. Phys.*, 83:157–193, Apr 2011.

[8] F Kappeler, H Beer, and K Wisshak. s-process nucleosynthesis-nuclear physics and the classical model. *Reports on Progress in Physics*, 52(8):945–1013, aug 1989.

[9] Z.Y. Bao, H. Beer, F. Kappeler, F. Voss, K. Wisshak, and T. Rauscher. Neutron cross sections for nucleosynthesis studies. *Atomic Data and Nuclear Data Tables*, 76(1):70 – 154, 2000.

[10] Sachiko Amari. Recent progress in presolar grain studies. *Mass Spectrometry*, 3:S0042–S0042, 01 2014.

[11] J.G. Peters. Nucleosynthesis by the s-process in stars of 9 and 15 solar masses. *Astrophysical Journal*, 154:225, 1968.

[12] M. Pignatari, R. Gallino, M. Heil, M. Wiescher, F. Kppeler, F. Herwig, and S. Bisterzo. The weak s-process in massive stars and its dependence on the neutron capture cross sections. *The Astrophysical Journal*, 710(2):1557, 2010.

[13] N. Prantzos, M. Hashimoto, and K Nomoto. The s-process in massive stars - yields as a function of stellar mass and metallicity. *Astronomy and Astrophysics*, 234:211–229, Aug 1990.

[14] R Reifarth, C Lederer, and F Kppeler. Neutron reactions in astrophysics. *Journal of Physics G: Nuclear and Particle Physics*, 41(5):053101, mar 2014.

[15] S R Elliott et al. The majorana project. *Journal of Physics: Conference Series*, 173(1):012007, 2009.

[16] D.-M. Mei and A. Hime. Muon-induced background study for underground laboratories. *Phys. Rev. D*, 73:053004, Mar 2006.

[17] Kurt Schoenberg and Paul Lisowski. Lansce a key facility for national science and defense. *Los Alamos Science*, 30, November 2006.

[18] John Ullmann. An overview of dance; a 4pi baf_2 detector for neutron capture measurements at lansce. *Progress of theoretical physics*, 92:275–306, 1996.

[19] M. Weigand, T. Bredeweg, A. Couture, K. Gbel, Tanja Heftrich, M. Jandel, Franz Kaeppeler, C. Lederer, Niko Kivel, Gunther Korschinek, M. Krtika, J. O'Donnell, J. Ostermller, R. Plag, R. Reifarth, D. Schumann, J. Ullmann, and Anton Wallner. Ni 63 (n ,) cross sections measured with dance. *Physical Review C*, 92, 10 2015.

[20] J. M. Wouters, A. A. Vicente, T. A. Bredeweg, E. Esch, R. C. Haight, R. Hatarik, J. M. O'Donnell, R. Reifarth, R. S. Rundberg, J. M. Schwantes, S. A. Sheets, J. L. Ullmann,

D. J. Vieira, and J. B. Wilhelmy. Acquisition-analysis system for the dance (detector for advanced neutron capture experiments) baf/sub 2/ gamma-ray calorimeter. *IEEE Transactions on Nuclear Science*, 53(3):880–885, June 2006.

[21] D. A. Brown and et al. Endf/b-viii.0: The 8th major release of the nuclear reaction data library with cielo-project cross sections, new standards and thermal scattering data. *Nucl. Data Sheets*, 1:148, 2018.

[22] M. Jandel, T. A. Bredeweg, E. M. Bond, M. B. Chadwick, R. R. Clement, A. Couture, J. M. O'Donnell, R. C. Haight, T. Kawano, R. Reifarth, R. S. Rundberg, J. L. Ullmann, D. J. Vieira, J. B. Wilhelmy, J. M. Wouters, U. Agvaanluvsan, W. E. Parker, C. Y. Wu, and J. A. Becker. Neutron capture cross section of ^{241}Am. *Phys. Rev. C*, 78:034609, Sep 2008.

[23] F Becvar, M Krticka, and M Jentschel. Simulations of gamma cascades and modelling atomic collision chains. *Journal of Research of the National Institute of Standards and Technology*, 105:113–123, Feb 2000.

[24] S Valenta. private communication. October 2019.

[25] K. Macon. Direct measurements of nuclear reactions in hot stellar environments. 2016.

[26] Endf/b-viii.0: The 8th major release of the nuclear reaction data library with cielo-project cross sections, new standards and thermal scattering data. *Nucl. Data Sheets*, 1, 2018.

[27] Sammy, multilevel r-matrix fits to neutron and charged-particle cross-section data using bayes' equations.

[28] A Couture. private communication. October 2019.

[29] I. Dillamnn, R. Plag, F. Käppeler, and T. Rauscher. The thid update of the "karlsruhe astrophysical database of nucleosynthesis in stars". *EFNUDAT Fast Neutrons, Proceedings of the Scientific Workshop on Neutron Measurements*, 2009.

[30] J. Marganiec, I. Dillmann, C. Domingo Pardo, F. Käppeler, R. Reifarth, R. Gallino, M. Pignatari, and P. Grabmayr. Neutron capture cross sections of ^{74}Ge, ^{76}Ge, and ^{75}As at 25 kev. *Phys. Rev. C*, 79:065802, Jun 2009.

[31] G Walter and H Beer. Measurement of neutron capture cross sections of s-only isotopes - ge-70, sr-86, and sr-87. *Astronomy and Astrophysics*, 142:268–272, Jan. 1985.

[32] V.M. Piksaikin, A.S. Egorov, A.A. Goverdovski, D.E. Gremyachkin, and K.V. Mitrofanov. High resolution measurements of time-dependent integral delayed neutron spectra from thermal neutron induced fission of 235u. *Annals of Nuclear Energy*, 102:408 – 421, 2017.

[33] G. I. Bell and S. Glasstone. *Nuclear Reactor Theory*. Van Nostrand Reinhold Company, 1970. osti: 4074688.

[34] D.R. Slaughter et al. The nuclear car wash: A system to detect nuclear weapons in commercial cargo shipments. *Nuclear Instruments and Methods in Physics Research Section A: Accelerators, Spectrometers, Detectors and Associated Equipment*, 579(1):349 – 352, 2007.

[35] N. Nishimura, H. Sawai, T. Takawaki, S. Yamada, and F. K. Thielemann. The intermediate r-process in core-collapse supernovae driven by the magneto-rotational instability. *The Astrophysical Journal Letters*, 836(2):L21, 2017.

[36] C. Freiburghaus, S. Rosswog, and F.-K. Thielemann. r-process in neutron star mergers. *The Astrophysical Journal Letters*, 525(2):L121, 1999.

[37] Alexey Evdokimov, Iris Dillmann, M. Marta, F. Bosch, A. Dolinskii, Christophor Kozhuharov, Yu Litvinov, F. Nolden, M. Steck, H. Weick, Thomas Faestermann, Roman Gernhuser, and Ludwig Maier. An alternative approach to measure -delayed neutron emission. *Proceedings of Science*, pages 115–, 01 2012.

[38] J. Engel and M. Bender. Beta-decay from r-process waiting-point nuclei. *AIP Conference Proceedings*, 481(1):554–560, 1999.

[39] F. K. Thielemann, J. Metzinger, and H. V. Klapdor. Beta-delayed fission and neutron emission: Consequences for the astrophysicalr-process and the age of the galaxy. *Zeitschrift für Physik A Atoms and Nuclei*, 309(4):301–317, Dec 1983.

[40] T. Kodama and K. Takahashi. R-process nucleosynthesis and nuclei far from the region of β-stability. *Nuclear Physics A*, 239:489–510, March 1975.

[41] John Cowan and Friedrich Thielemann. R-process nucleosynthesis in supernovae. *Physics Today - PHYS TODAY*, 57:47–53, 10 2004.

[42] Rebecca Surman, Matthew Mumpower, and Ani Aprahamian. The sensitivity of -process nucleosynthesis to individual -delayed neutron emission probabilities. 2015.

[43] A. Tolosa-Delgado, J. Agramunt, J.L. Tain, A. Algora, C. Domingo-Pardo, A.I. Morales, B. Rubio, A. Tarifeo-Saldivia, F. Calvio, G. Cortes, N.T. Brewer, B.C. Rasco, K.P. Rykaczewski, D.W. Stracener, J.M. Allmond, R. Grzywacz, R. Yokoyama, M. Singh, T. King, M. Madurga, S. Nishimura, V.H. Phong, S. Go, J. Liu, K. Matsui, H. Sakurai, G.G. Kiss, T. Isobe, H. Baba, S. Kubono, N. Fukuda, D.S. Ahn, Y. Shimizu, T. Sumikama, H. Suzuki, H. Takeda, P.A. Sderstrm, M. Takechi, C.G. Bruno, T. Davinson, C.J. Griffin, O. Hall, D. Kahl, P.J. Woods, P.J. Coleman-Smith, M. Labiche, I. Lazarus, P. Morrall, V.F. E. Pucknell, J. Simpson, S.L. Thomas, M. Prydderch, L.J. Harkness-Brennan, R.D. Page, I. Dillmann, R. Caballero-Folch, Y. Saito, A. Estrade, N. Nepal, F. Montes, G. Lorusso, J. Liang, S. Bae, J. Ha, and B. Moon. Commissioning

of the briken detector for the measurement of very exotic -delayed neutron emitters. *Nuclear Instruments and Methods in Physics Research Section A: Accelerators, Spectrometers, Detectors and Associated Equipment*, 925:133 – 147, 2019.

[44] W.A. Peters, S. Ilyushkin, M. Madurga, C. Matei, S.V. Paulauskas, R.K. Grzywacz, D.W. Bardayan, C.R. Brune, J. Allen, J.M. Allen, Z. Bergstrom, J. Blackmon, N.T. Brewer, J.A. Cizewski, P. Copp, M.E. Howard, R. Ikeyama, R.L. Kozub, B. Manning, T.N. Massey, M. Matos, E. Merino, P.D. O'Malley, F. Raiola, C.S. Reingold, F. Sarazin, I. Spassova, S. Taylor, and D. Walter. Performance of the versatile array of neutron detectors at low energy (vandle). *Nuclear Instruments and Methods in Physics Research Section A: Accelerators, Spectrometers, Detectors and Associated Equipment*, 836:122 – 133, 2016.

[45] Wolfgang Paul. Electromagnetic traps for charged and neutral particles. *Rev. Mod. Phys.*, 62:531–540, Jul 1990.

[46] Raymond E. March. Quadrupole ion traps. *Mass Spectrometry Reviews*, 28(6):961–989, 2009.

[47] Donald J. Douglas, Aaron J. Frank, and Dunmin Mao. Linear ion traps in mass spectrometry. *Mass Spectrometry Reviews*, 24(1):1–29, 2005.

[48] N.D. Scielzo et al. The β-decay paul trap: A radiofrequency-quadrupole ion trap for precision β-decay studies. *Nuclear Instruments and Methods in Physics Research Section A: Accelerators, Spectrometers, Detectors and Associated Equipment*, 681:94 – 100, 2012.

[49] B. S. Alan, N.D. Scielzo, K. Siegl, A. Czeszumska, G. Savard, A. Aprahamian, S.A. Caldwell, C.J. Chiara, J.A. Clark, J.P. Greene, J. Harker, S.T. Marley, G.E. Morgan, E.B. Norman, R. Orford, S.W. Padgett, A. Perez Galvan, K.S. Sharma, and S.Y. Strauss. Beta-delayed-neutron studies of ^{135,136}sb and ^{140}i performed with trapped ions. *submitted to Physical Review C*.

[50] R. M. Yee et al. β-delayed neutron spectroscopy using trapped radioactive ions. *Phys. Rev. Lett.*, 110:092501, Feb 2013.

[51] K. Siegl, N. D. Scielzo, A. Czeszumska, J. A. Clark, G. Savard, A. Aprahamian, S. A. Caldwell, B. S. Alan, M. T. Burkey, C. J. Chiara, J. P. Greene, J. Harker, S. T. Marley, G. E. Morgan, J. M. Munson, E. B. Norman, R. Orford, S. Padgett, A. Perez Galván, K. S. Sharma, and S. Y. Strauss. Recoil ions from the β decay of ^{134}Sb confined in a paul trap. *Phys. Rev. C*, 97:035504, Mar 2018.

[52] A. Czeszumska, N.D. Scielzo, S.A. Caldwell, K. Siegl, B. S. Alan, G. Savard, A. Aprahamian, C.J. Chiara, J.A. Clark, J.P. Greene, J. Harker, S.T. Marley, G.E. Morgan, E.B. Norman, R. Orford, S.W. Padgett, A. Perez Galvan, K.S. Sharma, and S.Y. Strauss. Beta-delayed neutron studies of $^{137-138}$i and $^{144-145}$cs performed with trapped ions. *Submitted to Physical Review C.*

[53] N. D. Scielzo, S. J. Freedman, B. K. Fujikawa, and P. A. Vetter. Measurement of the $\beta - \nu$ correlation using magneto-optically trapped ^{21}Na. *Phys. Rev. Lett.*, 93:102501, Aug 2004.

[54] D. Manura and D. Dahl. *SIMION (R) 8.0 User Manual.* Ringoes, NJ 08551, Jan 2008.

[55] S. Agostinelli et al. Geant4a simulation toolkit. *Nuclear Instruments and Methods in Physics Research Section A: Accelerators, Spectrometers, Detectors and Associated Equipment*, 506(3):250 – 303, 2003.

[56] Root - an object oriented data analysis framework. *Nucl. Inst. & Meth. in Phys. Res. A*, pages 81–86, 1997.

[57] R. Capote et al. Reference input parameter library (ripl-3). *Nuclear Data Sheets*, 110:3107–3214, Dec 2009.

[58] E Browne and JK Tuli. Nuclear data sheets for a= 137. *Nuclear Data Sheets*, 108(10):2173–2318, 2007.

[59] K. Siegl et al. Study of recoil ions from the β-decay of ^{134}sb using the beta-decay paul trap. *Submitted to Phys. Rev. C*, 2018.

[60] G. E. Wilson. Private communication.

[61] Coral M Baglin. Nuclear data sheets for a= 92. *Nuclear Data Sheets*, 113(10):2187–2389, 2012.

Vita

Alexander Melvin Laminack was born in Atlanta, Georgia. After moving to Mississippi and graduating high school there, he attended The University of Alabama where he received a Bachelor of Science degree in physics and mathematics in May 2015. Immediately following college, he began his graduate studies at Louisiana State University in nuclear astrophysics. He will continue his work in nuclear physics as a postdoctoral researcher at Oak Ridge National Laboratory in Oak Ridge, Tennessee.